

Spring 2015

Electrochemical fatigue crack treatment

Konstantin Dolgan
Louisiana Tech University

Follow this and additional works at: <https://digitalcommons.latech.edu/dissertations>



Part of the [Mechanical Engineering Commons](#)

Recommended Citation

Dolgan, Konstantin, "" (2015). *Dissertation*. 225.
<https://digitalcommons.latech.edu/dissertations/225>

This Dissertation is brought to you for free and open access by the Graduate School at Louisiana Tech Digital Commons. It has been accepted for inclusion in Doctoral Dissertations by an authorized administrator of Louisiana Tech Digital Commons. For more information, please contact digitalcommons@latech.edu.

ELECTROCHEMICAL FATIGUE CRACK TREATMENT

by

Konstantin Dolgan, B.S., M.S.

A Dissertation Presented in Partial Fulfillment
of the Requirements for the Degree
Doctor of Philosophy

COLLEGE OF ENGINEERING AND SCIENCE
LOUISIANA TECH UNIVERSITY

May 2015

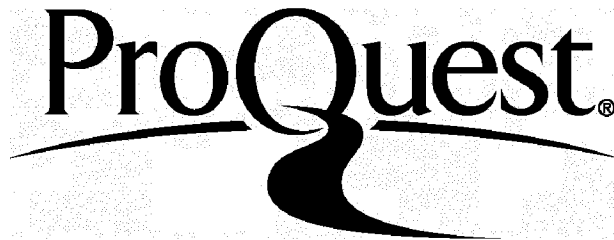
ProQuest Number: 3664373

All rights reserved

INFORMATION TO ALL USERS

The quality of this reproduction is dependent upon the quality of the copy submitted.

In the unlikely event that the author did not send a complete manuscript and there are missing pages, these will be noted. Also, if material had to be removed, a note will indicate the deletion.



ProQuest 3664373

Published by ProQuest LLC(2015). Copyright of the Dissertation is held by the Author.

All rights reserved.

This work is protected against unauthorized copying under Title 17, United States Code.
Microform Edition © ProQuest LLC.

ProQuest LLC
789 East Eisenhower Parkway
P.O. Box 1346
Ann Arbor, MI 48106-1346

LOUISIANA TECH UNIVERSITY

THE GRADUATE SCHOOL

23 January 2015

Date

We hereby recommend that the thesis prepared under our supervision

by Konstantin Dolgan

entitled Electrochemical Fatigue Crack Treatment

be accepted in partial fulfillment of the requirements for the Degree of

Ph.D. Materials and Infrastructure Systems

[Signature]
Supervisor of Thesis Research

[Signature]
Head of Department

Department

Recommendation concurred in:

[Signature]
[Signature]

Advisory Committee

[Signature]
[Signature]

Approved:

[Signature]
Director of Graduate Studies

Approved:

[Signature]
Director of the Graduate

School

[Signature]
Dean of the College

ABSTRACT

Fatigue is responsible for at least 50% of all mechanical and 90% of all metallic failures. Fatigue cracks often start at stress concentrations, and without timely and appropriate remediation, tend to exhibit relatively fast propagation that leads to property damage and sometimes serious accidents.

The objective of this research was to develop a new method of fatigue crack treatment in steel structures and estimate its efficiency and limitations. The method was based on placing fatigue cracks under compression by depositing nickel onto the surfaces of the cracks. The proposed method was applied to ASTM E399 compact-tension specimens machined from ASTM A36 steel. This study found that the method was able to arrest fatigue crack propagation. Fatigue crack arrest period varied from 2,000 to 30,000 cycles. The fatigue life of the specimens was extended for up to 55,000 cycles. In many cases the re-initiation life of fatigue cracks after treatment was similar to the crack initiation life obtained from the V-shaped starter notches. A power law relationship was developed that successfully correlates the fatigue crack arrest life and the stress intensity factor range applied for post-treatment load cycling. Fatigue crack packing with nickel resulted in significant reduction of stress concentration factors of the cracks.

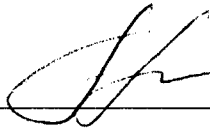
Spectroscopic analysis confirmed the presence of nickel in electrochemically treated fatigue cracks. The amount of nickel deposited was found to be non-uniform along the length of the cracks. This study found that an elastic finite element analysis (FEA) supported the notion of compressive stresses being developed at the crack tip and of a significant reduction in the stress concentration factor of the fatigue crack due to application of this treatment method. FEA has also supported the expectation that increasing the dosage of crack packing material would tend to result in a longer crack re-initiation period. The proposed method of electrochemical fatigue crack treatment was found to be beneficial in terms of improved corrosion resistance of treated specimens as long as the treatment was uniform and continuous. The average general corrosion rate of nickel-plated ASTM A36 steel specimens that were uncracked was 80% lower than that of the non-plated cases. The discontinuous deposition observed within cracks was expected to promote localized corrosion of the A36 base metal. Future work will examine the use of deposition candidates with less of a tendency toward dissimilar metal corrosion.

APPROVAL FOR SCHOLARLY DISSEMINATION

The author grants to the Prescott Memorial Library of Louisiana Tech University the right to reproduce, by appropriate methods, upon request, any or all portions of this Thesis. It is understood that "proper request" consists of the agreement, on the part of the requesting party, that said reproduction is for his personal use and that subsequent reproduction will not occur without written approval of the author of this Thesis. Further, any portions of the Thesis used in books, papers, and other works must be appropriately referenced to this Thesis.

Finally, the author of this Thesis reserves the right to publish freely, in the literature, at any time, any or all portions of this Thesis.

Author



Date

15 - Feb - 2015

DEDICATION

I dedicate this dissertation to my parents and my lovely wife. This achievement wouldn't be possible without their continuous support.

TABLE OF CONTENTS

ABSTRACT.....	iii
DEDICATION.....	v
LIST OF TABLES.....	viii
LIST OF FIGURES.....	ix
CHAPTER 1 INTRODUCTION.....	1
CHAPTER 2 BACKGROUND.....	2
2.1 Metal Fatigue.....	2
2.1.1 Motivation to Study Metal Fatigue.....	2
2.1.2 Crack Initiation.....	5
2.1.3 Linear Elastic Fracture Mechanics Concepts.....	8
2.1.4 Crack Tip Plasticity.....	17
2.1.5 Fracture Toughness.....	18
2.1.6 Fatigue Crack Growth.....	20
2.1.7 Crack Growth Life Integration.....	28
2.1.8 Mean Stress Effect.....	30
2.1.9 Cyclic Plastic Zone.....	33
2.1.10 Crack Closure.....	36
2.1.11 Corrosion Fatigue.....	41
2.1.12 Fatigue Crack Repair Techniques.....	43
2.2 Electrochemistry.....	46
2.2.1 Definition and Fundamentals of Electrochemistry.....	46
2.2.2 Electrochemical Cells.....	47
2.2.3 Electrodeposition of Metals, Electroplating.....	49
2.2.4 Corrosion of Metals.....	52
CHAPTER 3 METHODOLOGY AND PROCEDURES.....	62

3.1 Fatigue Crack Initiation and Growth	62
3.2 Electrochemical Fatigue Crack Treatment.....	72
3.3 Treated Crack Growth.....	75
3.4 Scanning Electron Microscopy	75
3.5 Optical Microscopy.....	79
3.6 Energy-dispersive X-ray Spectroscopy.....	80
3.7 Corrosion Susceptibility Determination	80
3.8 Finite Element Modeling and Simulation	86
CHAPTER 4 RESULTS AND DISCUSSION.....	91
4.1 Fatigue Crack Initiation and Growth	91
4.2 Re-initiation of Treated Fatigue Cracks.....	103
4.3 Microscopic Analysis.....	114
4.4 Spectroscopic Analysis	125
4.5 Finite Element Analysis.....	129
4.6 Corrosion Susceptibility Analysis.....	150
CHAPTER 5 CONCLUSIONS	158
APPENDIX.....	165
REFERENCES	173

LIST OF TABLES

Table 1. Major pipeline accidents in the USA caused by fatigue cracks	4
Table 2. The fatigue properties of ASTM A36 steel	12
Table 3. Paris' Law modifications and variations.....	27
Table 4. Composition, operating conditions and mechanical properties of Watts nickel plating bath	58
Table 5. The values of standard electrode potentials of some metals.	58
Table 6. Mechanical properties and chemistry of ASTM A36 Mild (low-carbon) steel.....	64
Table 7. Material properties of the nickel deposit for the finite element modeling and analysis	87
Table 8. Elemental content (weight %) of electrochemically treated specimen.....	126
Table 9. FEA model results for the maximum and minimum normal stresses.....	126
Table 10. Results of the treated fatigue crack re-initiation analysis based on the crack-length-adjusted stress intensity factor range, ΔK_{tr}	126
Table A1. Fatigue crack propagation in specimen 2.....	126
Table A2. Fatigue crack propagation in specimen A.....	126
Table A3. Fatigue crack propagation in specimen C.....	126
Table A4. Fatigue crack propagation in specimen D.	126
Table A5. Fatigue crack propagation in specimen E.	126
Table A6. Fatigue crack propagation in specimen H.	126

LIST OF FIGURES

Figure 1. Actual service load history experienced by a gas pressure vessel.....	4
Figure 2. Schematic illustration of (a) growth of short cracks in smooth specimens as a function of fatigue life fraction and (b) crack velocity as a function of crack length	6
Figure 3. Stress concentration around a hole in a uniformly stressed plate.....	10
Figure 4. Modes of crack growth.....	14
Figure 5. Polar coordinates at the crack tip.....	16
Figure 6. Crack tip plastic zone shape	18
Figure 7. A fracture toughness vs. thickness graph	19
Figure 8. Schematic section through a fatigue fracture showing the three stages of crack propagation.....	21
Figure 9. Crack propagation behavior	23
Figure 10. Fatigue striations in (a) interstitial free steel and (b) aluminum alloy AA2024-T42	24
Figure 11. Laird’s proposed mechanisms of striation formation in the stage II of propagation: (a) no load; (b) tensile load; (c) maximum tensile load; (d) load reversion and (e) compressive load.....	25
Figure 12. Fatigue fracture surface: (a) high applied load; (b) low applied load	26
Figure 13. Limitations of fail-safety	29
Figure 14. Mean stress influence on fatigue crack growth rates.....	31
Figure 15. Schematic of the plastic zone at the tip of advancing crack: (a) loading cycle, (b) monotonic plastic zone, (c) cyclic plastic zone	34
Figure 16. Schematic representation of opening and effective stress intensity factors	37
Figure 17. Schematic representation of the mechanism of fatigue-crack closure according to Elber.....	38
Figure 18. General crack closure mechanisms: (a) transformation induced crack closure, (b) oxidation-induced crack closure, (c) fluid-induced crack closure, (d) roughness- or geometry-induced crack closure and (e) plasticity-induced crack closure	40
Figure 19. Corrosion fatigue crack growth rates for 4340 Steel in 3 wt% NaCl water solution.....	42
Figure 20. Schematic of electrolytic electrochemical cell	48

Figure 21. Types of corrosion: (a) uniform; (b) non-uniform; (c) selective leaching; (d) stain corrosion; (e) crevice corrosion, (f) pitting corrosion, (g) undersurface corrosion, (h) intergranular corrosion.....	53
Figure 22. The galvanic series in seawater	55
Figure 23. ASTM E399 compact tension specimen.	63
Figure 24. CT specimen loaded into clevis.....	65
Figure 25. ASTM E399 tension testing clevis	66
Figure 26. Fatigue cracking setup.....	66
Figure 27. MTS Model 632.02 clip-on displacement gage	69
Figure 28. Conditioning circuit of the MTS clip-on displacement gage	69
Figure 29. Knife edges installation	70
Figure 30. Compact-tension specimen with knife edges and displacement clip-on gage attached.....	70
Figure 31. Back-face strain gage attached to the ASTM E399 compact-tension specimen	72
Figure 32. Assembly steps for creating a treatment solution reservoir inside the specimen	72
Figure 33. The specimen opened using a static loading armature	73
Figure 34. Electrochemical treatment setup.....	74
Figure 35. Scanning electron microscopes: (a) TM-1000 (Hitachi Ltd, Tokyo, Japan); (b) Phenom Pro G2 (PhenomWorld Inc., Eindhoven, Netherlands); (c) S-4800 (Hitachi Ltd, Tokyo, Japan).....	76
Figure 36. A portion of the ASTM E399 compact tension specimen cut for scanning electron microscope imaging	77
Figure 37. The specimen molded with epoxy and ready to be polished.....	77
Figure 38. 60-1990 grinder-polisher (Buehler Inc., Lake Bluff, IL, USA) loaded with molded specimens.....	78
Figure 39. An example of a specimen mounted on an aluminum SEM specimen base using silver paint and prepared for imaging	79
Figure 40. Dimensions and geometry of the ASTM A36 steel specimen used for corrosion susceptibility testing	81
Figure 41. Schematic representation of the ASTM A36 steel specimen covered with epoxy resin	82
Figure 42. An example of a rectangular steel specimen covered with epoxy and placed into container with corrosive environment (3.5 wt% NaCl)	83
Figure 43. The steps of the finite element analysis: (1) subjecting a CT-specimen with a fatigue crack to static loading; (2) inserting a layer of nickel (simulating nickel deposition); (3) releasing static loading while nickel is deposited on crack surfaces.....	86

Figure 44. ASTM E399 compact-tension specimen and nickel deposit meshed in ANSYS	87
Figure 45. Nickel clump model meshed in ANSYS	88
Figure 46. The boundary conditions applied to the CT-specimen and nickel layer models at 3 steps of the dynamic transient finite element analysis	89
Figure 47. The boundary conditions applied to the CT-specimen and nickel clump at 3 steps of the dynamic transient finite element analysis.....	90
Figure 48. Fatigue crack propagation in specimen C without electrochemical treatment	92
Figure 49. 34 sets of fatigue crack growth data for ASTM A36 steel	93
Figure 50. Fatigue crack propagation in ASTM A36 steel CT specimen D before and after electrochemical treatment.....	95
Figure 51. Fatigue crack propagation in specimen C (not treated) and in specimen D (treated).....	97
Figure 52. Fatigue crack propagation in specimen E before and after electrochemical treatment	98
Figure 53. Fatigue crack propagation in specimen H before and after electrochemical treatment	100
Figure 54. The average number of cycles required to initiate a fatigue crack from a V-notch as compared to re-initiating a fatigue crack after electrochemical treatment	103
Figure 55. Comparison between the predicted and the actual numbers of reversals to failure (crack initiation) of ASTM E399 CT V-shaped starter notches.....	107
Figure 56. The relationship between the predicted and the actual values of reversals to failure (crack initiation) of starter V-shaped notches	108
Figure 57. The relationship between the predicted and the actual values of reversals to failure (crack initiation) of electrochemically treated fatigue cracks	111
Figure 58. Relationship between fatigue crack arrest life (number of cycles to re-initiate a fatigue crack after treatment) and theoretical stress intensity factor range (ΔK) applied for post-treatment cycling.....	112
Figure 59. Log-log plot of the relationship between fatigue crack arrest life (number of cycles to re-initiate a fatigue crack after treatment) and theoretical stress intensity factor range (ΔK) applied for post-treatment cycling.....	113
Figure 60. Starter notch radius of an ASTM E399 compact-tension specimen.....	114
Figure 61. SEM image of the fatigue crack tip (Specimen G) following nickel plating treatment	115
Figure 62. Optical microscope image of electrochemically treated fatigue crack.....	117
Figure 63. Optical microscope image of a portion of a fatigue crack packed with plating bath constituents (presumably with nickel)	118

Figure 64. Magnified optical microscope image extracted from Figure 63. This image shows deposit formation within the crack, the arc of the deposit and the radii at each surface	119
Figure 65. Scanning electron microscope image of an electrochemically treated fatigue crack within 5 mm of the crack tip	120
Figure 66. SEM image of the electrolytic nickel layer deposited onto an ASTM A36 steel specimen	121
Figure 67. Thickness variation of a nickel layer electrodeposited onto ASTM A36 steel plate	123
Figure 68. SEM image of electrochemically treated specimen fracture surface	126
Figure 69. ASTM A36 steel specimen with an electrochemically treated fatigue crack viewed from side	128
Figure 70. Normal stress distribution along X-axis (σ_x) in the ASTM E399 CT specimen with a V-shaped starter notch subjected to a static load of 6 kips	130
Figure 71. Crack packing schematic	131
Figure 72. Normal stress distribution along X-axis (σ_x) in ASTM E399 compact tension (CT) specimen with a fatigue crack packed with a nickel layer extending 10% of the crack length, starting at the tip.....	132
Figure 73. The relationship between the percentage of crack packing and the compressive stress developed at the new crack tip.....	137
Figure 74. Fatigue crack volume	138
Figure 75. The fatigue cycles required for re-initiation of treated fatigue cracks	142
Figure 76. The relationship between ΔK_{Ic} and the actual cycles required for crack re-initiation observed during experiments	152
Figure 77. Log-log plot of the relationship between ΔK_{Ic} and the actual number of crack re-initiation cycles observed during experiments.....	152
Figure 78. Schematic representation of discrete crack packing.....	145
Figure 79. Normal stress distribution along the X-axis (σ_x) in ASTM E399 CT specimen model with a fatigue crack held open by a wedge of nickel at the 3rd step of the transient analysis	152
Figure 80. Normal stress distribution along X-axis (σ_x) at the nickel wedge area	147
Figure 81. Normal stress distribution along X-axis (σ_x) within the nickel wedge.....	147
Figure 82. Corrosion potential of electrolytic nickel, nickel-plated ASTM A36 steel, and non-plated ASTM A36 steel in 3.5 wt% NaCl solution.....	152
Figure 83. Corrosion rates of electrolytic nickel, nickel-plated ASTM A36 steel and non-plated ASTM A36 steel	152
Figure 84. Average corrosion rates in simulated seawater solution (3.5 wt% NaCl).....	152
Figure 85. Nickel-plated ASTM A36 steel specimens with localized corrosion after 12 weeks in 3.5% NaCl solution.....	152

CHAPTER 1

INTRODUCTION

Fatigue is responsible for at least 50% of all mechanical and 90% of all metallic failures [1,2,3]. Fatigue cracks often start at stress concentrations, and without timely and appropriate remediation, tend to exhibit relatively fast propagation that may lead to property damage and sometimes to serious accidents.

The objective of this research was to develop a new method of fatigue crack treatment in steel structures and estimate its efficiency and limitations. The method was based on placing fatigue cracks under compression by electrodepositing nickel onto the surfaces of the cracks. It is conceivable that this new method of fatigue crack mitigation could be applied to any metallic structure. The application focus for this work was on steel pipelines.

CHAPTER 2

BACKGROUND

2.1 Metal Fatigue

2.1.1 Motivation to Study Metal Fatigue

Fatigue is a process of structural damage caused by cyclic stress or strain. These stresses and strains are usually amplified at surface and structural irregularities, such as notches, cracks, material non-homogeneities and other defects [1]. Under conditions of fluctuating local stresses material failure may be observed at a stress level significantly lower than the material's static yield strength of the material.

The process was call "fatigue" because the material appears to tire out after the repeated stress cycling. Fatigue gradually reduces mechanical, material and functional characteristics of all mechanical structures, such as spacecraft, aircraft, gas turbines and rocket engines, ground vehicles, pipelines, pressure vessels, offshore structures, and ship structures [4-8]. Fatigue was found responsible for at least 50% of all mechanical failures and 90% of all metallic failures [1-3].

There are a handful of fatigue types that are recognized in the literature. These include cyclic plasticity, contact fatigue, corrosion fatigue, and creep fatigue [1-3, 9, 10].

Fatigue failures are a threat to structures, human health and environmental safety. The relative cost of these failures constitutes approximately 4% of the US gross national product [11]. Moreover, fatigue failures can be catastrophic. Due to the small initial scale they usually progress undetected until large scale damage or a structural failure occurs [12].

Metal fatigue is mostly a descriptive subject. A significant volume of literature was accumulated especially over the past sixty years describing the mechanics and mechanisms of fatigue failure [11,12]. Two groups of metal fatigue descriptions can be differentiated: metallurgical and mechanical. Metallurgical descriptions characterize material mechanisms of metal fatigue on microstructural level. Mechanical descriptions focus on the structural response to cyclic loading with the main emphasis on prediction of the remaining life of a structure. The mechanical descriptions are more often used in engineering, as they can be used to predict service behaviors of structures and components via analytical and numerical models. These models are based on mechanical fatigue properties of materials that are obtained empirically.

High-pressure pipelines and storage vessels are often subjected to pressure fluctuations due to variations in supply and demand, vibrations, and fluid hammer effects (temporary change in pressure due to a sudden change in fluid velocity) [13, 14]. In regard to simple pressure fluctuations, the maximum pressure of a high-pressure pipeline is typically observed overnight and varying minimum pressures are observed during the daytime. A typical service load history of a gas pressure vessel is presented in Figure 1.

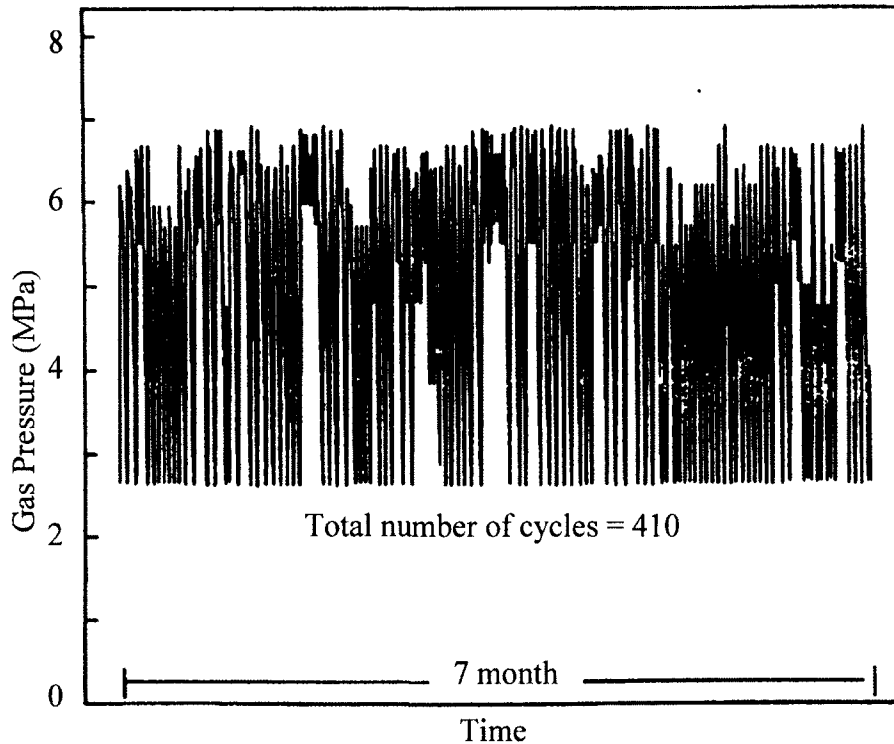


Figure 1. Actual service load history experienced by a gas pressure vessel [13]. Reprinted from, N.A. Fleck, R.A. Smith, "Fatigue life prediction of a structural steel under service loading", p.203, 1984, with permission from Elsevier.

Fatigue is often a cause of pipeline accidents. For instance, Table 1 presents a list of major pipeline accidents that occurred in the USA and were caused by fatigue cracks during the last 14 years [15-21]. According to the National Transportation Safety Board, the total cost of these accidents was around \$807 million.

Table 1. Major pipeline accidents in the USA caused by fatigue cracks

Year	Type of a pipeline	Location	Reference
2000	Petroleum pipeline	Greenville, TX	[15]
2000	Crude oil pipeline	Winchester, KY	[16]
2001	Petroleum pipeline	Knoxville, TN	[17]
2002	Crude oil pipeline	Cohasset, MN	[18]
2004	Ammonia pipeline	Kingman, KS	[19]
2009	Natural gas pipeline	Palm City, FL	[20]
2010	Petroleum pipeline	Marshall, MI	[21]

In the practice of pipeline utilization the majority of these pipeline failures tended to occur without any obvious reasons: the internal pressure did not exceed the design level, there were no plastic macro-deformations associated with damage in the failure zone and the mechanical properties of the pipe did not exhibit any problems [22]. The damage was usually caused by cyclic loading and fractures originating from fatigue crack initiation and growth. The number of loading cycles per year in pipelines under normal working conditions often reaches the level of 10^3 - 10^6 cycles per year [23]. The starting locations of fatigue cracks are usually at initial defects of the base material or at process defects which may appear during welding or assembly. Other operational defects can be caused by a corrosive environment or overloading. Cracks propagate over a period of time which defines the remaining life of the structure. In order to forecast the growth of fatigue cracks it is necessary to have information about growth rates under cyclic loading. This data can be obtained empirically or by using a theoretical model.

The fatigue process is usually divided into three stages: crack origination (initiation), crack propagation, and rapid unstable fracture (or failure). Each fatigue stage is often easily distinguishable and governed by separate factors and processes.

2.1.2 Crack Initiation

The major portion of the fatigue life of smooth specimens, in the absence of surface defects, consists of the initiation of surface cracks and their propagation to the “engineering” size (2-3 mm deep) [24,25]. Fatigue life mainly consists of two stages: initiation of surface microcracks and their propagation to the engineering size. In order to understand fatigue, it is necessary to study the mechanisms that operate during crack initiation.

Recently Chopra and Raman observed that surface microcracks ($>10\ \mu\text{m}$) form rather early on smooth specimens when subjected to cyclic loading [24,26]. Typically the microcrack formation period was within the first 10% of the fatigue life of the material. The initiation of the surface microcracks was usually observed at surface imperfections or discontinuities formed during fabrication process or produced by cyclic loading. The authors concluded that the fatigue life of a crack mainly consisted of propagation from $10\ \mu\text{m}$ to $3\ \text{mm}$ in length [27]. A schematic illustration of these two stages of fatigue crack life is shown in Figure 2.

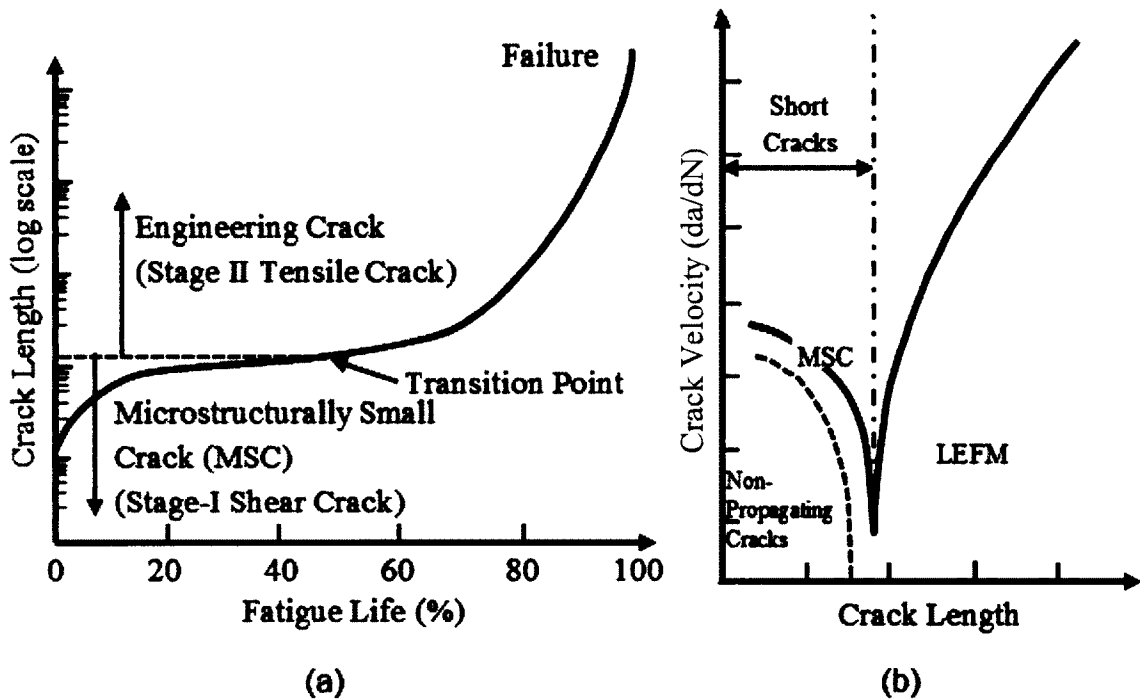


Figure 2. Schematic illustration of (a) growth of short cracks in smooth specimens as a function of fatigue life fraction and (b) crack velocity as a function of crack length. LEFM = Linear Elastic Fracture Mechanics [25]. Adapted from O K Chopra, "Mechanism and estimation of fatigue crack initiation in austenitic stainless steels in LWR environments", p. 19, 2001, with kind permission from Argonne National Library, managed and operated by Uchicago Argonne, LLC, for the U.S. Department of Energy under Contract No. DE-AC02-06CH11357.

The growth of microstructurally small cracks (MSCs) is observed during the crack initiation stage. This stage is characterized by a crack growth velocity that is reducing in magnitude as the crack increases in length (MSC region in Figure 2b) [25]. The growth of the engineering cracks is observed during the propagation stage which is characterized by accelerating crack growth (LEFM region in Figure 2b). The growth rate of MSCs depends on the material microstructure [25, 28, 29]. Fatigue cracks longer than the critical length of MSCs are termed engineering cracks. The propagation of engineering cracks is not influenced by material microstructure. Cracks above this size are characterized by the formation of striations on the fatigue surface. This surface is normal to the maximum principal stress. Engineering cracks propagate in Stage II region (see Figure 2a).

Following its initiation the surface microcrack continues to propagate as a shear crack in the Stage I region. Microcracks usually propagate at a 45° angle to the principal stress axis [25]. A Stage I crack may grow along the boundary of several grains if the strain amplitude is low. The increasing stress intensity factor affects the growth of the microcrack by promoting the crack growth in the direction perpendicular to the principal stress. At this transition point the crack starts propagating as a tensile crack, perpendicular to the principal stress axis in the Stage II growth region.

Numerous criteria have been developed to estimate the crack size at the moment of transition from a MSC to an engineering crack [25]. These criteria demonstrated relationships between a transition crack length, the applied stress and the microstructure of a material. Typical values of the transition crack length for steel were found to vary from 150 to 250 μm .

The relationship between the total strain amplitude and the number of stress reversals to failure (defined as the initiation of an engineering fatigue crack of 2 mm or longer) was found by Morrow [30]. It is presented by Eq. (1):

$$\frac{\Delta\varepsilon}{2} = \frac{\sigma_f' - \sigma_m}{E} (2N_f)^b + \varepsilon_f' (2N_f)^c \quad (1)$$

where E is the Young's modulus of elasticity, σ_f' is the fatigue strength coefficient, σ_m is the mean stress, b is the fatigue strength exponent, ε_f' is the fatigue ductility coefficient, c is the fatigue ductility exponent, $\frac{\Delta\varepsilon}{2}$ denotes the total strain amplitude and $2N_f$ is the number of reversals to failure (1 cycle = 2 reversals). The first and the second functions of $2N_f$ on the right side of Eq. (1) represent the elastic and plastic components of the strain amplitude respectively.

At low stress levels MSCs do not transform to engineering cracks (see Figure 2) [25]. This condition is responsible for the fatigue limit that is observed for smooth specimens. In order for a microcrack to grow to the engineering size it must be subjected to a stress higher than the endurance limit stress of the material. Interestingly, if the crack is longer than the transition crack length the propagation can occur at a stress that is lower than the fatigue limit. The growth of such cracks is described with linear-elastic (LEFM) or elastic-plastic fracture mechanics (EPFM).

2.1.3 Linear Elastic Fracture Mechanics Concepts

The analysis and application of fatigue crack propagation rates and threshold data in laboratory specimens and structures became much easier with the development of fracture mechanics through the pioneering work of Griffith (1921 to 1924) and its

development to the practical form by Irwin (1957, 1958) and Rice (1968) [31-33]. Linear Elastic Fracture Mechanics (LEFM) is a theory that describes behavior of sharp cracks in elastic bodies [11]. It is limited to linear elastic material conditions when they apply during the fatigue process. These conditions become violated in the presence of plastic deformation, crack growth or material fracture. For such circumstances elastic-plastic fracture mechanics (EPFM) approaches the most accurate characterization of fatigue and fracture processes. Since the beginning of the 20th century fracture mechanics has been extensively applied to almost all engineering fields, including construction, aerospace, and nuclear industry.

The foundation of the quantitative definition of material toughness was established by the work of Inglis in 1913 [34]. He demonstrated the stress magnification that occurs at the edge of the hole. Also, using elastic theory he found that the stress concentration at the edge of the hole was higher as the radius of curvature became smaller (see Figure 3).

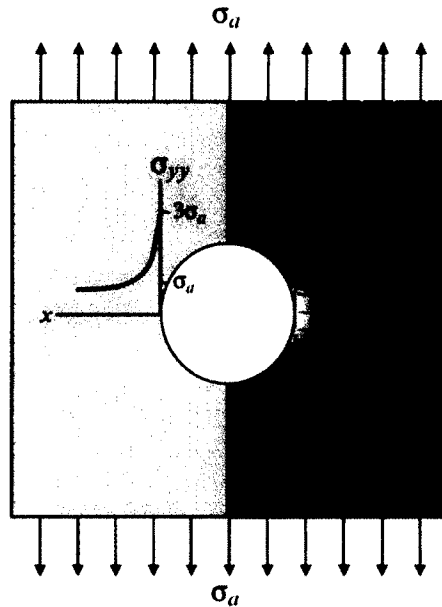


Figure 3. Stress concentration around a hole in a uniformly stressed plate. The contours for σ_{yy} shown here were generated using the finite-element method. The stress at the edge of the hole is three times the applied uniform stress [35]. Reprinted from “Linear Elastic Fracture Mechanics”, 2007, p. 32, Chapter 2, A C Fischer-Cripps, Figure 2.2.1., with kind permission from Springer Science and Business Media (License # 3417821256858).

Inglis developed a formula for the stress concentration factor, K , for an elliptical hole (Eq. (2)):

$$K = 1 + 2 \sqrt{\frac{c}{p}} \quad (2)$$

where c and p are the major and the minor radii of an elliptical hole. The stress concentration factor can be greater than one for small elliptical holes. Using Eq. (2) it can be found that the stress concentration of a circular hole, K is equal to three (as shown in Figure 3). From Eq. (2) it can be noticed that the stress concentration depends only on the ratio of the local dimensions of the hole, particularly the hole radii. The stress concentration factor is not related to the length or depth of the hole.

Equation (3) represents a formula for the stress concentration factor (K_{tg}) of an elliptical or U-shaped notch in a semi-infinite thin structure subjected to tension:

$$K_{tg} = 0.855 + 2.21 \sqrt{\frac{t}{r}} \quad (3)$$

where t is the depth of a notch and r is the radius of a notch [36-38].

Stress concentration factors K and K_{tg} account only for elastic stresses. Fatigue damage can also occur if localized plasticity is present, such as within a notch. Thus in order to relate the purely elastic stress concentration factor to fatigue crack initiation where plasticity is involved a modification that would take into account plasticity is needed. In 1961 Neuber proposed a model describing the local stress and strain concentration factors, K_σ and K_ϵ , and their relationship to the theoretical elastic stress concentration factor, K_t , (see Eq. (4)) [39]:

$$K_t^2 = K_\sigma K_\epsilon. \quad (4)$$

Neuber's rule (Eq. (4)) states that the squared theoretical elastic stress concentration factor is equal to the product of the local stress (K_σ) and the local strain (K_ϵ) concentration factors. The local concentration factors denote the relationships between the local and the remote (outside of the notch) stress and strain ranges respectively.

Equation (4) can be expanded:

$$K_t^2 = \left(\frac{\Delta\sigma}{\Delta S}\right) \left(\frac{\Delta\epsilon}{\Delta e}\right) \quad (5)$$

where $\Delta\sigma$ and ΔS are the local true stress and the remote engineering stress ranges (respectively), $\Delta\epsilon$ and Δe are similarly the respective local true strain and remote engineering strain ranges. Equation (5) can be rewritten into a convenient form:

$$\Delta\sigma\Delta\varepsilon \cong \frac{(K_t\Delta S)^2}{E} \quad (6)$$

where E denotes the Young's modulus of elasticity. Neuber's rule is often employed for estimation of elastic-plastic stresses and strains at notch roots. It usually provides a reasonable approximation if yielding of the material is localized (within the notch region only). Other versions of Neuber's rule may provide a reasonable approximation of stresses and strains when a large portion of the material (outside of the notch) undergoes yielding.

The local strain at the notch subjected to cyclic loading may be determined from empirically obtained cyclic stress-strain curves or can be approximated by application of the Ramberg-Osgood relationship shown in Eq. (7) [40]:

$$\frac{\Delta\varepsilon}{2} = \frac{\Delta\sigma}{2E} + \left(\frac{\Delta\sigma}{2K'}\right)^{1/n'} \quad (7)$$

where K' is the fatigue strength coefficient and n' is the fatigue strain hardening exponent. These and other fatigue properties of ASTM A36 steel used in this study are shown in Table 2 [41].

Table 2. The fatigue properties of ASTM A36 steel [41].

Property name	Designation	Value
Fatigue strength coefficient	K'	159 ksi
Fatigue strain hardening exponent	n'	0.249
Fatigue strength coefficient	σ'_f	147 ksi
Fatigue ductility coefficient	ε'_f	0.271
Fatigue ductility exponent	c	-0.451
Fatigue strength exponent	b	-0.132

The local stress range ($\Delta\sigma$) at the notch root can be estimated using a combination of Eq. (6) and (7), achieved by eliminating the $\Delta\varepsilon$ from these expressions, as shown in Eq. (8):

$$\Delta\sigma = \left\{ E \left[\frac{(K_t \Delta S)^2}{E} - 2 \left(\frac{(\Delta\sigma)^{\frac{n'+1}{n'}}}{(2K')^{1/n'}} \right) \right] \right\}^{1/2} \quad (8)$$

Equations (1, 7, 8) can be solved numerically for the analysis of local elastic-plastic stresses and strains at the notches, and for prediction of fatigue lives of notched specimens.

In 1920 Griffith proposed that the amount of strain energy reduced due to the formation of new crack surfaces (at the moment of crack propagation) must be equal to or greater than the amount of surface energy required in the process of forming new crack faces [33]. According to Griffith, there are two required conditions for crack growth:

1. The material bonds at the crack tip must be subjected to a stress high enough to cause failure. Griffith found that the stress at the crack tip depends on the stress concentration factor which is inversely proportional to the ratio of crack tip radius to the length of that crack.
2. For a crack to grow, the amount of strain energy released per increment of crack extension must be equal or larger than the amount of surface energy required for formation of new crack faces. This condition is formulated by Eq. (9):

$$\frac{dU_s}{dc} \geq \frac{dU_\gamma}{dc} \quad (9)$$

where U_s is the strain energy, U_γ is the surface energy, and dc is the crack length increment.

The energy balance criterion defines if crack growth is theoretically possible, however for a crack to grow the crack tip must be subjected to a sufficient stress. A crack will only propagate when the bonds at the crack tip will be subjected to a load greater than their maximum tensile strength. Even if there is enough strain energy accumulated to facilitate crack growth a sufficient concentration of local stress is required to drive crack propagation. Crack blunting may increase the crack tip radius and prevent crack growth due to an insufficient stress concentration at the crack tip.

There are three typical modes of crack surface displacement which can cause crack growth; these are shown in Figure 4.

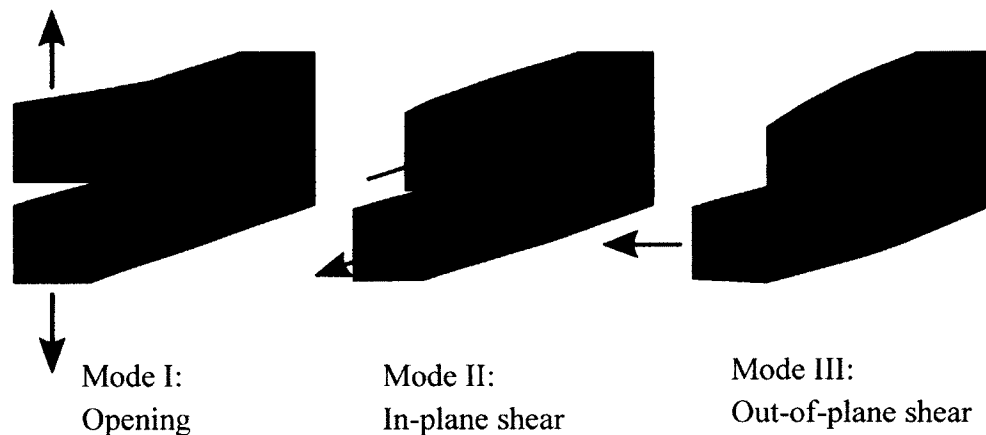


Figure 4. Modes of crack growth [42]. Reprinted from “Encyclopedia of Physics (Handbuch der Physik)”, 1958, Vol. VI, Flugge Ed., G R Irwin, Figure 3, with kind permission from Springer (License # 3512730373630).

- I. The opening mode. The crack surfaces move directly away from each other.
- II. The edge sliding mode or in-plane shear mode. The crack surfaces move parallel to the crack.
- III. The out of plane shear mode or tearing mode. The crack surfaces move apart in the crack plane.

Mode I is the most common type of crack growth encountered in engineering design, mostly because cracks tend to grow on the plane of maximum tensile stress. Mode II displacements can only be observed at internal or at very deep external cracks [10]. Mode III crack growth is typical for a cylindrical notched bar loaded in torsion. Combinations of these crack extension modes can also occur.

In 1940's, during the Second World War, George R. Irwin developed one of the key concepts of fracture mechanics during his study of steel armor penetrated by ammunition [43]. Experiments Irwin conducted at the U.S. Naval Research Laboratory in Washington, D.C. helped him to formulate the theory of fracture mechanics that is now applied in various industries [31]. Irwin mathematically described the stress field in the region of an infinitely sharp crack tip (see Eq. (10)):

$$\sigma_{yy} = \frac{K_I}{\sqrt{2\pi r}} \cos \frac{\theta}{2} \left(1 - \sin \frac{\theta}{2} \sin \frac{3\theta}{2} \right) \quad (10)$$

where $\frac{K_I}{\sqrt{2\pi r}}$ characterizes the magnitude of the stress, while all the terms containing θ describe its distribution. The Mode I stress intensity factor, K_I can be expressed as Eq. (11):

$$K_I = \sigma_a Y \sqrt{\pi c} \quad (11)$$

where σ_a is the externally applied stress, Y is a geometry factor, and c is the crack half-length. The subscript I in K_I is associated with tensile loading, as shown in Figure 4. Stress intensity factors exist for other types of loading, but K_I is the most often used as Mode I crack growth is the most common type that leads to brittle fracture. K is conventionally expressed in $\text{ksi}\sqrt{\text{in}}$ in the imperial measurement system. Equation (11)

describes the stress distribution and its magnitude in the vicinity of the crack tip. The stress at an “infinitely sharp” crack goes to infinity due to the singularity existing at the crack tip [35]. The stress intensity factor may be considered as a measure of the magnitude of that singularity. The stress intensity factor K_I accounts for both applied stress and crack length that define the magnitude of the stress at a point located at (r, θ) polar coordinates near the crack tip region, as shown at Figure 5.

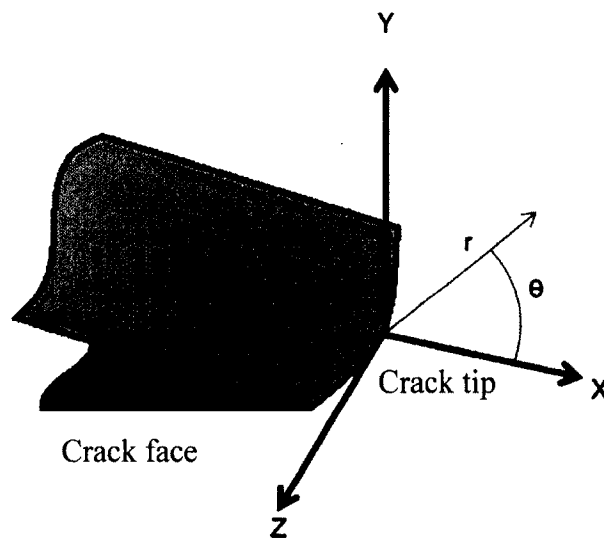


Figure 5. Polar coordinates at the crack tip.

The stress distribution around the crack tip is the same for all sharp cracks. It does not depend on crack length [35]. There is a critical value for K_I for each material that corresponds to the energy balance criterion. That critical value of K_I characterizes the fracture strength of the material.

2.1.4 Crack Tip Plasticity

According to Eq. (4) the stress σ_{yy} at the crack tip (i.e. $r = 0$) goes to infinity. In reality, it is limited by material yielding strength, and hence the limiting condition of linear elasticity is violated in the crack tip zone [44]. That zone is experiencing non-linear (plastic) stress conditions and is often called the “crack tip plastic zone”. The form and the size of the plastic zone can be determined from models proposed by Irwin [43]. Equation (12) can be used to estimate the size of the plastic zone:

$$r_p = \frac{K_I^2}{2\pi\sigma_{ys}^2} \quad (12)$$

where σ_{ys} is the tensile yielding strength of the material. Using the stress field Eq. (10) and the von Mises or the maximum shear stress yield criteria, plastic zone shape can be determined. The plastic zone shape for Mode I resulting from the von Mises criterion is shown in Figure 6. For plane stress conditions (when $\sigma_z = 0$) a much larger plastic zone exists compared to the plane strain condition, where the tensile stress component, σ_z , restricts yielding.

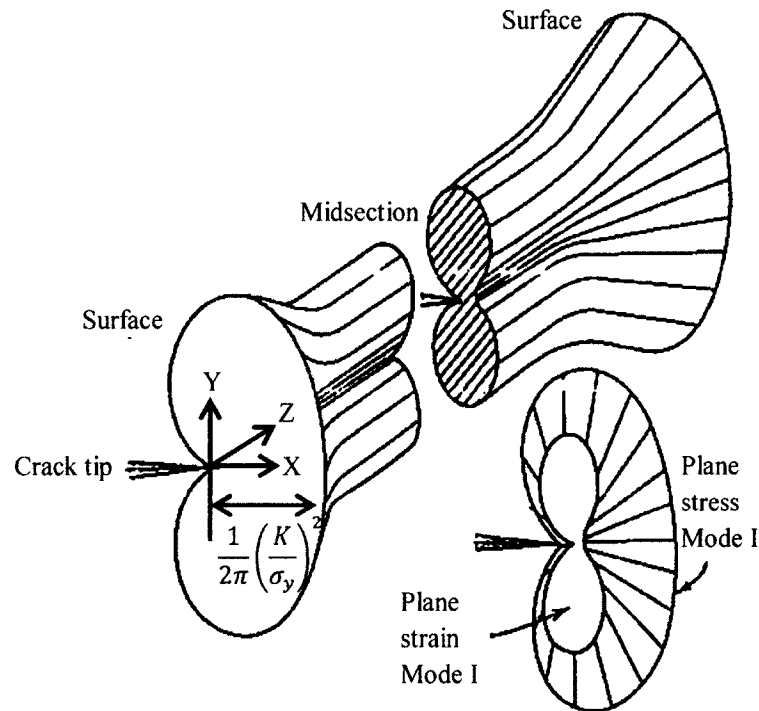


Figure 6. Crack tip plastic zone shape [45]. Reprinted from “Metal Fatigue in Engineering”, 2nd ed., 2000, p. 75, Chapter 4, R I Stephens, with kind permission from “John Wiley and Sons” (License # 3492881307833).

There is still not much attention of engineers paid to plasticity; however it remains an important issue in fracture mechanics. The degree of plasticity relative to specimen and crack dimensions characterizes the state of stress (plane strain or plane stress) and defines applicability of LEFM [45]. Plane stress condition is observed when the size of the plastic zone approaches the value of the material thickness. When the size of the plastic zone becomes comparable to the crack length, the LEFM assumptions are voided and yielding fracture mechanics (YFM) parameters must be used.

2.1.5 Fracture Toughness

The value of K_I at the point of rapid, unstable crack extension is called the critical stress intensity factor, K_C . It defines the beginning of crack extension. K_C is typically

considered as a specimen property as opposed to a pure material property and can be applied for characterization of material fracture toughness of a specific component.

Fracture toughness is used to quantitatively describe the resistance of a material component to brittle fracture. This can be expressed by:

$$K_c = \sigma_c \sqrt{\pi a_c f\left(\frac{a_c}{w}\right)} \quad (13)$$

where σ_c is the applied nominal stress at crack instability, a_c is the crack length at instability, K_c is the fracture toughness that depends on the material, temperature, strain rate, environment, and thickness. The dependence of the fracture toughness on specimen thickness was only observed in thin specimens, as shown in Figure 7.

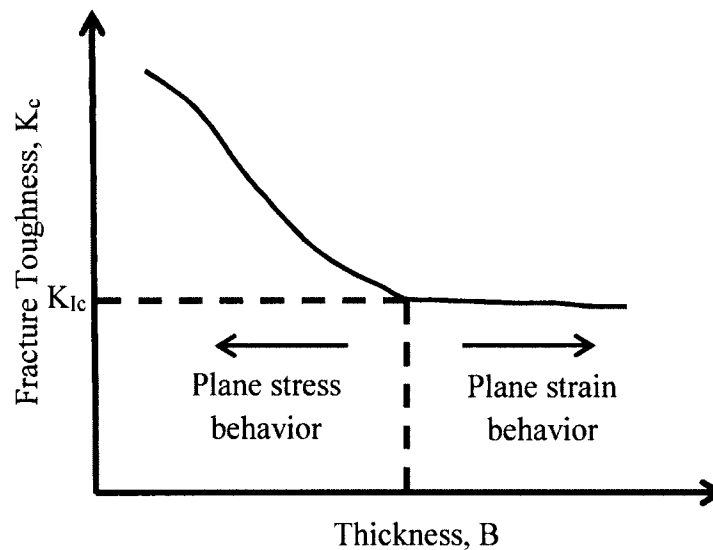


Figure 7. A fracture toughness vs. thickness graph [46]. Reprinted from “Material Science and Engineering: An Introduction”, 1994, 3rd ed., W Callister, with kind permission from John Wiley & Sons.

It was observed that thin components usually have higher value of K_c due to the beneficial effects of “shear lips” and slant fracture. When specimen thickness increases,

the ratio between the area of "shear lips" and the area of fracture surface decreases resulting in a lower K_c value. When both slant and flat fracture surfaces are observed the fracture appearance is called *mixed-mode*. For thick parts, the entire fracture surface is flat and K_c approaches the minimum value, called the "plane strain fracture toughness", K_{Ic} . It is considered a true material property due to its independence from specimen thickness. ASTM Standard E399 contains detailed specifications for the specimen geometry, experimental procedure, and data collection, and for techniques used to determine valid K_{Ic} values [47].

2.1.6 Fatigue Crack Growth

Fatigue crack growth characterization remains a largely empirical art within science, despite being a relatively old subject with more than 150 years of history described in numerous publications [48-52].

In the 1950's Forsyth concluded that fatigue crack propagation in metals is a two stage process, as demonstrated in Figure 8 [53, 54].

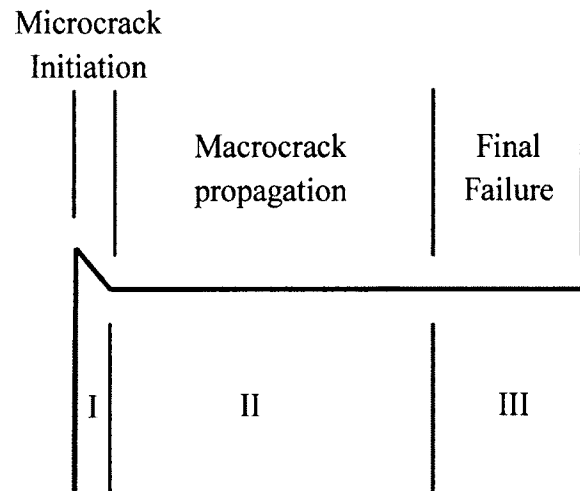


Figure 8. Schematic section through a fatigue fracture showing the three stages of crack propagation [55]. Reprinted from “Why Metal Fatigue Matters”, 2007, p. 163, Chapter 9, L Pook, with kind permission from Springer Science and Business Media (License # 3417880758984).

At Stage I a microcrack initiated from a surface crack propagates without changing direction in the plane of maximum shear stress (often located at 45° angle to the applied tensile load) [56]. A Stage I crack becomes a Stage II crack when it reaches a critical length, changes direction and starts to propagate normal to the maximum principal tensile stress. In fracture mechanics this stage is called Mode I. The maximum length of a Stage I crack (before transition to Stage II) strongly depends on microstructural features and on stress conditions. Many authors observed that the maximum length of a mode I crack exhibits wide variability [57-61]. The maximum length of a Stage I crack is usually less than 0.25 mm and is typically around 0.02 mm. After the transition a Stage II crack propagates through the main portion of the cross-section. Some authors use more descriptive terms for stages of crack propagation, such as *Microcrack* (Stage I), *Macrocrack* (Stage II) and *Engineering Crack* (Stage II crack longer than 2 mm). When the crack propagates to the point where the cross-section

becomes so reduced that conditions for failure in one load cycle are satisfied it reaches the 3rd Stage of crack propagation. This Stage is typically the shortest as rapid unstable crack propagation and specimen failure caused by brittle fracture or ductile collapse are usually observed at this point [55].

In 1960's fatigue crack life prediction was made easier and more quantitative.

Paris proposed using the range of Irwin's stress intensity factors, $\Delta K = K_{max} - K_{min}$ to characterize the rate of crack growth per cycle (da/dN), since a large amount of data fell into a single power law in the $da/dN - \Delta K$ diagram [62, 63]. The basic Paris law equation is presented by Eq. (14):

$$\frac{da}{dN} = C \Delta K^m \quad (14)$$

where a is the crack length and N is the number of loading cycles. The term on the left side is the crack growth rate. It defines the speed of crack propagation in inches per cycle. The right term of the equation consists of the material constants C and m and the stress intensity factor range, ΔK . This range is the difference between the stress intensity factors at maximum and minimum loading, $\Delta K = K_{max} - K_{min}$.

Currently the process of fatigue crack propagation is usually described by the Paris Law and represented by logarithmic da/dN vs. ΔK diagrams (Figure 9).

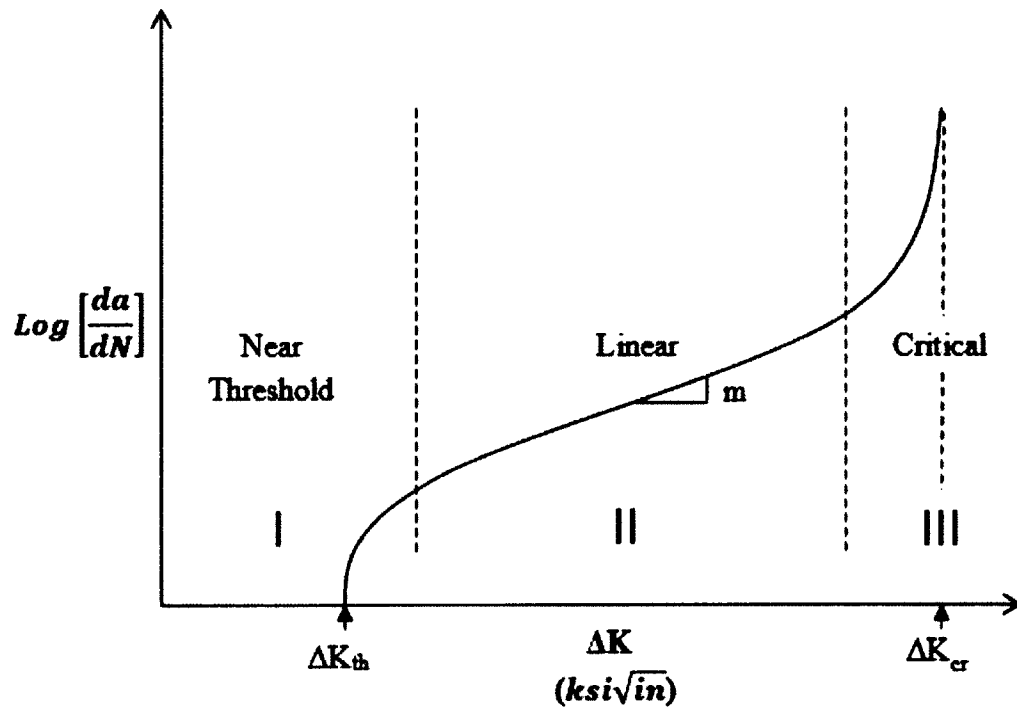


Figure 9. Crack propagation behavior [63]. Reprinted from “A generalized Paris’ law for fatigue crack growth”, 2006, p. 1339, N. Pugno, with kind permission from Springer Science and Business Media (License #3417881400121).

The near threshold region (Region I) is that region of the curve typically below 10^{-8} in/cycle (10^{-10} m/cycle). In this region the value of the stress intensity factor range (ΔK) is not sufficient to drive crack propagation.

The linear, also called “Paris region” (Region II) contains data where the crack propagates with a linear rate. The behavior of the cracks propagating in this region is usually described well by the Paris Law [64]. Crack propagation in this region is marked with formation of surface striations (also called beach marks). These striations can be observed via optical or scanning electron microscopy. Each striation corresponds to one stress cycle. The distance between striations is the dimension of crack propagation increment. This direct relation between striations and number of applied stress cycles was

observed and studied by many authors [65]. Fatigue striations cannot be seen in all engineering materials, however they are usually clearly observed in most metals. In steels, fatigue striations can often be found in cold-worked alloys. Figure 10 contains examples of fatigue striations in interstitial-free steel and in aluminum alloys [66].



Figure 10. Fatigue striations in (a) interstitial-free steel; (b) aluminum alloy AA2024-T42 [66]. Reprinted from "Fatigue-Crack Propagation in Steels of Various Yield Strengths," by J M Barsom, *Journal of Manufacturing Engineering*, Volume 93, 2010, with kind permission from ASME Publications.

The most commonly accepted mechanism of formation of fatigue striations on the surfaces of ductile metals is the repeating process of crack tip blunting and re-sharpening, as represented in Figure 11. It was first proposed by Laird [66].

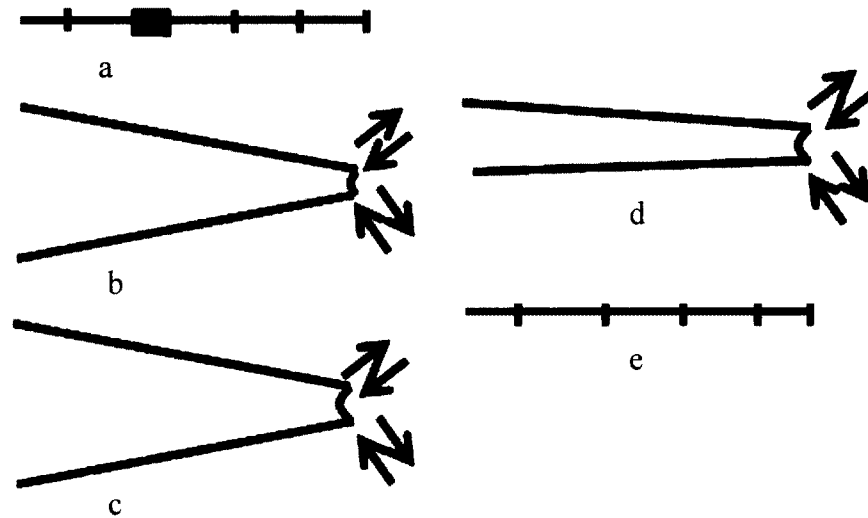


Figure 11. Laird's proposed mechanisms of striation formation in Stage II of crack propagation: (a) no load; (b) tensile load; (c) maximum tensile load; (d) load reversal and (e) compressive load [66]. Reprinted from "Fatigue-Crack Propagation in Steels of Various Yield Strengths," by J.M. Barsom, *Journal of Manufacturing Engineering*, Volume 93, 2010, with kind permission from ASME Publications.

The final region (Region III) of the crack growth curve is governed by the fracture toughness of the material. In this region the material is in a state of rapid unstable fracture (extremely rapid crack propagation).

Two distinct regions are usually observed on fatigue fracture surface. These are shown in Figure 12. The first region appears like a smooth surface, sometimes with the presence of large striations (beach marks). This morphology is associated with stable fatigue crack propagation. The other region indicates the location where the material failure occurred. The fatigue surface in that region is rough (fibrous) and irregular. Mechanical properties of the material as well as specimen dimensions and loading conditions characterize the type of fracture in this region. It can be either ductile or brittle in nature. The ratio between the surface areas of smooth and fibrous fracture relates to the applied load level. High applied load entails fast crack propagation due to a high value of

the stress intensity factor. This results in a small area of stable crack propagation, as shown in Figure 12a. At a lower load the crack will need to be longer in order for the stress intensity factor to reach the critical value of the fracture toughness of the material. This will result in a larger smooth fatigue surface region, Figure 12b [66].

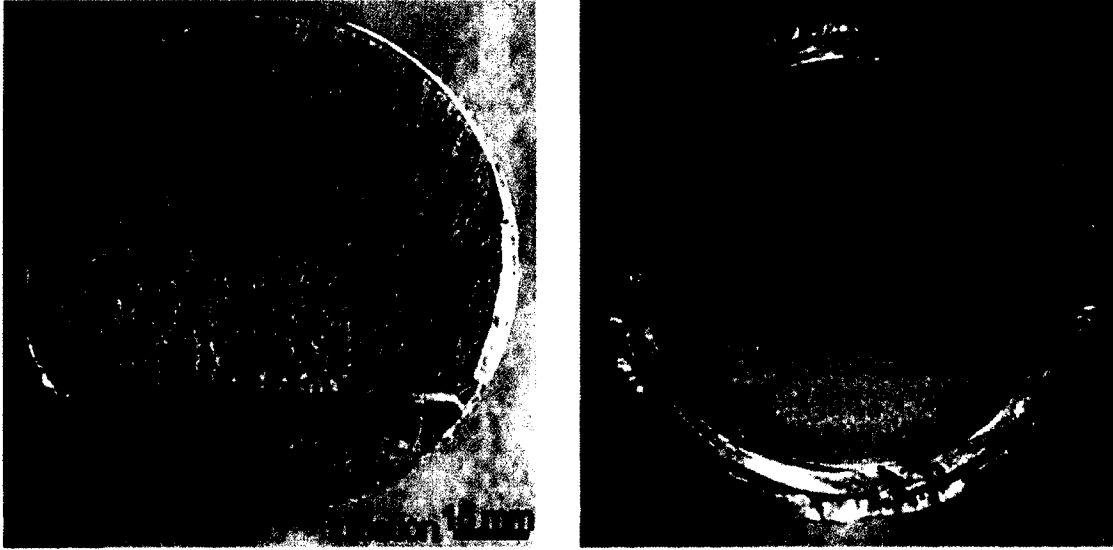


Figure 12. Fatigue fracture surface: (a) high applied load; (b) low applied load [66]. Reprinted from "Fatigue-Crack Propagation in Steels of Various Yield Strengths," by J.M. Barsom, *Journal of Manufacturing Engineering*, Volume 93, 2010, with kind permission from ASME Publications.

For a crack to propagate two conditions need to be satisfied: enough energy needs to be available to operate the crack propagation mechanism (thermodynamic criterion), and the stress magnitude at the crack tip must be large enough to operate this mechanism crack propagation (stress criterion) [67].

Since its development the Paris Law was extensively studied and different modifications were put forward. Forman, Walker, Erdogan, and other authors have

proposed their modifications to the Paris Law [63,68-71]. A list of some Paris' Law modifications and variations is shown in Table 3.

Table 3. Paris' Law modifications and variations.

($\frac{da}{dN}$ – crack propagation rate; ΔK – stress intensity factor range; K_{th} - threshold stress intensity factor; K_{max} , K_{min} – maximum and minimum values of the stress intensity factor; K_c – material fracture toughness; $C, C_1, C_2, m, n1, n2$ – empirical exponents; R – stress ratio; G – elastic strain energy release rate, p, q – material constants, ΔS – remote stress range)

Equation	Author
$\frac{da}{dN} = C(\Delta K)^m$	Paris [64]
$\frac{da}{dN} = C(\Delta K)^m \left(1 - \frac{\Delta K_{th}}{\Delta K}\right)^p$	Fleck [13]
$\frac{da}{dN} = C \left(\frac{\Delta K}{(1-R)^{1-p}}\right)^m$	Walker [70]
$\frac{da}{dN} = C \left(\frac{\Delta K^m}{(1-R)K_c - \Delta K}\right)$	Forman [69]
$\frac{da}{dN} = C \left(\left(\frac{1-f}{1-R}\right) \Delta K\right)^m \left[\left(1 - \frac{\Delta K_{th}}{\Delta K}\right)^p / \left(1 - \frac{K_{max}}{K_c}\right)^q\right]$	FNK/NASGRO [72]
$\frac{da}{dN} = \frac{C_1}{\Delta K^{n1}} + \frac{C_2}{\Delta K^{n2}} - \frac{C_2}{[K_c(1-R)]^{n2}}$	Saxena [73]
$\frac{da}{dN} = C(\Delta K - K_{th})^2 \left(1 + \frac{\Delta K}{K_c - K_{max}}\right)$	McEvily [74]
$\frac{da}{dN} = C(\Delta K^p \Delta K_{max}^q)$	Roberts [75]
	Klesnil [76]
$\frac{da}{dN} = C(K_{max}^2 - K_{min}^2)^m$	Arad [77]
$\frac{da}{dN} = C(\Delta G)^m$	Mostovoy [78]
$\frac{da}{dN} = C(\Delta S)^m$	Badaliance [79]

2.1.7 Crack Growth Life Integration

One of the goals of failure analysis is to predict fatigue life for some structural components. Under constant amplitude loading conditions and with a suitable fatigue crack growth law in hand, the fatigue life of a structure can be found by integration of the fatigue crack growth rate model from the initial to the final crack lengths (Eq. (15)):

$$N_f = \int_{a_0}^{a_f} \frac{da}{f(\sigma, a)} \quad (15)$$

where N_f is the number of cycles before failure, a_f is the critical crack length at which momentary failure will occur, and a_0 is the initial crack length. The initial crack length usually varies from 1 μm to 1 mm, depending on material defects present.

Using the Paris Law formulation (Eq. (14)), the number of cycles to failure, N_f , can be expressed by Eq. (16):

$$N_f = \int_{a_0}^{a_f} \frac{da}{C(\Delta K)^m} \quad (16)$$

where C and m are power law coefficients, and ΔK is the stress intensity factor range ($K_{max} - K_{min}$). Equation (16) often needs to be solved numerically.

Another method for fatigue crack growth prediction under constant-amplitude loading involves approximating the number of cycles for each increment of crack advance. The values of dN for each increment are then summed up for an approximate solution for the number of loading cycles of crack growth between any two lengths, a_0 and a_f [80].

In real applications mechanical structures are usually subjected to random loading amplitudes. This complicates the fatigue life calculation, requires more computational resources, and results in less reliable approximations. One of the common methods of crack growth prediction under variable amplitude loading conditions is the application of a cycle-by-cycle prediction method. This method is based on evaluation of the crack growth increment (da/dN) using ΔK , and R (loading ratio, K_{min}/K_{max}) values at each cycle of the variable amplitude history. If crack propagation is relatively slow, routine inspections and maintenance may be conducted in order to prevent operational failures. In the aircraft industry this practice has led to the well-known fail-safe philosophy. The concept of that approach is illustrated in Figure 13 [60].

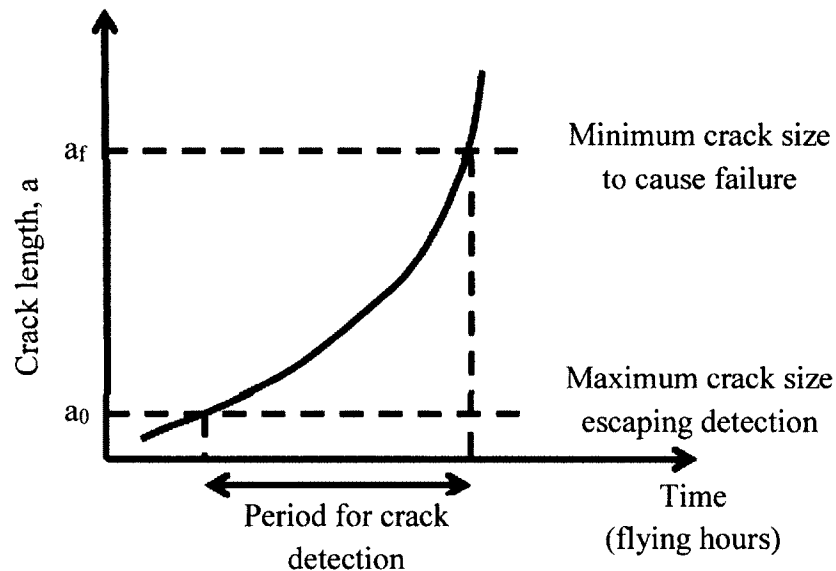


Figure 13. Limitations of fail-safety [60]. Reprinted from “Observations on the Prediction of Fatigue Crack Growth Propagation Under Variable-Amplitude Loading”, 1976, J Schijve, with kind permission from ASTM International.

The time period available for crack detection depends on both a_0 and a_f . Without sophisticated laboratory inspections fatigue cracks can be detected only when they reach

engineering size (~2-3 mm). However the major portion of the fatigue life often consists of the propagation of surface microcracks to the engineering crack size. For this reason the crack detection period mainly depends on the a_o size. It appears to be possible to reduce the number of required inspections, as well as the period between them, by reducing the crack propagation rate. This can lead to material, labor and financial savings.

2.1.8 Mean Stress Effect

A major loading parameter that affects the fatigue crack growth rate is the stress ratio ($R = \sigma_{min}/\sigma_{max}$) [81]. The effect of the mean stress is characterized by this parameter. Mean stress influence on fatigue crack growth is very important, and each mechanical design approach should take it into account. The general influence of the mean stress on fatigue crack growth behavior is shown schematically in Figure 14 [11].

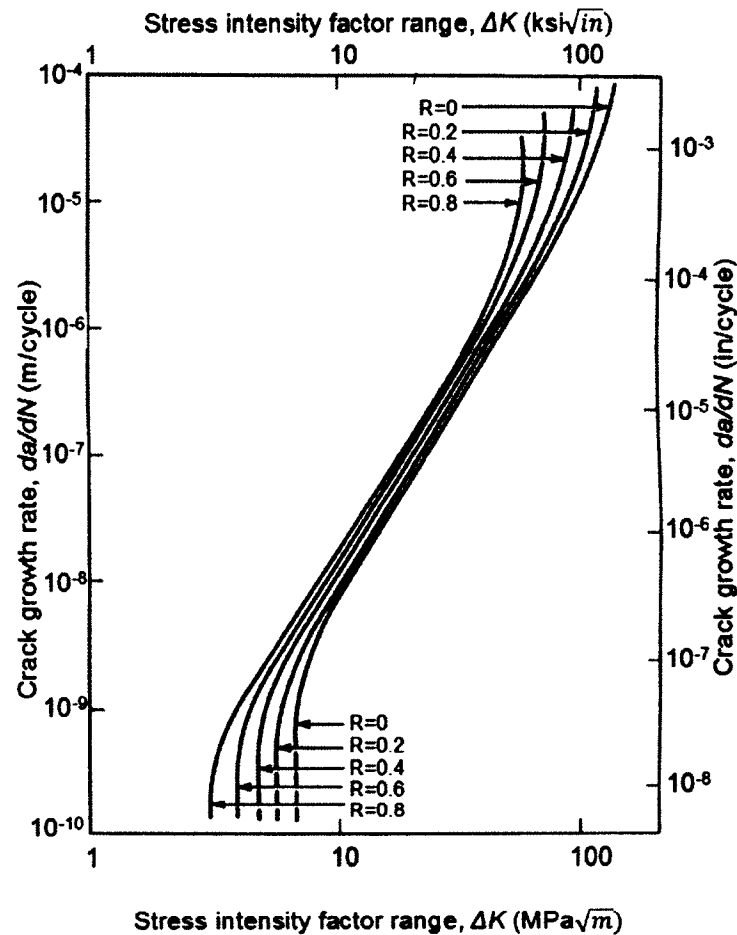


Figure 14. Mean stress influence on fatigue crack growth rates [11]. Reprinted from “Metal Fatigue in Engineering”, 2nd ed., 2000, p. 75, Chapter 4, R I Stephens, with kind permission from “John Wiley and Sons” (License # 3484350018108).

The stress ratio $R = \frac{K_{min}}{K_{max}} = \frac{\sigma_{min}}{\sigma_{max}}$ is used as a principal parameter. A major

proportion of authors have studied the effects of mean stress on crack propagation only for positive stress ratios ($R \geq 0$). From Figure 14 it can be observed that increase of the R ratio results in an increase of the crack propagation rate (da/dN) in all regions of the $da/dN - \Delta K$ curve. It was empirically found that the effect of the R ratio on fatigue crack growth behavior depends on material properties [11].

A commonly used equation that accounts for mean stress effects in regions II and III is the Forman equation [69]:

$$\frac{da}{dN} = \frac{A'(\Delta K)^{n'}}{(1-R)K_c - \Delta K} = \frac{A'(\Delta K)^{n'}}{(1-R)(K_c - K_{max})} \quad (17)$$

where A' and n' are empirical fatigue crack growth rate constants and K_c is the applicable fracture toughness for the material and thickness. The Forman equation is a modified Paris' Law that accounts for mean stress and the unstable rapid crack growth behavior of region III.

The mean stress effects under a positive stress ratio were also described with an empirical relation introduced by Walker (Eq. (18)) [70]:

$$\frac{da}{dN} = \frac{A(\Delta K)^n}{(1-R)^{n(1-\lambda)}} = A^n (\Delta K)^n \quad (18)$$

where A and n are the Paris coefficients and slope for $R = 0$, respectively, and λ is a material constant.

Not much attention was given to the investigation of the effects of negative R ratios. These effects include compressive stress in the cycle. The majority of the tests of cast irons, steels and aluminum alloys under negative R ratios did not demonstrate significant differences when compared to test results obtained under zero stress ratio conditions [81-84].

2.1.9 Cyclic Plastic Zone

Equation (11) describes the size of the monotonic plastic zone developed at the crack tip when the crack is subjected to the maximum load. This concept was initially proposed by Irwin in 1957 [31].

Under cyclic loading, the plastic zone becomes complicated with a second plastic zone that results from the local compression occurring at the time the crack closes during each cycle. The two plastic zones, monotonic (r_y) and cyclic (r'_y), are proportional to

$\left(\frac{K_{max}}{\sigma_y}\right)^2$ and $\left(\frac{\Delta K}{\sigma_y}\right)^2$ respectively. The size of the cyclic plastic zone relative to the

microstructure determines the Stage of crack propagation. The schematic of the plastic zone at the tip of the propagating crack is shown in Figure 15. Davidson and Lankford described the nature of cyclic plastic zones [85-87].

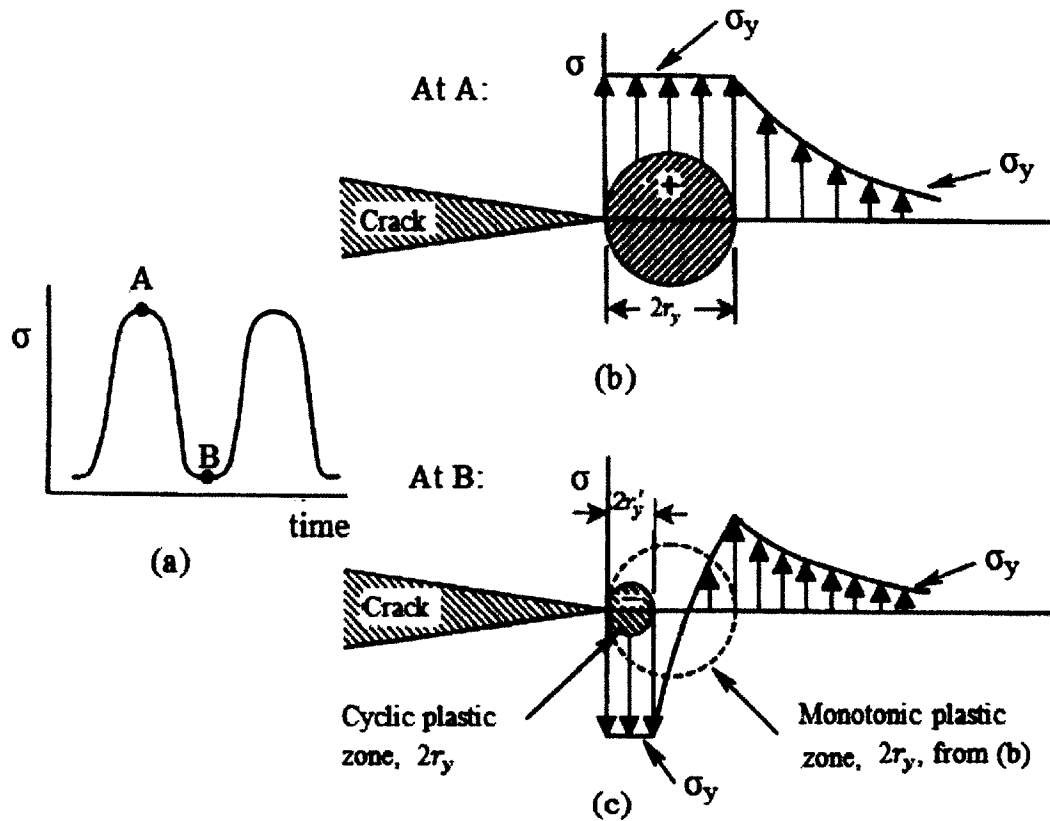


Figure 15. Schematic of the plastic zone at the tip of advancing crack: (a) loading cycle, (b) monotonic plastic zone, (c) cyclic plastic zone [11]. Reprinted from “Metal Fatigue in Engineering”, 2nd ed., 2000, p. 92, Chapter 6, R I Stephens, with kind permission from “John Wiley and Sons” (License # 3484350018108).

Figure 15a presents a typical sinusoidal load cycle with points A and B representing maximum and minimum load respectively. The maximum load produces monotonic plastic zone. The minimum load produces cyclic plastic zone (point B in Figure 15a). The local stress near the crack tip at the minimum load is reduced to a value less than that observed for the monotonic plastic zone size (r'_y). The stresses at minimum load within the cyclic plastic zone are compressive. Their magnitude tends to decrease towards the outside of the zone where the stresses become tensile.

The size of the cyclic plastic zone experiencing yielding under plane stress condition can be determined with Eq. (19) [75]:

$$r'_y = \frac{1}{4\pi} \left(\frac{\Delta K}{\sigma_y} \right)^2 \quad (19)$$

where r'_y is the size of the cyclic plastic zone under plane stress conditions for $R \geq 0$, σ_y is the yielding stress, and ΔK denotes the range of the stress intensity factors ($K_{max} - K_{min}$). Under plain strain conditions, the cyclic plastic zone size can be estimated using Eq. (20):

$$r'_y = \frac{1}{12\pi} \left(\frac{\Delta K}{\sigma_y} \right)^2 \quad (20)$$

Loye and others studied the plastic zone ahead of a fatigue crack in 316 Stainless Steel on a microstructural level using microhardness techniques. They found that the monotonic plastic zone was characterized by an almost uniform microhardness while the cyclic plastic zone demonstrated a parabolic distribution of the microhardness values. They also observed that the R-ratio did not affect the cyclic zone radius [87].

Chikh studied the influence of the size of the cyclic zone on the propagation of the fatigue crack and observed that generally, the plastic zone size increases with the crack advance. The fatigue crack growth rate can be correlated with the energy concentrated in these plastic zones [88].

Excessive plastic deformation and a large plastic zone size (compared to the crack length) violate assumptions of the LEFM. However, practically it was observed that the LEFM provides reasonable approximations for fatigue crack growth (even when applied to materials that exhibit large plasticity) when the size of the cyclic plastic zone is

significantly smaller than the size of the monotonic plastic zone size [11]. According to Irwin in order to ensure plain strain crack propagation the minimum thickness of the cracked component and the crack length should be at least 2.5 times larger than the squared ratio of the critical stress intensity factor and the yield strength of the material $\left(\frac{K_c}{\sigma_y}\right)^2$. The remaining uncracked length should be at least five times that ratio [31].

2.1.10 Crack Closure

The concept of crack closure was first introduced by Elber in 1970 [89,90]. Based on his experimental observations on thin sheets of 2024-T3 aluminum alloy Elber observed that a fatigue crack can be closed even when subjected to tensile load due to the development of compressive residual stresses at the crack tip region. This phenomenon results in a lower crack propagation rate due to reduction of crack growth driving force. Elber's finding was further studied and resulted in numerous publications on the subject of crack closure. Scientific conferences and symposia have been organized to better understand the crack closure phenomenon. This resulted in various proceedings [91,92].

Figure 16 shows various definitions used to characterize the stress intensity factor range during cyclic loading. Two important points are defined on the K - time plot. One point is where the crack opens on the loading portion of the cycle, K_{op} , and another is where the crack closes on the unloading portion of the cycle, K_{cl} .

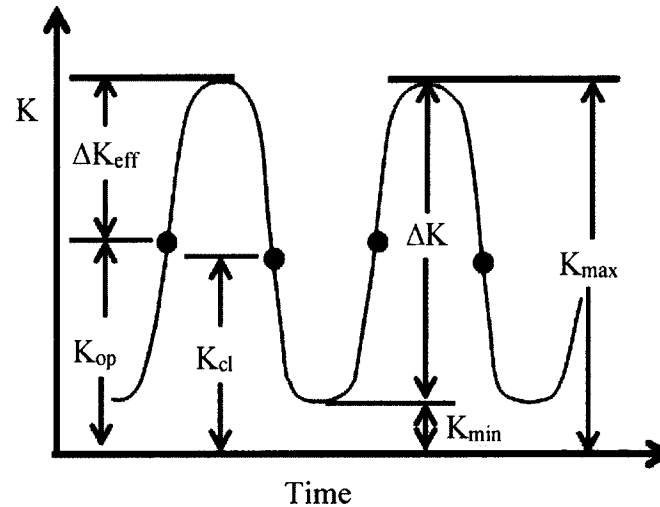


Figure 16. Schematic representation of crack opening and effective stress intensity factors.

As can be seen from Figure 16, the nominal stress intensity factor range, ΔK , defined as $K_{max} - K_{min}$, is greater than the effective crack tip driving force, ΔK_{eff} , defined by Elber as $K_{max} - K_{op}$. Thus the crack propagation driving portion of the loading cycle, ΔK_{eff} , is limited to the crack opening portion of the stress intensity factor range. This means that the portion of the cycle which occurs below K_{op} has little or no influence on fatigue crack growth.

The mechanism of fatigue crack closure observed by Elber by attaching an extensometer close to the tip of a propagating crack is shown in Figure 17 [89]. During crack propagation the plastic zone remains in the region of the actual crack tip. Crack advance occurs within the plastic cyclic zone at the moment when the maximum tensile load is applied. At this moment the elastic energy is released. During unloading cycle material elasticity brings crack faces into contact before the unloading cycle is completed. The remaining portion of the unloading cycle leads to a complete closure of

the crack. (The effect of crack closure becomes unnoticeable in terms of displacement at the crack tip (see Figure 17). The crack closure phenomenon described above was called *plasticity-induced crack closure*.

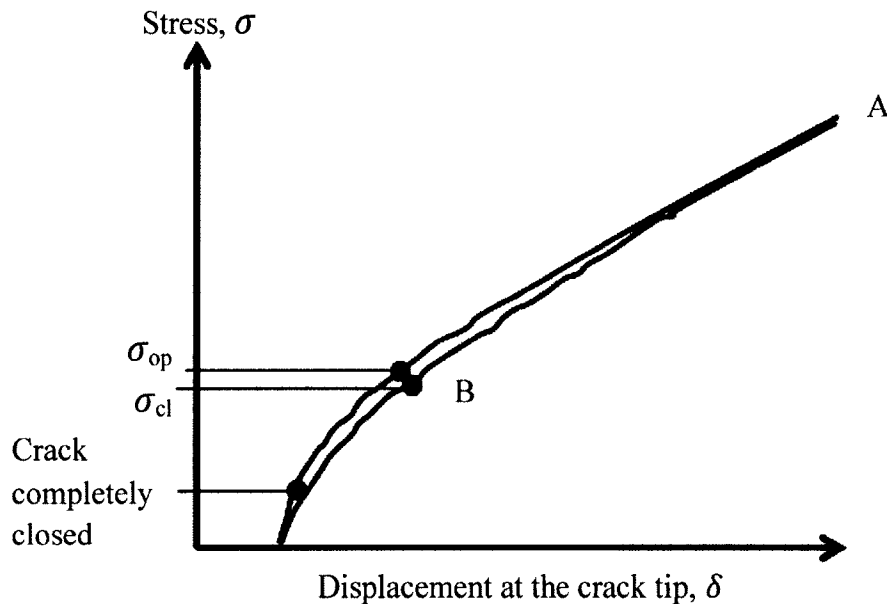


Figure 17. Schematic representation of the mechanism of fatigue-crack closure according to Elber [89]. Reprinted from “Fatigue crack closure under cyclic tension”, 1970, W Elber, with kind permission from Elsevier.

Elber also developed the parameter, termed the closure ratio (U), which defines the magnitude of crack closure. It indicates the portion of the loading cycle during which the crack is open. It is given by Eq. (21):

$$U = \frac{\Delta K_{eff}}{\Delta K} = \frac{\left(1 - \frac{K_{op}}{K_{max}}\right)}{(1-R)} \quad (21)$$

where R is the stress ratio, $R = \frac{K_{min}}{K_{max}} = \frac{\sigma_{min}}{\sigma_{max}}$. At high stress ratio (e.g. for $R > 0.5$) crack growth generally exhibits limited crack closure, while at low stress ratio crack growth tends to experience higher levels of crack closure [11].

Vasudevan and Sadananda stated that plastic deformation along the crack length has almost negligible effect on crack closure. They observed that fatigue crack propagation in a vacuum did not depend on the stress ratio [93-95]. Particularly the whole range of da/dN was nearly independent of the R -ratios when cycling was conducted in a high vacuum. This observation led the authors to the conclusion that plasticity does not induce closure [96,97]. They found that crack closure effects were less important for crack growth when compared with microstructural and environmental effects (described later in the chapter), and did not influence the overall crack growth behavior.

Since Elber's first work in this area, several additional closure mechanisms have been proposed. These mechanisms include transformation-induced crack closure, oxidation-induced crack closure, roughness induced crack closure and others. The concepts of these mechanisms are shown schematically in Figure 18 [98]. The main volume of the publications on crack closure focuses on plasticity-induced, oxide-induced and roughness-induced types of crack closure. These forms of the fatigue closure have been described, categorized and reviewed extensively by a many authors [99-102].

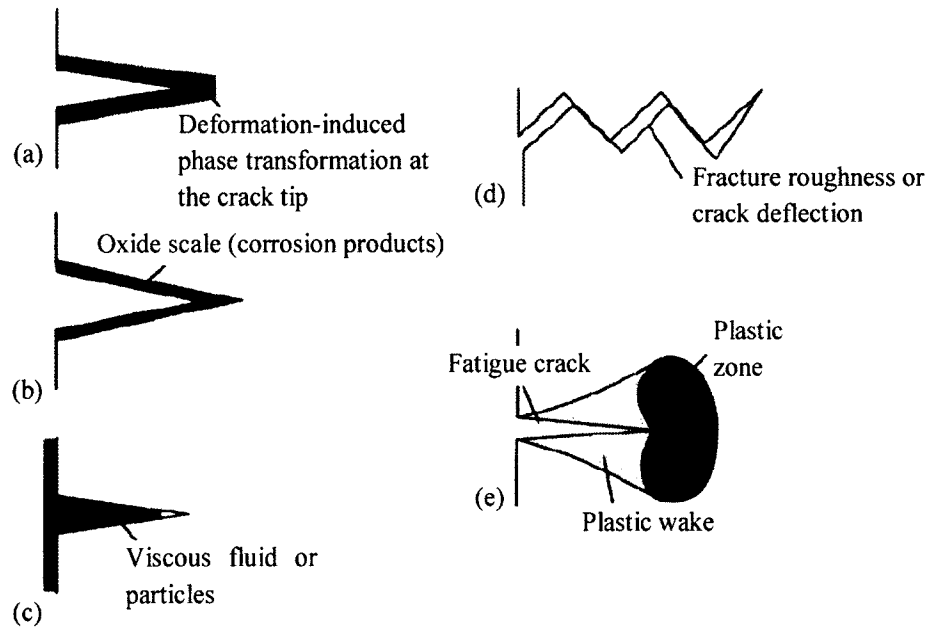


Figure 18. General crack closure mechanisms: (a) transformation induced crack closure; (b) oxidation-induced crack closure; (c) fluid-induced crack closure; (d) roughness- or geometry-induced crack closure; and (e) plasticity-induced crack closure [98]. Reprinted from “Fatigue Crack Propagation in Metals and Alloys: Microstructural Aspects and Modelling Concepts”, 2007, U Krupp, with kind permission from John Wiley & Sons.

Crack closure was demonstrated by some authors to be one of the main causes of crack growth retardation [101]. The crack closure mechanisms can be separated by two types: those that operate in front of the crack tip and those that operate behind the crack tip. The main mechanisms of the first type are crack tip blunting, crack branching, crack tip strain hardening and crack deflection. The mechanisms that operate behind the crack tip include plasticity-induced crack closure and roughness-induced crack closure [102]. The crack closure phenomenon is important and beneficial from a practical standpoint as it was shown to reduce propagation rates of fatigue cracks.

2.1.11 Corrosion Fatigue

Corrosion fatigue is a process of mutual interaction of corrosion and fatigue processes. This phenomenon is usually observed when mechanical structures are subjected to cyclic loads in corrosive environments (gaseous or aqueous). The fatigue life of metals usually reduces in the presence of aggressive environments and failures can occur at lower loads as compared to those applied in mild environments or in vacuum. The degree of fatigue life reduction in a corrosive environment is a function of the environment, the material, and the stress level. It takes time for corrosion to progress. This is why at short fatigue lives the reduction may be small or negligible. However at low cycling rates and at long fatigue lives the fatigue strengths of metals can be significantly reduced when cycled in corrosive environment. Combined interaction exists between the applied stress and the corrosive environment because of the continuous destruction of protective oxide films during cycling. Usually corrosion fatigue is associated with very little material loss and is often localized, involving surface pitting and cracks nucleating from pits. Figure 19 demonstrates the effect of a corrosive environment (3 wt% NaCl water solution) on the crack growth rate of 4340 steel [103].

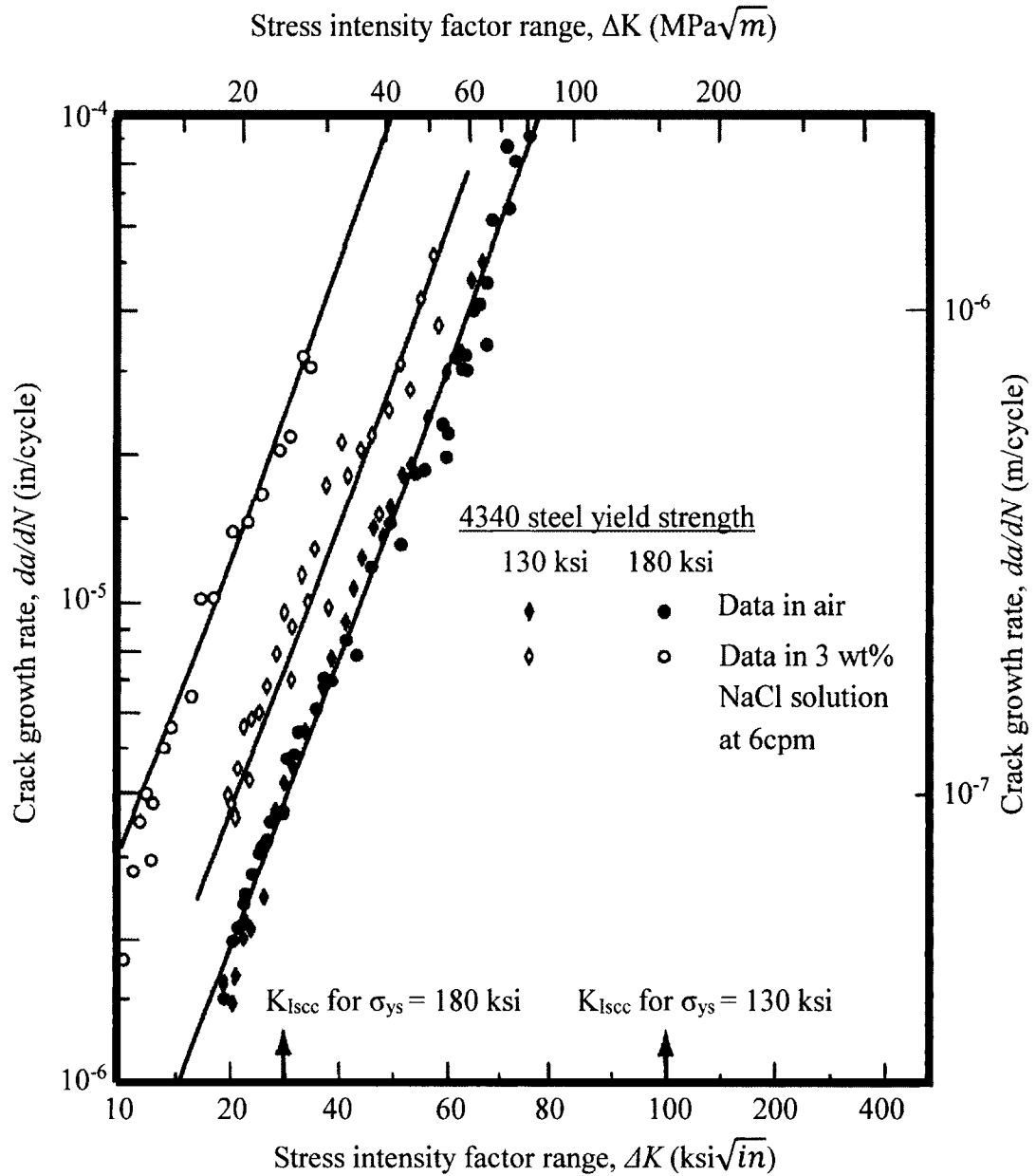


Figure 19. Corrosion fatigue crack growth rates for 4340 Steel in 3 wt% NaCl water solution [103]. Reprinted from “Fatigue and Corrosion-Fatigue Crack Growth of 4340 Steel at Various Yield Strengths”, 1973, E J Imhof, with kind permission from ASTM International.

Novak studied corrosion-fatigue crack initiation behavior of four structural steels at low cycling frequency and stress rate [104]. He showed that fatigue loading in a corrosive environment (3.5 wt% NaCl solution) can result in a degradation of cyclic load-

carrying capacity of ASTM A36 steel by 54 percent. At very high crack growth rates less time is available for the interaction between corrosion and cyclic stresses. In those cases the fatigue rate differences between corrosive and non-corrosive environments is usually small. Better corrosion fatigue resistance exists in those environment/material systems where corrosion resistance itself is better.

2.1.12 Fatigue Crack Repair Techniques

Several methods of rehabilitation of steel structures containing fatigue cracks were developed over the years. Initial methods relied on removing material containing a fatigue crack from a damaged part. A portion of the material containing a fatigue crack was simply ground away if the crack was shallow [105]. Often this method required further welding of the material to restore strength loss associated with grinding. However, welding is also associated with the reduction of fatigue life due to the development of residual stresses, stress corrosion cracking and hydrogen embrittlement [106]. High variations in success and the difficulty of implementing these methods led to development of more practical methods.

Stop hole drilling has been extensively utilized in engineering applications [107-111]. This method was based on reducing the stress concentration factor by drilling a hole at the crack tip. The fatigue crack had to re-initiate from a hole and thus the fatigue growth was retarded. This method suffers from the difficulty of locating the fatigue crack tip and thus the results were often inconsistent and unpredictable.

Compressing the material at the fatigue crack tip with steel rollers or balls was studied [110, 112-117]. Compression causes plastic deformation and material hardening at the crack tip region and thus reduces the fatigue crack growth rate.

Thin-walled components containing a fatigue crack can be treated with adhesive patching with composite materials. This method has been used in the aircraft industry [118-120]. The efficiency of the method was found to be low when applied to thick components or those under large loading.

Novotny during his study of methods of fatigue life extension of pressure vessels found that a single tensile overload could slow down crack propagation [119]. Many authors have concluded that crack closure caused by the overload was the main mechanism of the crack growth retardation [122-124]. This method did not find broad engineering application due to the significant risk of structural failure while overloading.

The mechanism inducing crack retardation due to closure has been used in other fatigue crack repair methods, for example, crack infiltration with foreign materials. Sharp and his colleagues have described a method of fatigue crack treatment in aluminum by vacuum-infiltration of polymeric materials into the crack tip [125]. Song has achieved fatigue crack life extension of up to 300,000 cycles by employing pressurized nitrogen for introducing closure materials into the crack and using alumina and silicon carbide reinforced epoxy resin for crack infiltration in 5083-O aluminum alloy and AISI 4130 stainless steel specimens [126]. Shin and Cai in 2008 reported growth retardation of surface fatigue cracks by infiltration of polymeric resin [127]. Crack infiltration with polymers (usually epoxy resin) has been tested by some other authors with varying levels of success [128-130]. Numerical models for determining the result of crack treatment by infiltration techniques have also been proposed [128,130]. Generally low reproducibility of the experimental results was observed. This could be explained by the high viscosity of epoxy that often prevented penetration to the crack tip. Increasing the temperature of

the epoxy resin could reduce its viscosity, but a temperature over 150°C could affect the stability of the epoxy resin for long-term use [131]. Low epoxy strength compared to the metal could be another cause of low data reproducibility when higher stress levels were applied.

The latest methods of fatigue crack treatment have involved introduction of carbon nanotubes into the fatigue crack tip [132-135]. Those studies demonstrated fatigue life increase due to a fatigue crack bridging (wedging) mechanism. In another study, Syed and Jiang reported fatigue crack life extension of about 40% when multi-walled carbon nanotubes were introduced into fatigue cracks of compact tension specimens machined from 304 stainless steel. Carbon nanotubes still remain a very expensive material, and their application for fatigue crack treatment is currently economically unfeasible.

In this study electrochemical treatment of fatigue cracks was attempted. Nickel was introduced into fatigue cracks via electroplating. Electrochemical treatment has advantages in terms of low viscosity of the plating solution, high temperature and corrosion resistance, and high strength of the deposit. This method is less expensive as compared to an introduction of carbon nanotubes and can be applied by several well-known nickel plating techniques.

2.2 Electrochemistry

2.2.1 Definition and Fundamentals of Electrochemistry

Electrochemistry is the study of mutual electrical and chemical reactions. In these reactions charged particles (ions or electrons) transfer through the boundary between two phases of matter: solid (usually metallic) and liquid. These particles migrate from one electrode to another through a conductive solution (electrolyte) [136]. The necessity to study chemical and electrical phenomena in their unity was first expressed by Russian scientist Michail Lomonosov more than 250 years ago. The first experimental work in electrochemistry was done by Italian physician and physicist Luigi Galvani in 1791 [137]. The first battery whose principle was based on electrochemistry was invented by Alessandro Volta in 1800. His invention is currently known as a voltaic pile. The battery consisted of interleaved copper and zinc disks separated by paper sheets steeped in acid solution. Volta's discovery of a sustainable source of electrical current has accelerated the development of electrochemistry. In 1835 Michael Faraday defined the main concepts of electrochemistry: anode, cathode, electrode, electrolyte, and ion [138]. Benjamin Franklin defined the positive and negative mathematical conventions for electrical charge [139]. Gibbs and Helmholtz significantly contributed to the understanding of the energy of the galvanic cell [140]. A Large contribution to the formation of solution theory was made by Hittorf, Kohlrausch, Arrhenius, Mendeleev [141-143]. They determined the electric charge of ions defined the electrical resistance of the solution, described the nature of ions, and the thermodynamics of the solvation process. In 1923 Debye-Hückel proposed the theory of strong electrolytes [144].

During an electrochemical reaction oxidation and reduction processes are taking place. Oxidation refers to the process in which chemical species lose one or more electrons. These species are called reducing agents. The gain of electrons is called reduction and the species that receive them are termed the oxidizing agents. Reduction-oxidation (redox) is a process that involves both reduction and oxidation [137]. This process can occur when external electric energy is applied to a system or an internal chemical energy is released.

2.2.2 Electrochemical Cells

An electrochemical cell is a device that can generate electricity from chemical reactions or drive chemical reactions through the application of electricity. Two types of electrochemical cells are distinguished: galvanic and electrolytic. Galvanic cells are those whose reactions are spontaneous when the electrodes are connected via a conductor. An electrolytic cell requires a potential in excess of its open-circuit potential (OCP) to be provided in order to drive an electrochemical process [137]. Figure 20 schematically represents an electrolytic electrochemical cell.

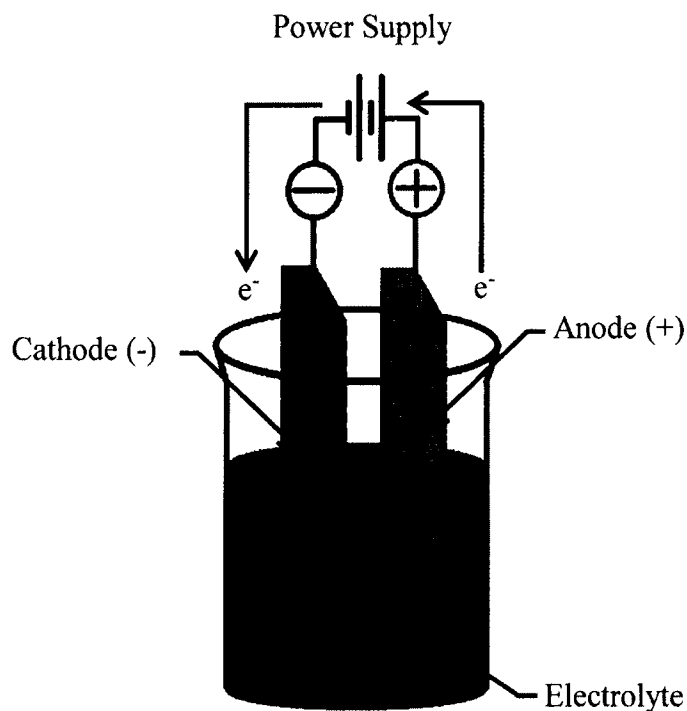


Figure 20. Schematic of electrolytic electrochemical cell.

Electrochemical cells require two conductive electrodes defined as the cathode and the anode. The reduction process takes place at the cathode and the oxidation process takes place at the anode. Electrodes are usually made of materials possessing relatively high conductivity, such as metals, semiconductors and even conductive polymers. The electrodes are placed in electrolyte which contains ions that can carry the current and move freely. In this study a titanium electrode was used as an anode, ASTM A36 steel was the cathode, and a Watts nickel plating bath was used as an electrolyte. Driven by the electrical current, nickel ions migrated from the electrolyte (nickel plating solution) to the surface of the cathode (ASTM A36 steel).

2.2.3 Electrodeposition of Metals, Electroplating

Electrodeposition refers to the process of deposition of a thin metallic layer onto a substrate material occurring through the electrochemical reduction of metal ions from an electrolyte. This technology is also known as electroplating.

The deposition a substrate material is immersed into an electrolyte containing a counter electrode. These two electrodes are then connected to an external power supply to establish a direct current circuit (see Figure 20). The substrate (the object to be plated) is connected to the negative terminal of the power supply. Plating metal (anode) is dissolved into the electrolyte to form metal ions. The flow of direct current causes one of the electrodes (the anode) to dissolve. The ions travel through the solution depositing onto the cathode's surface. Electroplating of metals is utilized in a many industries such as metallurgy, microelectronics, nanotechnology and others. The most often plated metals are nickel, copper, chromium, and zinc.

Electroplated coatings of nickel are known for providing corrosion and wear resistance [144]. Nickel plating was first patented by Bottger in Germany in 1843. Bottger used nickel ammonium sulfate plating bath. He was later acknowledged as the originator of nickel plating [145]. Different formulations of nickel ammonium chloride plating solution were patented in the U.S. starting in 1869 [146-149]. In 1916 Watts developed a rapid nickel plating solution which remains the most popular to date [150]. The plating operation in Watts' solution was relatively inexpensive and simple. The Watts' nickel plating bath's composition, operating conditions and mechanical properties are presented in Table 4.

Table 4. Composition, operating conditions and mechanical properties of Watts nickel plating bath [150]

Composition		
Chemical Name	Chemical Formula	Amount
Nickel sulphate	$\text{NiSO}_4 \cdot 6\text{H}_2\text{O}$	32-40 oz/gal (240-300 g/l)
Nickel chloride	$\text{NiCl}_2 \cdot 6\text{H}_2\text{O}$	4-12 oz/gal (30-90 g/l)
Boric acid	H_3BO_3	4-6 oz/gal (30-45 g/l)
Operating Conditions		
Temperature		105-150°F (40-65°C)
Cathode Current Density		20-100 A/ft ² (2-10 A/dm ²)
pH		3.0-4.5
Mechanical Properties		
Tensile Strength		50-70 ksi (345-485 MPa)
Elongation		10-30%
Hardness		130-200 HV
Internal stress		18-27 ksi (125-185 MPa)

Each of the constituents of the Watts' solution affects the properties of the electrodeposited nickel. Nickel sulfate improves metal distribution and solution conductivity. It also defines the maximum cathode current density at which a good quality nickel deposit will be achieved. Nickel chloride is beneficial as it increases the dissolution rate of the anode. It also increases the conductivity and throwing power which in turn improves the uniformity of plating. The throwing power is a characteristic of an electroplating solution defining its ability to leave uniform thickness deposits on non-uniform (irregular) surfaces. It also refers to the distance away from the anode at which a

quality deposition can be applied. Chlorides increase the internal stress of the deposits and typically reduce the grain size. Boric acid is usually added to achieve better appearance and higher brightness of the deposits. The operating conditions, such as pH, temperature and current density also affect the material properties of the deposits [151].

The weight of the deposited nickel can be estimated using the Faraday's Law of Electrolysis which is shown in Eq. (22):

$$W = \frac{ItA}{nF} \quad (22)$$

where W is the weight of the plated metal (grams), I is the current (Ampere), t is time (sec), A is the atomic weight of the metal (gram/mole), n is the valence of the dissolved metal in solution, F is Faraday's constant ($F = 96,485.309$ coulombs/equivalent). The thickness of the deposited layer can be obtained by dividing its weight by the surface area and material density. The surface roughness of plated nickel (R_a) can be estimated using Eq. (23) [152]:

$$R_a = \frac{1}{n} \sum_{i=1}^n |y_i| \quad (23)$$

where n represents points along the trace of the profile, y_i is a vertical distance from the mean line to the i^{th} data point.

For some applications on steel structures the surface roughness is of high importance. For example this is a concern for the function of sliding components or for the minimization of hydrodynamic drag. Surface roughness is of interest as it affects fatigue life of smooth components [153-157].

Electrodeposited nickel is characterized by high hardness (130-500 HV) [158]. Nickel depositions are often twice (or more) as hard as bulk nickel due to the microstructure created by the deposition process [159]. Nickel coatings provide great wear resistance as well as corrosion resistance.

2.2.4 Corrosion of Metals

Corrosion is one of the main causes of infrastructure damage in the United States. The study of the US Federal Highway Administration revealed that in 1998 the total annual cost of losses associated with corrosion only in the U.S. was around \$276 billion [160]. This amount constitutes to approximately 3.2% of the US gross domestic product. Corrosion of pipelines constitutes \$7 billion of this total. Oil and gas pipelines often experience this type of degradation [160-163]. Corrosion was found to be responsible for 18% of the significant incidents in oilfield occurring in the decades (1988 – 2008).

Corrosion is a process of material degradation due to a reaction with an environment. These reactions can be chemical, electrochemical and sometimes mechanical in nature. Metals usually react with an environment in an electrochemical manner [164].

As a result of corrosion the properties of metals can change and their functional characteristics are degraded. Corrosion can partially or completely destroy metals. There are several manifestations of corrosion. They are differentiated by the form of the changes made to the metal surface. Figure 21 shows several of the main types of corrosion damage. Each type is discussed in the following paragraphs.

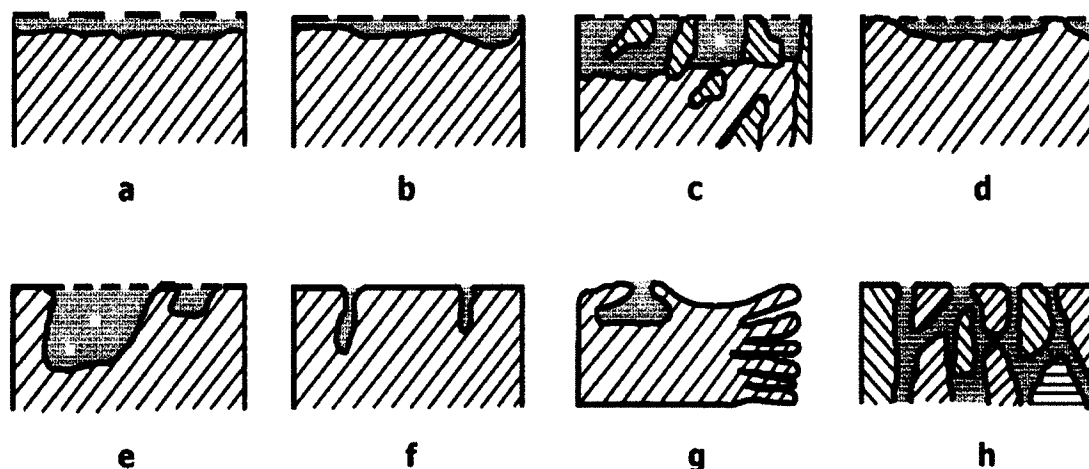


Figure 21. Types of corrosion: (a) uniform; (b) non-uniform; (c) selective leaching; (d) stain corrosion; (e) crevice corrosion; (f) pitting corrosion; (g) undersurface corrosion; (h) intergranular corrosion [161]. Reprinted from “Corrosion and Corrosion Protection”, 2002, I Semenova, with kind permission from Dr. Semenova.

Uniform (general) corrosion (Figure 21, a) progresses with the same speed over the entire surface of a substrate [161]. This is in large contrast to non-uniform corrosion, (Figure 21, b) where the speed of the process varies over the location. Examples of general corrosion can be observed everywhere, as metals corrode uniformly in atmospheres, soils and water. The appearance of general corrosion is usually called “*rust*”. During selective leaching (Figure 21, c) one alloy element of a material component is being dissolved. Alloys containing dissimilar metals are often susceptible to this type of corrosion. The interaction between more and less noble metals within the alloy in corrosive environments causes the less noble metal to dissolve via galvanic corrosion acting on a microscopic level. This type of corrosion is usually observed in alloys containing metals with significantly different corrosion potentials (located far from each other in the galvanic series). The elements that often experience selective leaching

are zinc, aluminum, iron, cobalt, and chromium. Local corrosion (Figure 21, d, e, and f) covers only some areas of the metal surface.

Local corrosion can be found in the form of stains, crevices and pits [161,165]. Crevice corrosion (Figure 21, e) usually occurs in restricted small spaces with limited access to a corrosive liquid (electrolyte). Pitting corrosion (Figure 21, f) is a form of a very localized corrosion. Pitting corrosion is typically differentiated by small holes and cavities. The cause of pitting corrosion is the localized disruption of the protective passive film within a small region of the material surface. This region becomes anodic while the rest surface area becomes cathodic. This leads to a localized galvanic corrosion. After a pit has been established, the mechanism of pitting corrosion is then similar to crevice corrosion. In both cases a key feature is that the oxygen content within the pit or crevice is much lower than on the outer surface of the metal. Both processes tend to be autocatalytic as the pH within the pit or crevice starts to drop and the pH outside of this location starts to increase. Both of these trends tend to accelerate the corrosion rate within the pit or crevice. Undersurface corrosion (Figure 21, g) initiates on the surface but mainly propagates inside the thickness of a metal. The products of the corrosion become accumulated in the formed cavities inside the metal. This type of corrosion causes distention and exfoliation of the metallic products.

Intergranular corrosion cracking (Figure 21, h) is characterized by the destruction of the metal on the grain boundaries [166]. This is caused by the formation of corrosion products in between the grains. Intergranular corrosion is often observed in chromium, nickel and aluminum alloys.

The cause of electrochemical corrosion is the thermodynamic instability of metals in electrolytic environments [166]. An ability of metals to withstand the impact of the environment is called the corrosion resistance or chemical resistance. Some metals are naturally more resistant to corrosion than others. The Galvanic series shown in Figure 22 presents the list of metals and their corrosion potentials in seawater from the highest (noble, cathodic metals) to the lowest (the most corrosion susceptible, anodic metals).

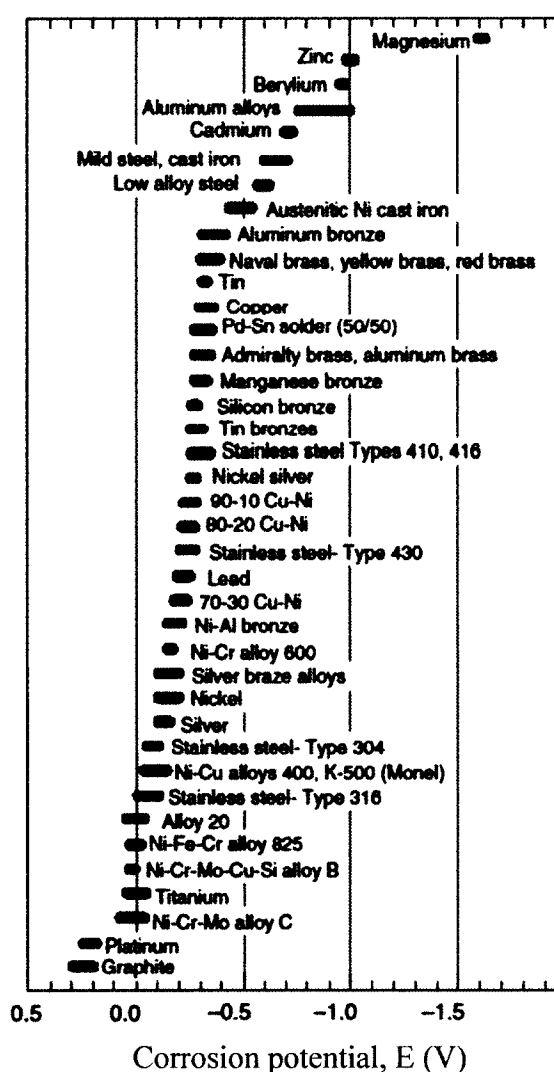
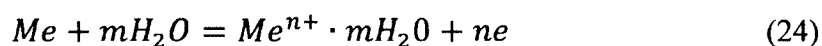


Figure 22. The galvanic series in seawater [166]. Reprinted from “Thermodynamics of Corrosion: Electrochemical Cells and Galvanic Corrosion”, 2010, p. 77, Chapter 5, E McCafferty, with kind permission from Springer Science and Business Media (License #3417950650014).

It is important to understand electrochemical thermodynamics and electrochemical kinetics in order to explain corrosion reactions. If metals are placed into an electro-conductive environment, such as an acid, alkali or salt solution the main condition for the initiation of an electrochemical type of corrosion is satisfied [167]. When a metal is introduced into an electrolytic solution interaction with charged particles of the solution takes place and ions of the metal dissolve into the surrounding solution. During electrochemical corrosion two conjugated processes are observed. The first process is the movement of atoms from a metal to a solution where they transform into solvated (in aqueous solutions – hydrated) ions. A chemical (oxidizing or anodic process) is expressed by Eq. (24):



The second process is the transition of those ions from the solution onto the surface of metal in the form of neutral atoms (a reduction or cathodic process).

The rate of corrosion is controlled by the electrode kinetics of reduction and oxidation [167]. If all parameters of electrochemical reactions are known the rate of corrosion can be determined using the Faraday's law. Faraday's Law describes a relationship between the metal corrosion rate at any potential, V_M , and the current density of metal corrosion $i_{a,M}$:

$$V_M = \frac{i_{a,M}}{nF} \quad (25)$$

where n is the number of electrons involved in the dissolving reaction, and F is the Faraday constant, $F = 96.485 \text{ C/mol}$. When polarization is not applied externally a metal immersed into a corrosive environment immediately obtains a certain potential,

termed the corrosion potential, E_{corr} [166]. The current density at the corrosion potential is defined as the corrosion current density, i_{corr} . At this point, Eq. (25) then can be written as Eq. (26):

$$V_{corr} = \frac{i_{corr}}{nF} \quad (26)$$

The net flow becomes equal to zero at the point when electrons available from within a corroding surface and the positive ions that are approaching it from the electrolyte are in equilibrium [161]. The electric potential difference at this point is called the equilibrium potential. The value of the equilibrium potential depends on temperature and the activity of reacting substances and can be estimated using the Nernst equation (Eq. (27)):

$$E_p = E_0 + \frac{RT}{nF} \ln \frac{a_{Me^{n+}}}{a_{Me}} \quad (27)$$

where E_0 is the standard metal potential; R is the universal gas constant; T is the absolute temperature; a is the chemical activity; n is the number of electrons participating in a reaction. In the case when the activity of the metal ions is equal to one the second member of Eq. (27) becomes equal to zero. At this point the electrode potential is equal to the standard potential. The values of the standard electrode potentials of some metals are given in Table 5.

Table 5. The values of standard electrode potentials of some metals [161]

Chemical Reaction	Potential, (V)	Chemical Reaction	Potential, (V)
$K^+ + e \rightleftharpoons K$	-2.925	$Pb^{2+} + 2e \rightleftharpoons Pb$	-0.126
$Ba^{2+} + 2e \rightleftharpoons Ba$	-2.9	$Fe^{3+} + 3e \rightleftharpoons Fe$	-0.037
$Mg^{2+} + 2e \rightleftharpoons Mg$	-2.37	$H^+ + e \rightleftharpoons 1/2H_2$	0
$Al^{3+} + 3e \rightleftharpoons Al$	-1.66	$Sn^{4+} + 4e \rightleftharpoons Sn$	+0.007
$Ti^{2+} + 2e \rightleftharpoons Ti$	-1.63	$Bi^{3+} + 3e \rightleftharpoons Bi$	+0.215
$Ti^{3+} + 3e \rightleftharpoons Ti$	-1.21	$Sb^{3+} + 3e \rightleftharpoons Sb$	+0.24
$Mn^{2+} + 2e \rightleftharpoons Mn$	-1.18	$Cu^{2+} + 2e \rightleftharpoons Cu$	+0.337
$Cr^{2+} + 2e \rightleftharpoons Cr$	-0.913	$Co^{3+} + 3e \rightleftharpoons Co$	+0.418
$Zn^{2+} + 2e \rightleftharpoons Zn$	-0.762	$Ag^+ + e \rightleftharpoons Ag$	+0.799
$Fe^{2+} + 2e \rightleftharpoons Fe$	-0.44	$Hg^{2+} + 2e \rightleftharpoons Hg$	+0.854
$Mn^{3+} + 3e \rightleftharpoons Mn$	-0.283	$Ir^{3+} + 3e \rightleftharpoons Ir$	+1.15
$Ni^{2+} + 2e \rightleftharpoons Ni$	-0.25	$Au^+ + e \rightleftharpoons Au$	+1.69

The measurement of the absolute electrode potential is currently technically impossible [166]. It may only be measured with a respect to a reference electrode. Standard hydrogen electrode's potential is used as a reference potential. For practical laboratory experiments copper-copper-sulfate or calomel reference electrodes are often utilized.

A potentiostat is a device used for electrochemical corrosion potential and corrosion current measurements [165]. It can be used to control a three electrode cell (which utilizes a working, a counter and a reference electrode). For some measurements the potential of a working electrode is kept at a constant level relative to a reference

electrode while changing the current at the counter electrode. The values of the current flow between a working and a counter electrode are then recorded.

A type of corrosion that is characterized by corrosion of one metal with respect to another caused by the difference of corrosion potentials is called *galvanic corrosion* [165]. During this process two dissimilar metals are in electrical contact and subjected to a corrosive environment. The less noble metal (anode) corrodes faster than it would independently, while the other corrodes slower (cathode). The corrosion potential is a measure of the relative nobility of metals [161]. The values of the nobility of some metals immersed into seawater can be found and listed in a galvanic series this particular environment (see Figure 22). A higher corrosion potential indicates higher nobility for that given metal.

Metallic structures operating under the simultaneous effects of an aggressive environment and a mechanical stress are subjected to a greater rate of deterioration [162,163,166,168-170]. Two types of mechanical stresses are recognized - internal and external. Internal stresses appear during thermal and mechanical processing, such as welding. External stresses are applied from without. They can be static or alternating (cycling). Three stages of corrosion processes acting under mechanical loadings are differentiated: incubation the stage, the corrosion origin development stage and the rapid failure stage. The structure of the surface of a metal experiences changes under mechanical stresses. This can lead to a change of its corrosion potential at some locations, to destruction of the protection film, and, as a result, to an increased corrosion rate. The following types of corrosion damage under mechanical loading are differentiated: stress

corrosion cracking (SCC), corrosion fatigue, hydrogen induced cracking, and erosion corrosion or fretting corrosion.

Stress corrosion cracking occurs under a simultaneous effect of a corrosive environment and a constant tensile stress [168,169]. At the initial stage cracks appear as a result of chemisorption of active ions from the corrosive environment. The origination of cracks could be associated with the appearance of microscopic tunnels (around 0.05 μm) and pits at the areas of defects. Such areas may be located, for example, at the grain boundaries, impurities or at the accumulation points of dislocations. Crack propagation and metal failure happens under the prevalent effect of a mechanical factor. Corrosion cracking is characterized by the almost absence of plastic deformation. The electrochemical potential has a critical effect on stress corrosion cracking. This type of corrosion can be often be observed in components that have residual stresses after thermal or mechanical processing such as assembling or welding, or after operation under high pressure or temperature. Stress corrosion cracking is estimated to be responsible for 20%-40% of all corrosive damage in the oil and gas field [161].

Corrosion fatigue is a process of material destruction due to the simultaneous effect of cyclic loading and a corrosive environment [161,165,166,168-170]. This synergistic process is typically associated with a larger level of material degradation as compared to corrosion or fatigue acting alone. Despite the increasing number of studies denoted to corrosion fatigue the basic understanding of this complex problem is still limited [163,169]. Recent studies have demonstrated a general lack of reliable corrosion fatigue results, and low availability of corrosion-fatigue crack initiation behavior. Corrosion fatigue destruction is often associated with the development of transgranular

and intergranular cracks. The cracks usually propagate only at the moment of tensile stress application. The susceptibility of the metal to corrosion fatigue is characterized by its fatigue endurance limit (the maximum cyclic stress that can be applied without causing a failure within 10^7 or more cycles). The simultaneous effect of the cyclic loading and a corrosive environment reduces the number of cycles before failure. The effect of the corrosive environment can increase the crack propagation rate dramatically. For example, Stonesifer and Krafft observed crack growth rate acceleration of about a factor of three in ASTM A36 steel fatigue cycled in seawater [170]. Novak studied fatigue crack initiation of four steels, including ASTM A36 in air and seawater environments under slow frequency and long fatigue life conditions [88]. He observed a 54% reduction of cyclic load-carrying capacity of the ASTM A36 steel in seawater.

CHAPTER 3

METHODOLOGY AND PROCEDURES

The procedures of this study can be separated into three groups: experimental, analytical and simulation procedures. The experimental procedures consisted of fatigue crack initiation, electrochemical crack treatment and post-treatment crack growth. The analytical procedures consisted of microscopy, spectroscopic analysis, corrosion susceptibility determination and analytical modeling. Finite element modeling and simulation was accomplished in ANSYS.

3.1 Fatigue Crack Initiation and Growth

Fatigue cracks were initiated and grown in notched compact tension (CT) specimens. The specimens were designed and machined according to ASTM E399 “Standard Test Method for Plane-Strain Fracture Toughness of Metallic Materials” [47]. Geometry and dimensions of the tested specimens are presented in Figure 23.

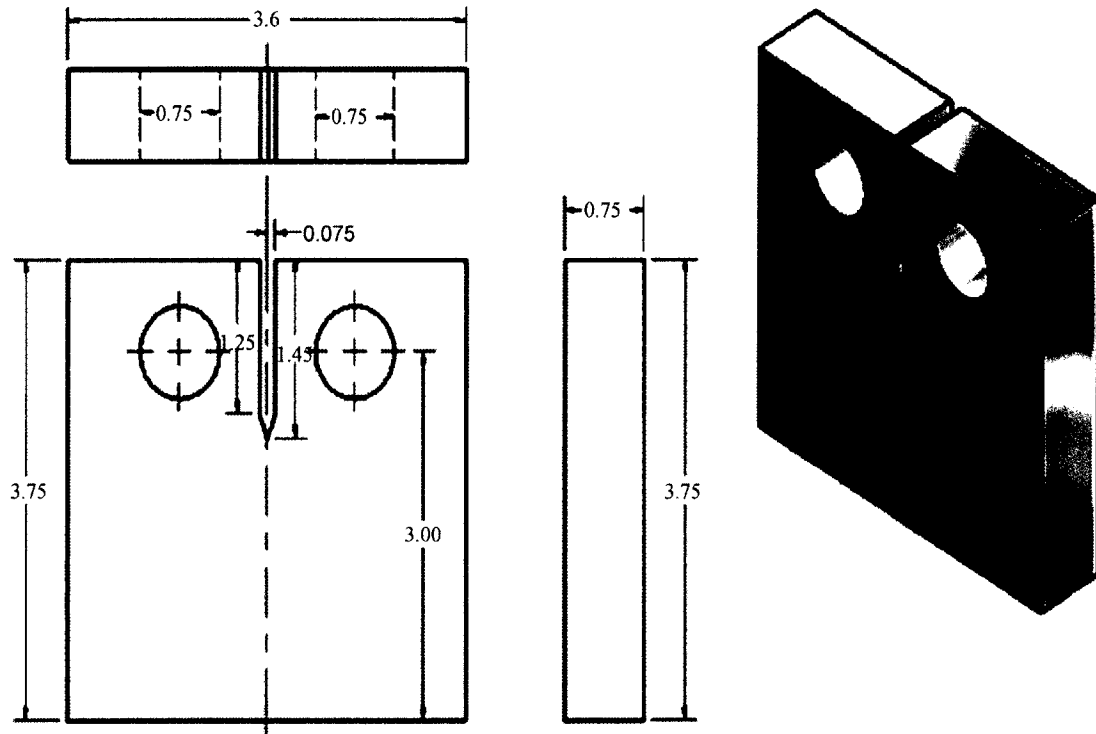


Figure 23. ASTM E399 compact tension specimen (dimensions are in inches).

The specimens were machined from ASTM A36 Mild (low-carbon) steel. A36 steel is a standard steel alloy which is a common type of a structural steel used in the United States. The steel was purchased as hot-rolled flat bars from onlinemetals.com. The chemistry and mechanical properties of the steel provided by the supplier are presented in Table 6 [171].

Table 6. Mechanical properties and chemistry of ASTM A36 Mild (low-carbon) steel

Categories	Properties	Values
Mechanical	Density, ρ (lb/in ³)	0.28
	Young's modulus, E (psi)	29x10 ⁶
	Poisson's ratio, ν	0.26
	Ultimate Tensile Strength, σ_u (psi)	58,000 – 79,800
	Yield Strength, σ_y (psi)	36,300
	Elongation, δ (%)	20.0%
	Shear modulus, G (psi)	11.5x10 ⁶
Chemical	Iron (Fe)	99%
	Carbon (C)	0.26%
	Manganese (Mn)	0.75%
	Copper (Cu)	0.2%
	Phosphorus (P)	0.04% max
	Sulfur (S)	0.05% max

Specimens were machined at Louisiana Tech University's machine shop.

Equipment used for fabrication included: a power band saw, a drilling machine, and a planer.

Specimen fabrication steps were conducted as follows: the cutting of the specimen outer dimensions from the steel flat bar was done using the band saw. The specimen loading apertures were made with a drill press. A straight-through slot terminating in a fatigue crack starter notch with 60° angle was accomplished using a V-notch cutter installed on the “#2” planer type milling machine (Cincinnati Milling

Machine Company, OH, USA). The dimensional tolerances and surface finishes proposed by ASTM E399 Standard were followed throughout the fabrication process [47].

Specimens were loaded in an MTS servo-hydraulic testing machine. Fixtures suitable for loading and holding the specimen (see Figure 24) were designed and machined as shown in ASTM E399 Standard (see Appendix A4) [47]. Both ends of the specimen were held in clevises and loaded with pins. The cylindrical pins allowed rotation of the specimen during cycling. As was suggested by the Standard rolling contact between the pins and the clevises was ensured by machining small flat areas on the loading surfaces as shown in Figure 25. The testing machine was controlled using TestStar™ IIs software version 4.0C 1994 (MTS Systems Corporation, MN, USA). The fatigue cracking setup is shown in Figure 26.

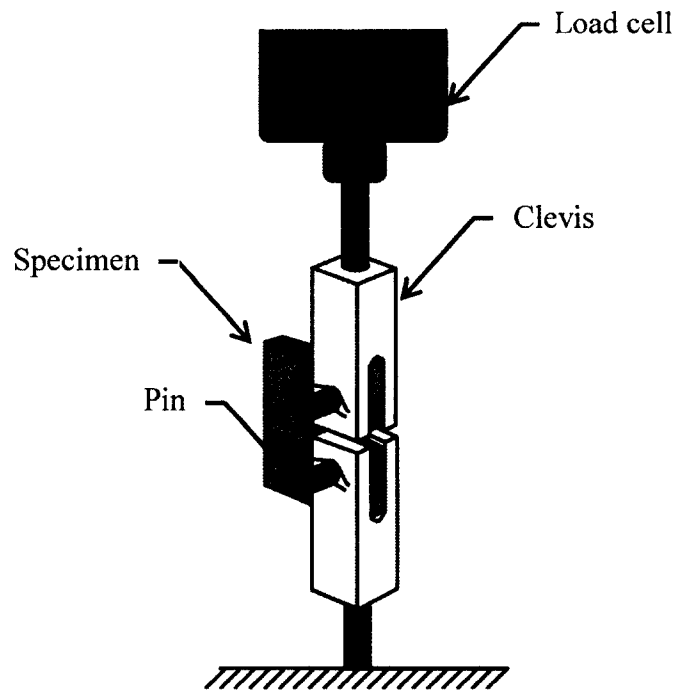


Figure 24. CT specimen loaded into clevis.

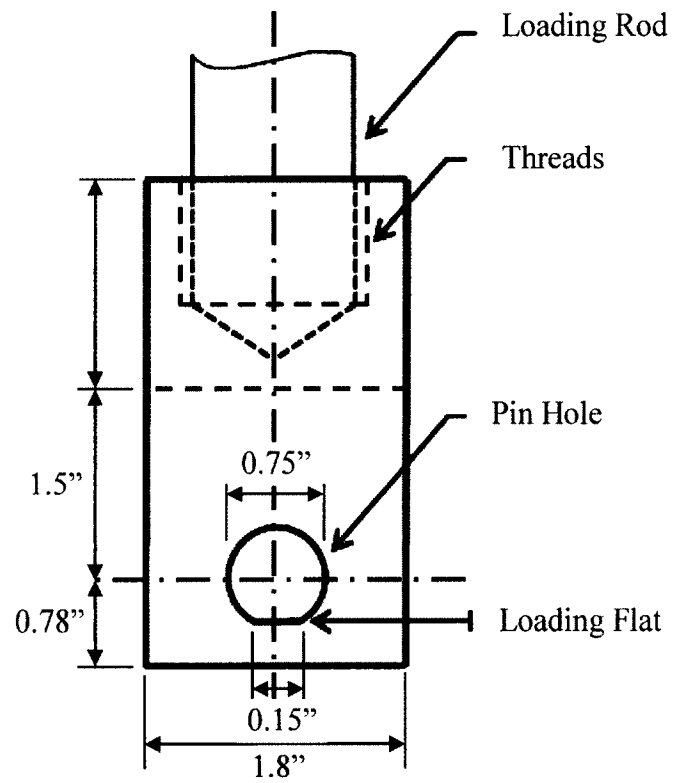


Figure 25. ASTM E399 tension testing clevis.



Figure 26. Fatigue cracking setup.

Fatigue crack initiation and growth was conducted in accordance with the procedures outlined in Annex A2 of ASTM E399 Standard [47]. During this procedure specimens were located into the loading fixture and secured in *S-T* (crack perpendicular to the short transverse (S) and along the long transverse (T)) crack plane orientation as required for the K calculation provided by the Standard. Cyclic fatigue loading was conducted using a sinusoidal waveform in a load control mode. The load cycle was maintained constant, while the maximum K and the ΔK values were allowed to increase with crack growth. The initial value of the maximum fatigue load was calculated using a model provided in the ASTM Standard. The maximum stress intensity factor in the initial portion of the fatigue test did not exceed 80% of the estimated K_{IC} value of the material (ASTM A36 steel) as suggested by Clause A2.4.1 of ASTM E399 [47]. The fracture toughness (K_{IC} value) of ASTM A36 steel was found in the literature to be $75 \text{ ksi}\sqrt{\text{in}}$ at room temperature [172]. The values used for the initial ΔK ranged from $11.8 \text{ ksi}\sqrt{\text{in}}$ to $29 \text{ ksi}\sqrt{\text{in}}$. The cycling frequency varied from 3 to 5 Hz. The values of frequency were chosen according to the machine capability, but from a material standpoint they could potentially be increased to up to 100 Hz, as there was no frequency effect observed on fatigue pre-crack formation up to at least 100 Hz in the absence of adverse environments. The specimen was carefully monitored until crack initiation was observed. The growth of the crack was also monitored to verify symmetrical growth. If crack initiation was not observed on the other side before appreciable growth was observed on the first, then fatigue cycling was stopped, the cause for the unsymmetrical behavior was determined and the remedy executed. If a crack was observed on both surfaces of the specimen the cycling continued until the total length of the notch and crack met the requirements of

clauses 7.3.2.1, 7.3.2.2, and Figure 7 of the standard. The lengths of initiated cracks varied from 0.7 to 1.85 inches long.

Three techniques were implemented for fatigue crack growth measurement. Two of them were based on the crack mouth opening displacement (CMOD), namely clip-on gage CMOD measurement and manual crack mouth opening measurement conducted with a digital caliper. The third technique, back-face strain (BFS) gage measurement, was based on the deformation of the back side of the specimen. CMOD and BFS gage techniques were used to automatically monitor crack length as a function of compliance.

Manual crack mouth opening deflection measurement consisted of the following procedures: suspension of cycling after a certain number of cycles (1,000 to 50,000 cycles), applying static loading of 6 kips and taking measurements of the crack mouth opening using a digital vernier caliper. The resolution of this measurement technique was 0.001 inch. The average of ten measurements was then recorded. The values of the crack mouth opening deflection were further used for crack length and ΔK calculations.

CMOD measurement using a clip-on gage was performed in accordance with the ASTM E399 Standard. The MTS Model 632.02 clip-on displacement gage was implemented. It was designed specifically to meet the ASTM E399 Standard and consisted of two metallic cantilever beams and a gage block as shown in Figure 27.

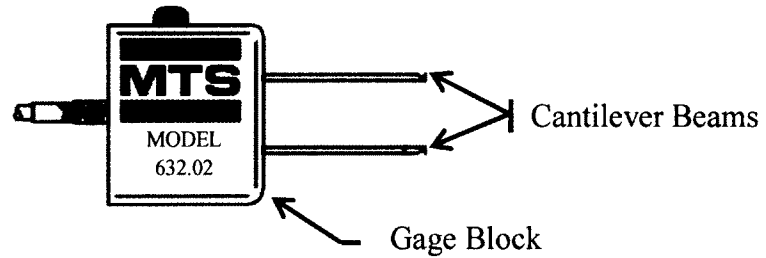


Figure 27. MTS Model 632.02 clip-on displacement gage [173]. Reprinted from Manual 100-007-834B, 2008 with kind permission from MTS Systems Corporation, Eden Prairie, MN, USA.

Figure 28 shows a circuit schematic of the MTS clip-on displacement gage. The clip-on gage used precision resistance-type strain gages bonded to the metallic cantilever beams to form a Wheatstone bridge circuit. The gage was connected to a DC conditioner of the MTS TestStar II testing machine control unit via an extension cable. The DC conditioner processed the signal and made it available to the controller where the signal was recorded and used.

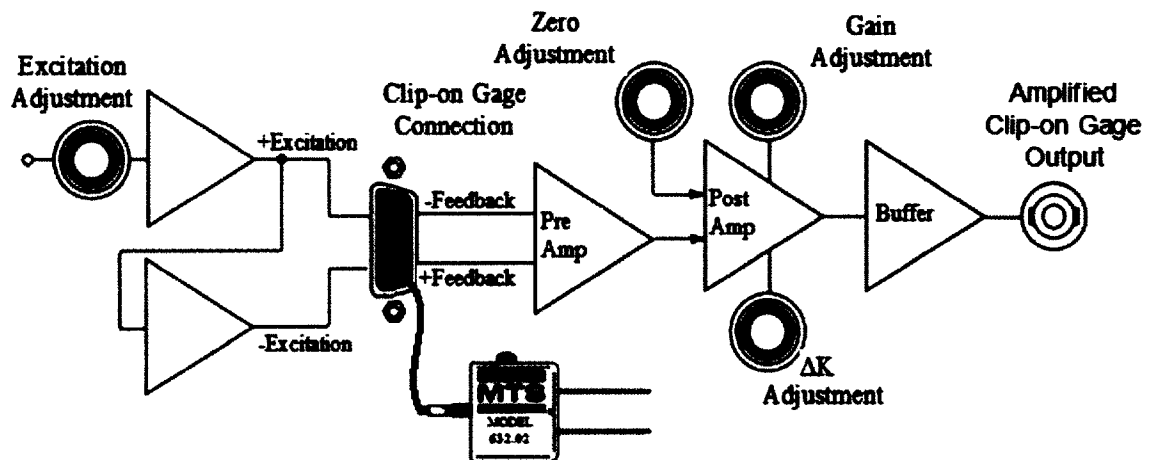


Figure 28. Conditioning circuit of the MTS clip-on displacement gage [173]. Reprinted from Manual 100-007-834B, 2008 with kind permission from MTS Systems Corporation, Eden Prairie, MN, USA.

The clip-on gage was installed into knife edges which were mounted onto a specimen. The alignment fixture provided with the gage set was used to establish the edge length and knife edge alignment. A schematic of knife edge installation is presented in Figure 29. A completed setup of the MTS Model 632.02 clip-on displacement gage attached to a compact-tension specimen is presented in Figure 30.

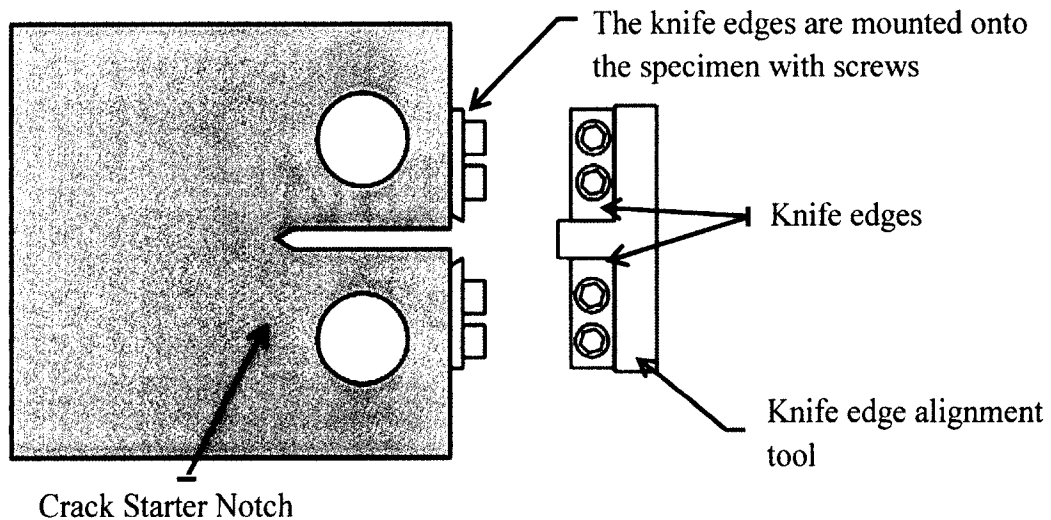


Figure 29. Knife edges installation [173]. Reprinted from Manual 100-007-834B, 2008 with kind permission from MTS Systems Corporation, Eden Prairie, MN, USA.

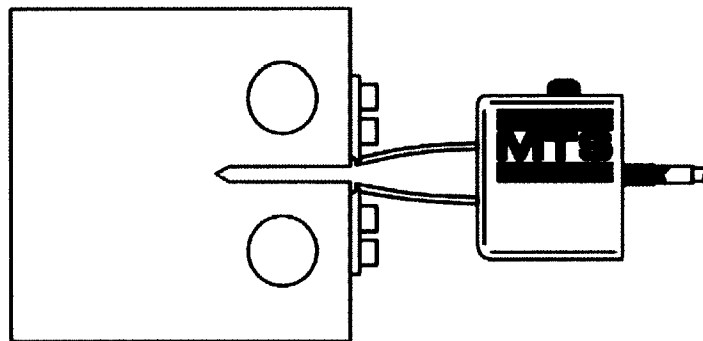


Figure 30. Compact-tension specimen with knife edges and displacement clip-on gage attached [173]. Reprinted from Manual 100-007-834B, 2008 with kind permission from MTS Systems Corporation, Eden Prairie, MN, USA.

Prior to conducting the crack mouth opening displacement measurement the signal from the clip-on gage was calibrated according to the procedures described in the gage manual (MTS 100-007-834B manual) [173]. The calibration process coordinated the interaction between the transducer and a DC conditioning circuit. After calibration the clip-on gage was deployed by clipping it between the knife edges on the specimen (see Figure 30). According to the ASTM E399 compliance method, the crack length in the specimen is a function of the crack mouth opening displacement achieved at a given applied load value. Since peak values are not required for crack length determination the measurement of the crack mouth opening can be done at frequencies lower than the cycling frequency. In this study the measurements of crack mouth opening displacement from the clip-on gage were recorded every 30 seconds. The data obtained was then converted into crack length using formula A4.4 from clause A4.5.6 of the ASTM E399 Standard.

The Back-face Strain (BFS) gage method was developed by Dean and Richard in 1979 [174]. This crack growth measurement method was based on a linear relationship between the strain on the back face of the E399 compact tension (CT) specimen and the crack length. A strain gage was bonded to the center of the back face of the specimen (the face opposite to that from which the notch slot was machined), in the plane of the crack as shown in Figure 31. The signal of the gage was recorded using the HP Agilent 34970A data acquisition system. A back-face compliance relationship for the ASTM E399 compact tension specimen was developed by Newman and his colleagues in 2011 to obtain crack length values from the back-face strain data [175].

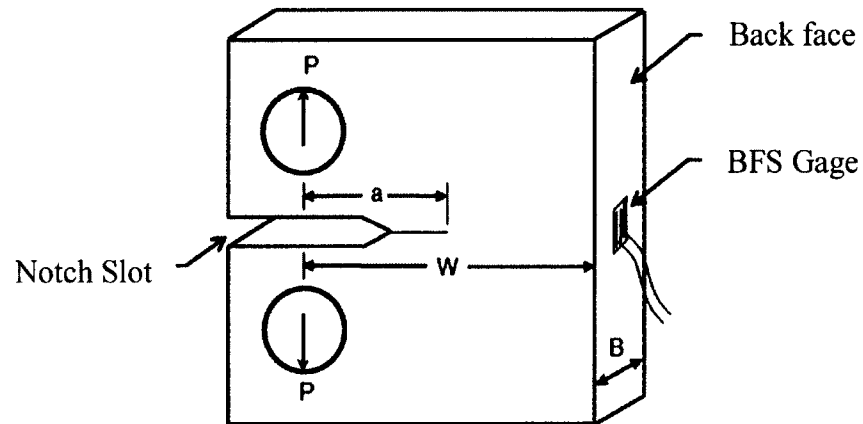


Figure 31. Back-face strain gage attached to the ASTM E399 compact-tension specimen [175]. Reprinted from “Back-face strain compliance relation for compact specimens for wide range in crack lengths”, *Engineering Fracture Mechanics*, 2011, p. 2708, J C Newman, with kind permission from Elsevier (License #3417960415748).

3.2 Electrochemical Fatigue Crack Treatment

Fatigue crack treatment consisted of electro-deposition of nickel onto the fatigue crack surfaces. A solution reservoir inside the specimen was created by applying non-conductive tape on the interior surfaces of the notch slot as shown in Figure 32. This allowed focusing of the treatment directly onto the crack surfaces.

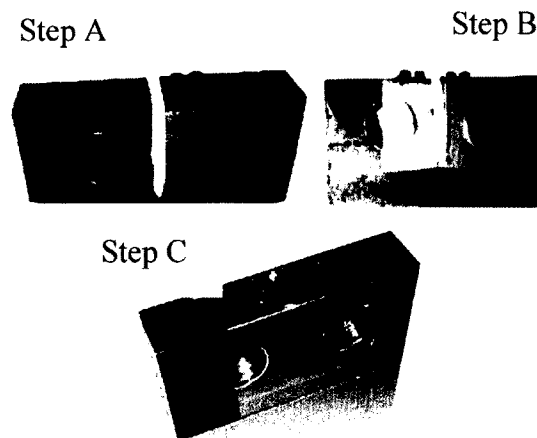


Figure 32. Assembly steps for creating a treatment solution reservoir inside the specimen.

The reservoir was filled with Watt's nickel plating bath solution [150]. The bath composition, operating conditions and mechanical properties are presented in Table 4, Section 2.2.3. After the bath solution was poured into the reservoir, the specimen was subjected to static loading using the static loading armature shown in Figure 33. Placing the bath into the crack prior to opening the crack helped prevent the formation of air bubbles at the crack tip which could interfere with plating. The specimen crack mouth was opened up to as well as above the size that was reached during initial cyclic loading that occurred prior to treatment.

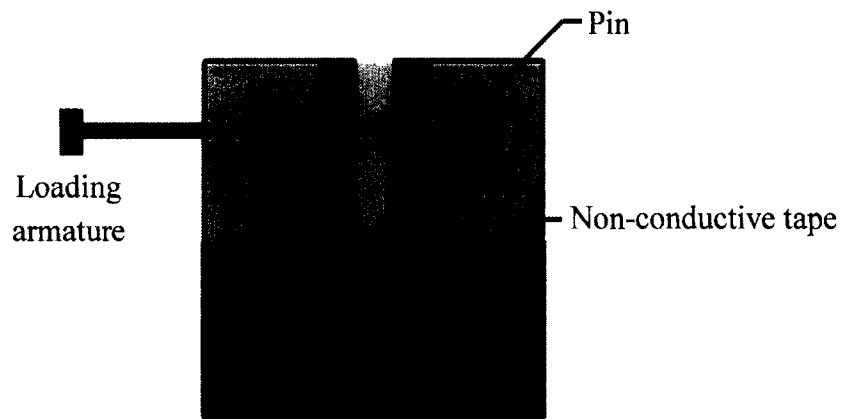


Figure 33. The specimen opened using a static loading armature.

After the crack was opened the specimen was placed onto a hot plate. The temperature of the hot plate was kept at 60 °C to match the plating bath requirements provided in Table 4. The plating bath temperature was monitored by immersion of a digital thermometer into the liquid. A titanium electrode, used as a counter electrode, was placed into the plating bath. All but the tip of the electrode was covered with a non-conductive tape in order to focus the treatment onto the tip of the fatigue crack.

The specimen and the electrode were connected to an external power supply allowing direct current flow. The specimen was connected to the negative terminal and the titanium electrode was connected to the positive terminal of the power supply. The electrochemical treatment setup is schematically shown in Figure 34.

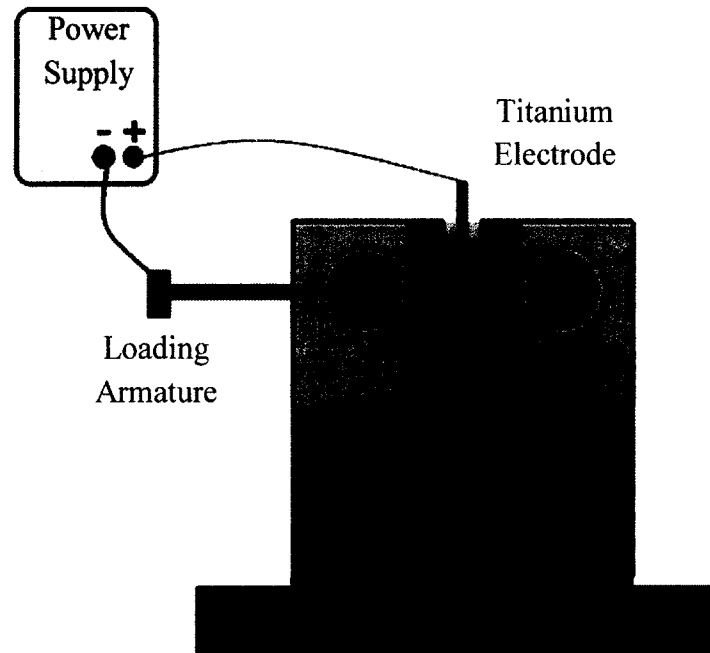


Figure 34. Electrochemical treatment setup.

The power supply was set for current control and provided an amperage flux of between 0.13 Amps/cm^2 and 0.15 Amps/cm^2 as suggested by Watt's plating bath requirements [150]. The conductive area was calculated using the crack length and the thickness of the specimen. All specimens were electrochemically treated for one hour. When the treatment was finished the static loading armature and the tape were removed. The specimen was washed with deionized water and ethyl alcohol; air dried and placed

into a sealed container with indicating Drierite desiccant (Hammond DRIERITE Co. LTD, Xenia, OH, USA).

3.3 Treated Crack Growth

After treatment the specimen was again subjected to the same magnitude and frequency of loading as was applied during the pre-treatment cycling. Cycling was periodically paused and the specimen was again statically loaded to assess crack propagation. The crack mouth opening deflection was measured using CMOD and BFS gages, or using a digital caliper to assess crack propagation as described in Section 3.1. Post-treatment cycling continued until crack propagation was quantified or specimen fracture was observed.

3.4 Scanning Electron Microscopy

Scanning Electron Microscopy (SEM) was implemented for studying surface topography, as well as the composition and distribution of nickel deposits on treated specimens. Three scanning electron microscopes were used during this study, namely the Phenom Pro G2 (PhenomWorld Inc., Eindhoven, Netherlands), the TM-1000 (Hitachi, Tokyo, Japan) and the S-4800 (Hitachi, Tokyo, Japan) (see Figure 35). SEM images and their analysis are presented in Section 4.3.

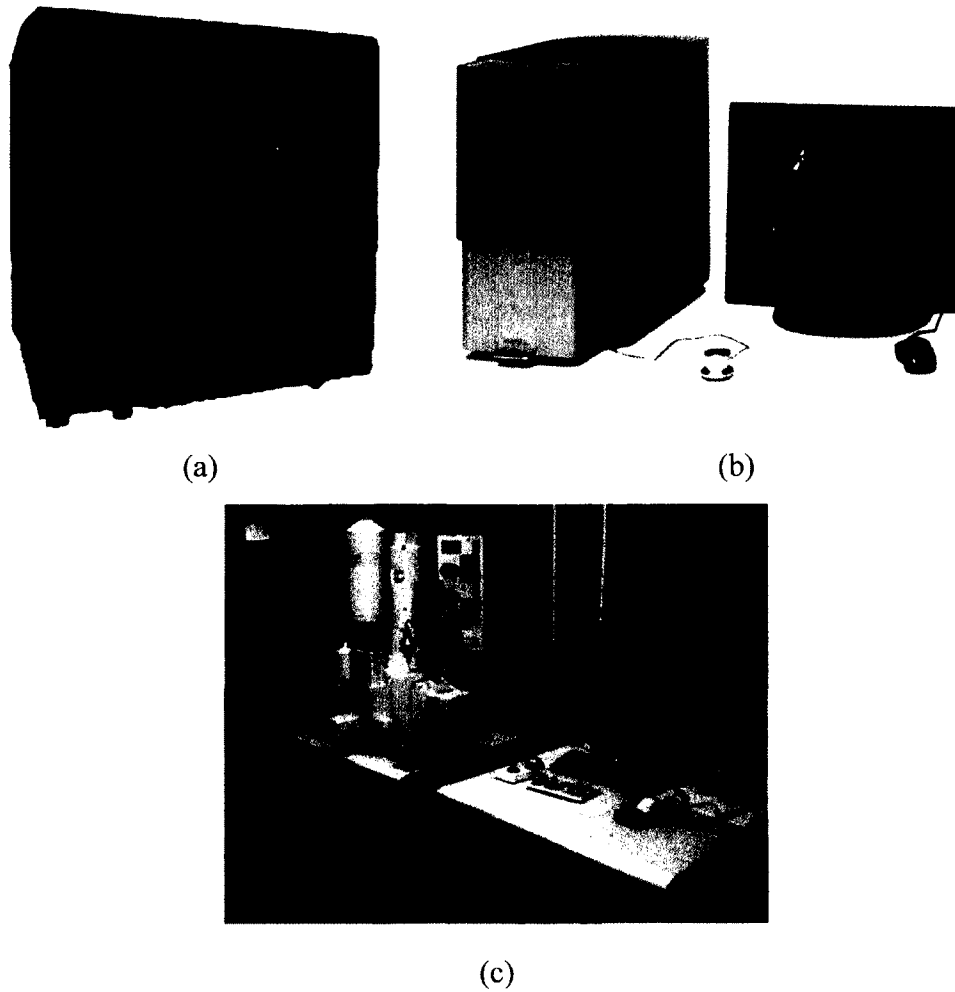


Figure 35. Scanning electron microscopes: (a) TM-1000 (Hitachi Ltd, Tokyo, Japan); (b) Phenom Pro G2 (PhenomWorld Inc., Eindhoven, Netherlands). Reprinted with kind permission from PhenomWorld Inc.; (c) S-4800 (Hitachi Ltd, Tokyo, Japan).

Prior to imaging each specimen was cut, cleaned, polished, and attached to a SEM specimen base. Initially a small part of the CT-specimen was cut as shown in Figure 36.

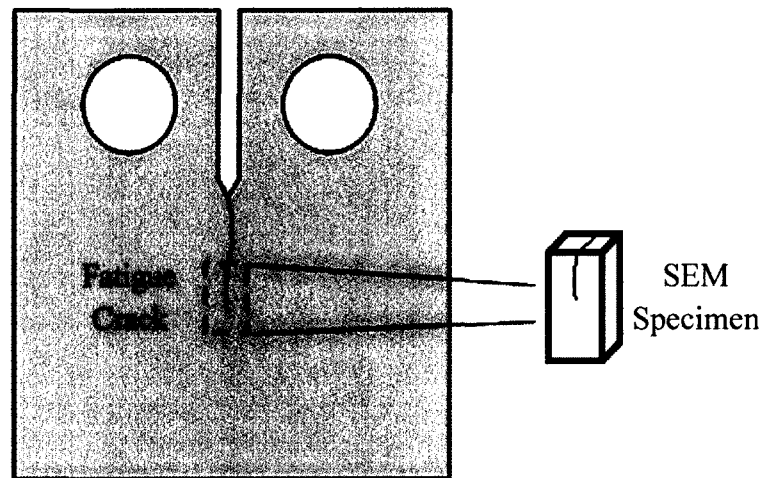


Figure 36. A portion of the ASTM E399 compact tension specimen cut for scanning electron microscope imaging.

A band saw was used for initial sectioning and a diamond blade saw was used for a finishing cut. The cut specimen was washed, degreased and air dried. The dried specimen was then prepared for polishing. The specimen was put into a cylindrical plastic vacuum mold with the surface to be imaged facing to the bottom of the mold. The mold was then filled with epoxy using the Cast n' Vac 1000 (Buehler Inc., Lake Bluff, IL, USA) castable vacuum system and left to harden for 24 hours. The hardened epoxy with the specimen embedded was then removed from the mold and polished. Figure 37 shows the specimen molded with epoxy prior to polishing.



Figure 37. The specimen molded with epoxy and ready to be polished.

A 60-1990 model grinder-polisher (Buehler Inc., Lake Bluff, IL, USA) was used for polishing. The polishing procedure was suggested by the polishing machine manufacturer. The specimen was polished with a sequence of sandpapers going from a coarse (240 Coated Abrasive Manufacturers Institute (CAMI) grit) to a fine one (1200 CAMI grit). A 50-50 mixture of ethylene glycol and ethyl alcohol 190 proof was used for lubrication. Finishing polishing was done using a Texmet polishing pad with addition of 1 μm alumina particles. The polishing setup can be observed in Figure 38.

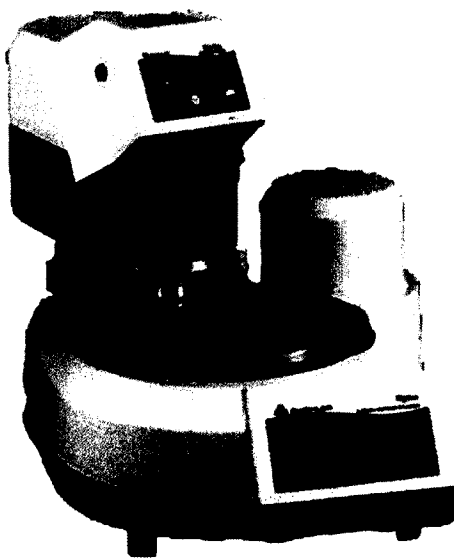


Figure 38. 60-1990 grinder-polisher (Buehler Inc., Lake Bluff, IL, USA) loaded with molded specimens [176]. Reprinted with kind permission from Buehler Inc.

Polished specimens were washed with ethyl alcohol and dried in a container with indicating Drierite desiccant for 24-48 hours. Cylindrical specimens were cut into a rectangular shape in order to fit the chamber of an SEM. Cut rectangular specimens were again washed with ethyl alcohol and placed into a container with indicating Drierite desiccant for 24-48 hours. Dried specimens were attached to an SEM specimen base

using SPI #04998-AB conductive silver paint (SPI Supplies Division, Structure Probe Inc., West Chester, PA, USA). An example of the specimen ready to be imaged is shown in Figure 39. Results and images obtained using scanning electron microscopy are presented in Section 4.3.

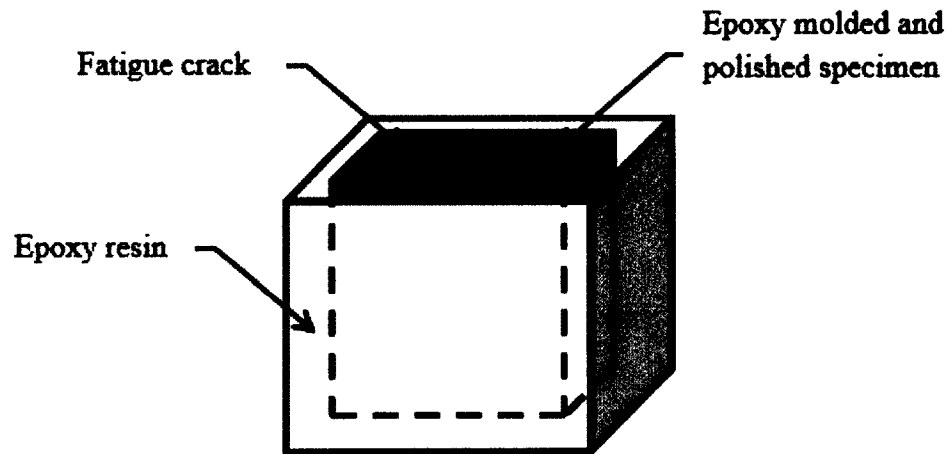


Figure 39. An example of a specimen mounted on an aluminum SEM specimen base using silver paint and prepared for imaging.

3.5 Optical Microscopy

Optical microscopy was used to obtain the dimensions of the notch and fatigue crack of ASTM E399 compact tension specimens, and for determination of nickel deposit distribution in a treated fatigue crack.

ASTM E399 compact tension specimens were analyzed before and after electrochemical treatment using Moticam 1000 1.3Mpx (Motic Inc., Hong-Kong) digital microscope connected to a computer with Images Plus 2.0 (Motic Inc., Hong-Kong) imaging software. The specimens were imaged unloaded and under static load of 6 kip

applied before and after the treatment using loading the armature shown in Figure 33. The data and images obtained using optical microscopy can be found in Section 4.3.

3.6 Energy-dispersive X-ray Spectroscopy

Energy-dispersive X-ray spectroscopy (EDS) was used for elemental analysis and chemical characterization of electrochemically treated specimens. This technique helped to confirm deposition of nickel on crack surfaces and to characterize its distribution.

Spectroscopic analysis was performed using a tabletop scanning electron microscope (SEM) TM-1000 (Hitachi Ltd, Tokyo, Japan) (see Figure 35, a) with an EDS module and S-4800 (Hitachi Ltd, Tokyo, Japan) SEM with EDAX EDS module (EDAX Inc., Mahwah, NJ, USA) (see Figure 35, c).

The preparation of the specimens for the spectrographic analysis was similar to the preparation of the SEM specimens described in Section 3.4., but, in contrast to the SEM specimens, the EDS specimens were not polished to avoid alteration of the outer surface of the plated nickel.

During the spectroscopic analysis rectangular areas of the specimens were studied using the “Area” mode of the EDS. Obtained data provided the quantification of elements concentrated at the studied regions. The results of the spectroscopic analysis are presented in Section 4.4.

3.7 Corrosion Susceptibility Determination

A corrosion susceptibility study was performed to evaluate the effect of nickel plating on the corrosion resistance of the ASTM A36 steel. The specimens for this study

consisted of five nickel plated and five bare ASTM A36 steel rectangular plates, and one electrolytic nickel strip (nickel deposit) separated from a previously plated specimen. The following sections describe these procedures.

The preparation of the ten rectangular A36 steel specimens consisted of machining, sand blasting, cleaning, covering with epoxy and electroplating (of the nickel plated specimens). Electrolytic nickel strip preparation consisted of only cleaning with ethyl alcohol 190 proof prior to placement into a corrosive environment.

The rectangular specimens were cut from flat bar of ASTM A36 steel using a band saw. The dimensions and geometry of the specimens are presented in Figure 40.

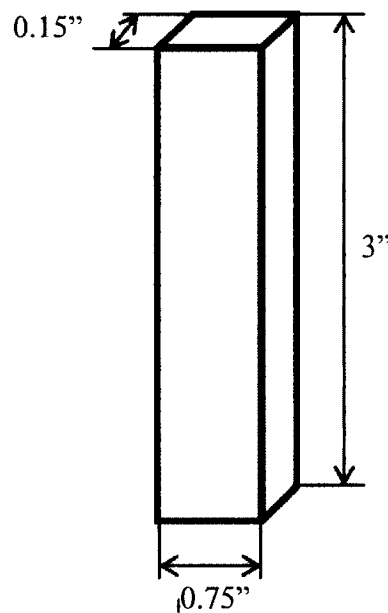


Figure 40. Dimensions and geometry of ASTM A36 steel specimen used for corrosion susceptibility testing.

Machined specimens were sand blasted using a SBCNNS (Black Bull Inc., Salt Lake City, UT, USA) sandblaster cabinet using glass abrasive in order to remove dirt,

cutting lubricant and possibly existing corrosion spots. After sand blasting the specimens were cleaned using methyl alcohol. The cleaned specimens were air dried and put into a container with indicating Drierite desiccant to await epoxy coating.

The specimens were coated with epoxy leaving only two areas uncovered, the area destined to be exposed to a corrosive environment and an electrode connection area at the top of the specimen as shown schematically in Figure 41.

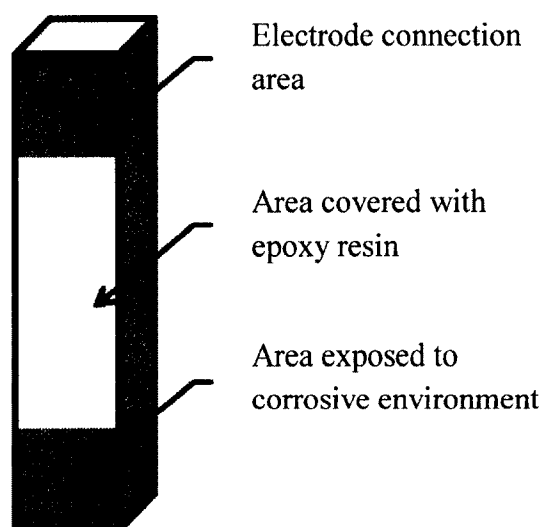


Figure 41. Schematic representation of the ASTM A36 steel specimen covered with epoxy resin.

The specimens covered with epoxy were kept for 24 hours in a dry environment at room temperature to let the epoxy cure. When the epoxy hardened the uncovered areas of the specimens were again sandblasted and cleaned with ethyl alcohol 190 proof.

Nickel plating was applied to five of the ten rectangular steel specimens covered with epoxy. The electroplating process and conditions were similar to the electrochemical treatment of fatigue cracks that was applied to the ASTM E399 compact-tension

specimens described in Section 3.2. A specimen was placed into the Watts' solution bath with a negative power supply lead attached to its top area as illustrated in Figure 42. The positive lead was attached to a titanium counter electrode. Electrodeposition lasted for 1 hour at an amperage flux of between 0.13 A/cm^2 and 0.15 A/cm^2 as per Watts' plating bath requirements [150].

When the nickel deposition was finished each specimen was placed into an opening in a 100 ml plastic container. Each container was covered with duct tape. The containers were filled with 3.5 wt% NaCl solution simulating seawater. An example of an epoxy covered specimen placed into a container with corrosive environment is illustrated in Figure 42.

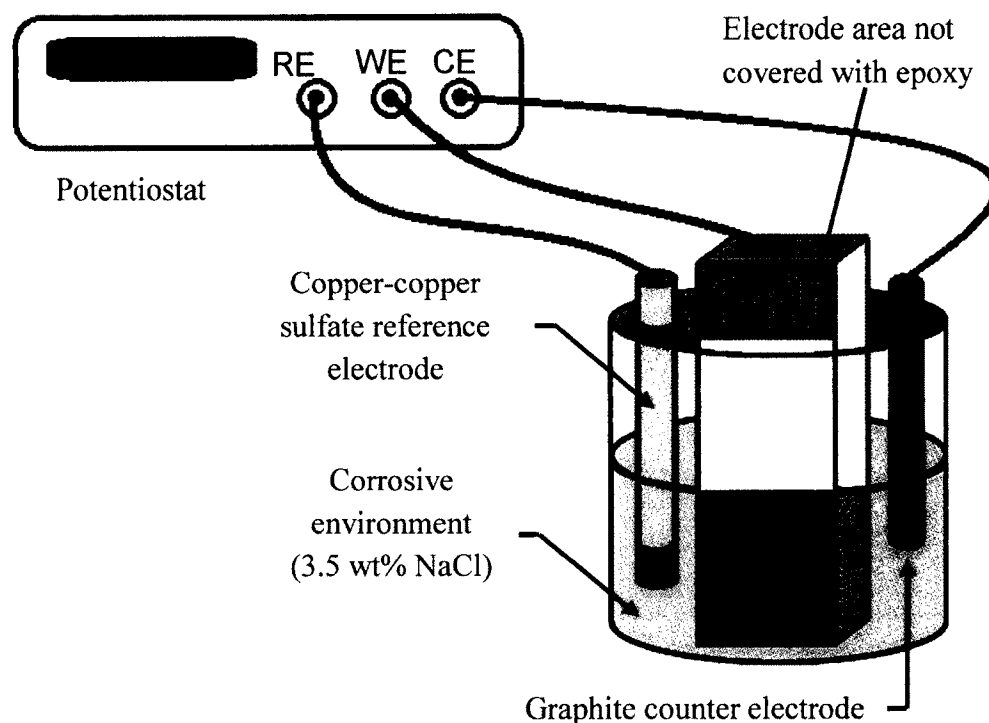


Figure 42. An example of a rectangular steel specimen covered with epoxy and placed into container with a corrosive environment (3.5 wt% NaCl).

The area of the rectangular steel specimen exposed to the corrosive environment during the corrosion susceptibility testing was 4.84 cm^2 . It was chosen based on the average crack length and the thickness of the treated specimens. The area of the nickel strip was 0.9 cm^2 .

An SI 1287 (Solartron Analytical Inc., Hampshire, GU14 0NR, UK) potentiostat connected to a PC with the CorrWare software version 3.3e (Solartron Analytical Inc., Hampshire, GU14 0NR, UK) was used to take measurements of corrosion potential and corrosion current density. The measurements were taken weekly during a 12 week period. All the measurements were taken at room temperature ($22 \text{ }^\circ\text{C} - 25.2 \text{ }^\circ\text{C}$). As shown in Figure 42 the measurement cell of the potentiostat consisted of a specimen, a graphite counter electrode and a copper/copper sulfate reference electrode. The potentiostat scan was run at a rate of 0.1 mV/sec within a range of $\pm 30 \text{ mV}$ from the corrosion potential of the specimen. The linear polarization resistance method was then applied to calculate the corrosion rate and current.

The galvanic corrosion rate between ASTM A36 steel and the electrolytic nickel deposit strip was measured using a galvanostatic zero resistance ammeter (GZRA) method [164]. The experimental setup for this method consisted of an ammeter and a power source connected in series with the anode (electrolytic nickel strip) and cathode (ASTM A36 steel). A high input impedance voltmeter was connected in parallel to the anode and cathode. Both the steel and nickel specimens were immersed in the same electrolyte (3.5 wt% NaCl water solution). The exposed surface area of the each specimen was 0.9 cm^2 . The reading of the voltmeter was monitored during adjustment of the current generated by the power supply until the potential difference between the

anode and the cathode was reduced to zero. This means that the power supply is providing just enough of a boost to overcome the inherent resistance of the ammeter. At that moment the true galvanic corrosion current displayed by the ammeter was recorded. Results of the corrosion measurements are presented in Section 4.6.

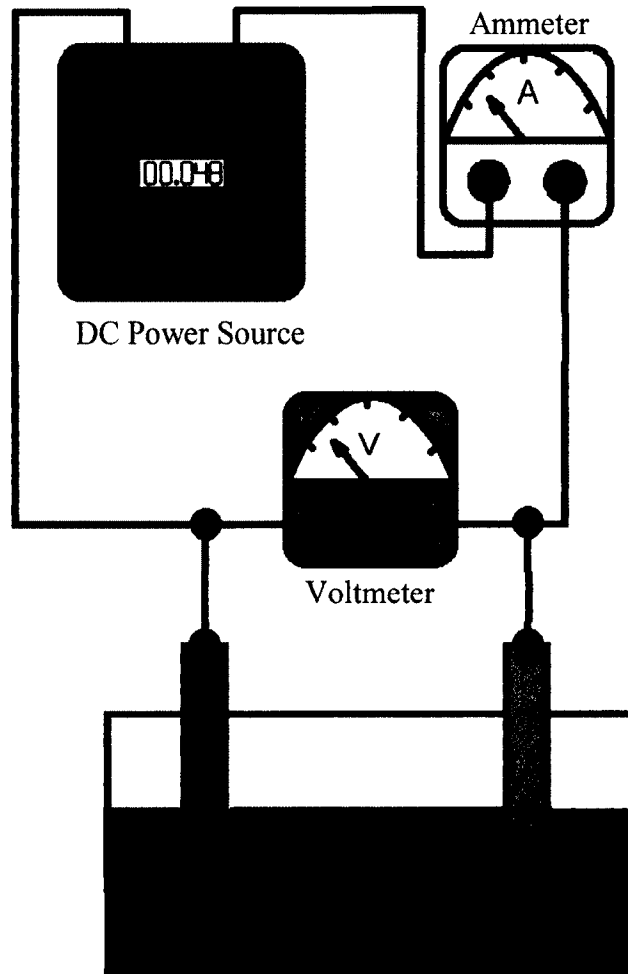


Figure 42-2. The schematic of the experimental setup for galvanic corrosion measurement using Galvanostatic Zero Resistance Ammeter (GZRA) method [164].

3.8 Finite Element Modeling and Simulation

Finite Element Modeling (FEM) and simulation was done to serve as a comparison to the experimental and analytical results. This method allowed analysis of the assumptions made in the research and evaluation of the obtained experimental data.

A dynamic transient finite element analysis technique was used for this study. The analysis was divided into 3 time steps: (1) subjecting a CT-specimen with a fatigue crack to static loading; (2) inserting a layer of nickel (simulating nickel deposition); (3) releasing the static loading with nickel deposited on the crack surfaces. The schematic of the steps of the finite element analysis is shown in Figure 43.

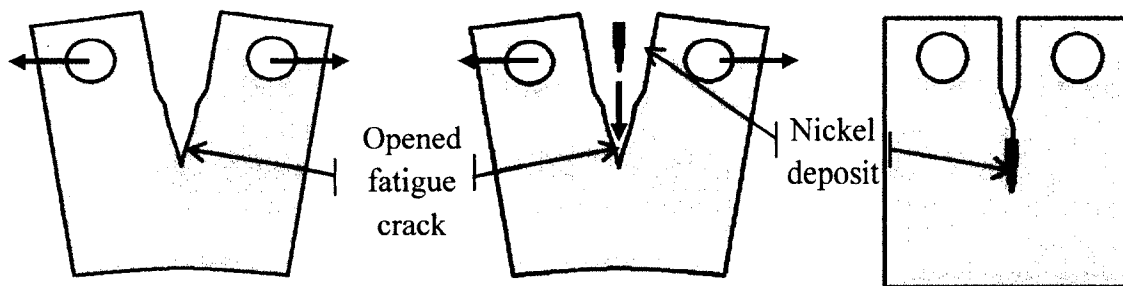


Figure 43. The steps of the finite element analysis: (1) subjecting a CT-specimen with a fatigue crack to static loading; (2) inserting a layer of nickel (simulating nickel deposition); (3) releasing static loading while nickel is deposited on crack surfaces.

A 2D model of an ASTM E399 compact-tension specimen with a fatigue crack was designed in ANSYS 14 (ANSYS, Inc., Canonsburg, PA, USA). The dimensions of the specimen were the same as of the specimens used during experimental cycling. The size of the crack was 1.4 inch from the point of load application or 0.7 inch from the notch tip. The size of the crack was chosen based on the average crack size reached during experimental cycling. The crack at this length was outside of the influence of the

notch. The material properties of the ASTM A36 steel provided in Table 6 were used as material properties of the CT-specimen model. The material properties of the nickel deposit used for the finite element analysis are presented in Table 7.

Table 7. Material properties of the nickel deposit for the finite element modeling and analysis

Properties	Values
Density, ρ (lb/in ³)	0.32
Young's modulus, E (psi)	29x10 ⁶
Poisson's ratio, ν	0.31

The model was automatically meshed by ANSYS and divided into 28,842 four-noded linear triangle and quadrilateral Shell 181 finite elements with six degrees of freedom. The minimum size of an element was 0.02 mm, the maximum was 0.5 mm. The mesh was refined at the notch tip. The meshed model of the specimen is shown in Figure 44.

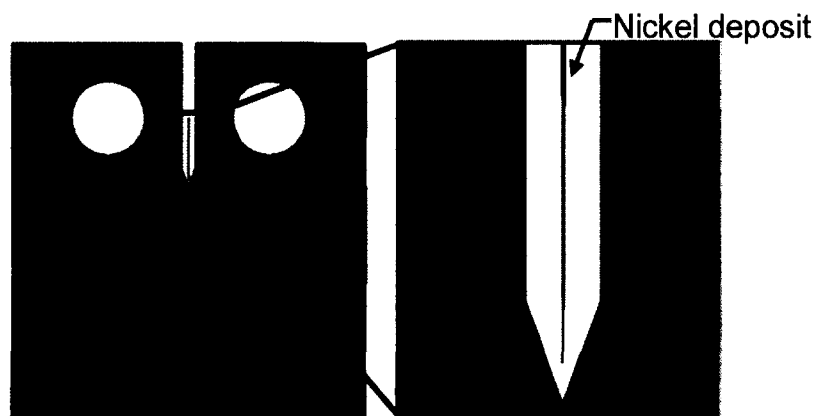


Figure 44. ASTM E399 compact-tension specimen and nickel deposit meshed in ANSYS.

The electrochemical treatment was modeled as an introduction of a thin nickel layer packing the fatigue crack (see Figure 43) and alternatively as an introduction of a nickel clump (see Figure 45) wedging the crack. Three models of the nickel layer were designed. The models varied by length. The lengths were as follows: 0.7 inch (100% of the crack length), 0.35 inch (50% of the crack length), and 0.07 (10% of the crack length). The nickel clump was modeled in one set of dimensions shown in Figure 45. It was positioned 5 mm (0.197 in) away from the crack tip corresponding to spectroscopy analysis findings (see Section 4.4). The nickel clump was designed with the arc-shaped top and bottom sides similar to those observed in microscopic images.

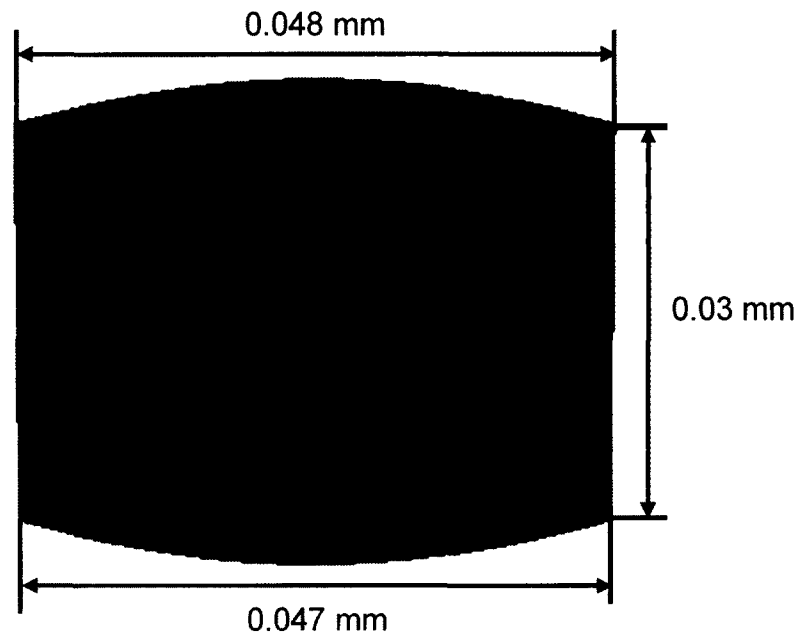


Figure 45. Nickel clump model meshed in ANSYS.

The boundary conditions were applied to the CT-specimen and to the nickel layer as shown in Figure 46. The boundary conditions varied for each time step of the transient analysis. The boundary conditions for the finite element analysis (FEA) of crack wedging

with a nickel clump are shown in Figure 47. The finite element analysis provided an elastic solution. The results and discussion of the FEA are presented in Section 4.5.

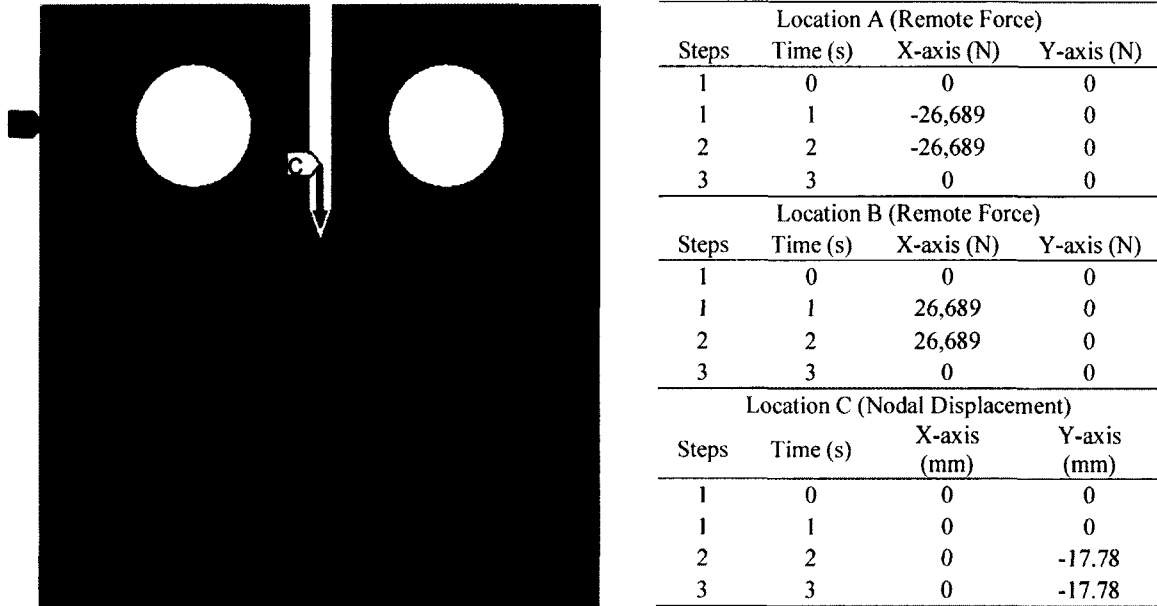
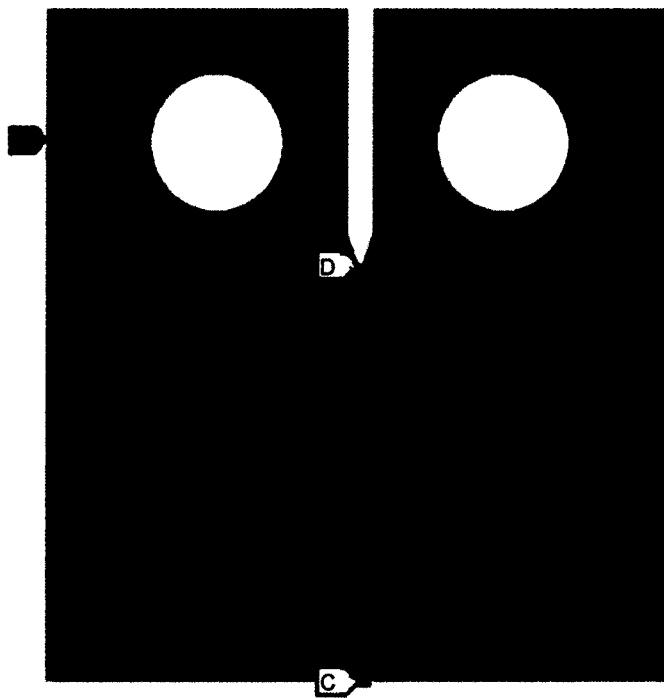


Figure 46. The boundary conditions applied to the CT-specimen and nickel layer models at 3 steps of the dynamic transient finite element analysis. Label “C” represents nickel layer deposit. Units: Newton (N), mm.



Location A (Remote Force)			
Steps	Time (s)	X-axis (N)	Y-axis (N)
1	0	0	0
1	1	26,689	0
2	2	26,689	0
3	3	0	0
Location B (Remote Force)			
Steps	Time (s)	X-axis (N)	Y-axis (N)
1	0	0	0
1	1	-26,689	0
2	2	-26,689	0
3	3	0	0
Location C (Nodal Displacement)			
Steps	Time (s)	X-axis (mm)	Y-axis (mm)
1	0	0	0
1	1	0	0
2	2	0	0
3	3	0	0
Location D (Nodal Displacement)			
Steps	Time (s)	X-axis (mm)	Y-axis (mm)
1	0	0	0
1	1	0	0
2	2	0	-12.78
3	3	0	-12.78

Figure 47. The boundary conditions applied to the CT-specimen and nickel clump at 3 steps of the dynamic transient finite element analysis. Label D represents nickel clump deposit. Units: Newton (N), mm.

CHAPTER 4

RESULTS AND DISCUSSION

In this chapter the results of experimental, analytical and simulation studies are presented and discussed. The concept and the usefulness of the proposed fatigue crack treatment technology in steel pipelines are discussed. The discussion focuses on understanding the results and their comparison to the literature and research in order to ascertain whether these findings support or contradict the current crack arrest hypothesis. The discussion demonstrates how the knowledge of fatigue crack treatment has been changed by the addition of this new study.

4.1 Fatigue Crack Initiation and Growth

In this study fatigue cracks in ASTM E399 Standard compact-tension (CT) specimens made of ASTM A36 steel were initiated and grown as described in Section 3.1. Some of the cracks were further treated using the proposed electrochemical method and some were also grown without treatment in order to serve as control specimens. An example of fatigue crack growth behavior in control specimens is shown in Figure 48.

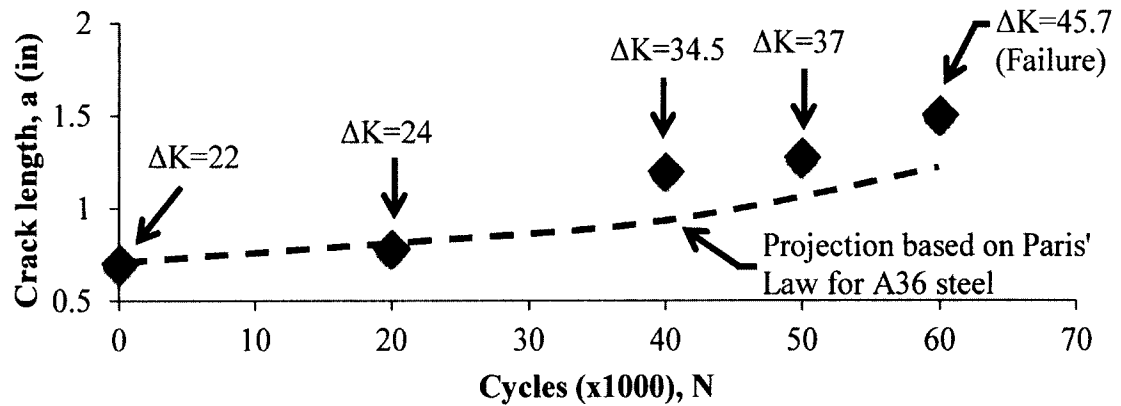


Figure 48. Fatigue crack propagation in specimen C without electrochemical treatment. ΔK units - $\text{ksi}\sqrt{\text{in}}$.

The fatigue crack in specimen C was grown using constant maximum and minimum loads. The stress ratio ($\frac{\sigma_{min}}{\sigma_{max}}$) was equal to 0.26. Under these conditions the value of the stress intensity factor range (ΔK) was increasing with the crack growth. The average rate of the crack growth (da/dN) was 1.33×10^{-5} inch/cycle. Figure 49 contains a compilation of da/dN data used to compare the results of this study to prior work [177]. This data was acquired from tests conducted on ASTM A36 steel from 1971-1987. No information was available as to the state of anneal for material used to obtain this data.

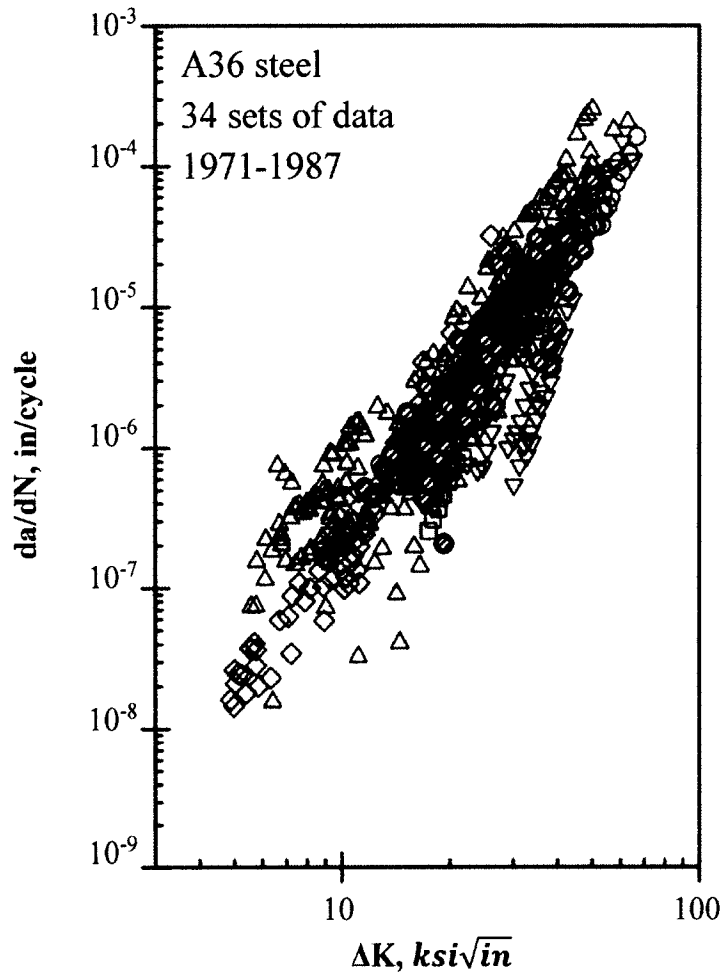


Figure 49. 34 sets of fatigue crack growth data for ASTM A36 steel [178]. Blue dashed circles represent data obtained during the current study. Reprinted from "Damage Tolerance Analysis of Tank Car Stub Sill Cracking", 1998, J W Cardinal, P C McKeighan, S J Hudak, with kind permission from Southwest Research Institute.

The range of crack behavior starts at 10^{-8} in/cycle and goes up to a rate of 10^{-3} in/cycle. In the current study the range of propagation rates were $10^{-7} - 10^{-4}$ in/cycle. As shown in Figure 49 the da/dN rates of the current study are represented by dashed circular points. It was observed that the data from the present study is all located within the scatter band of the data from the literature [177,179]. In general, the growth rates of

all fatigue cracks observed before treatment were in a good correlation with data found in the literature, as shown in Figure 49.

It is currently a general practice to characterize the rate of fatigue crack growth using the Paris Law as described in Section 2.1.6. In order to serve as a reference, the projection of the fatigue crack growth in specimen C, according to the Paris Law, was plotted as a dashed line in Figure 48. The projection was constructed by inserting actual ΔK and dN values (from the current study) into the Paris Law and solving it for da . The power law coefficients that were used for the da calculation were specific to ASTM A36 steel ($C = 7 \times 10^{-10}$, $m = 2.8$). These coefficients were found by Barsom and confirmed by Fisher [177,180]. In Figure 48, the ΔK and dN values for each of the five data points were used to calculate the corresponding Paris Law points. The dashed line is a curve fit through these five calculated points. In the case of specimen C the projection resulted in under-prediction of crack propagation. This Paris Law projection appears to be a reasonable approximation when taking into account the small number of data points considered. Specimen C failed within 60,000 cycles at ΔK equal to $45.7 \text{ ksi}\sqrt{\text{in}}$. The value of the plain strain fracture toughness (K_{Ic}) of ASTM A36 steel observed in the literature varied from $45 \text{ ksi}\sqrt{\text{in}}$ to $67 \text{ ksi}\sqrt{\text{in}}$ [84,181,182].

Figures 50-53 demonstrate behaviors of cracks before and after treatment. Figure 50 shows the history of fatigue crack propagation in specimen D.

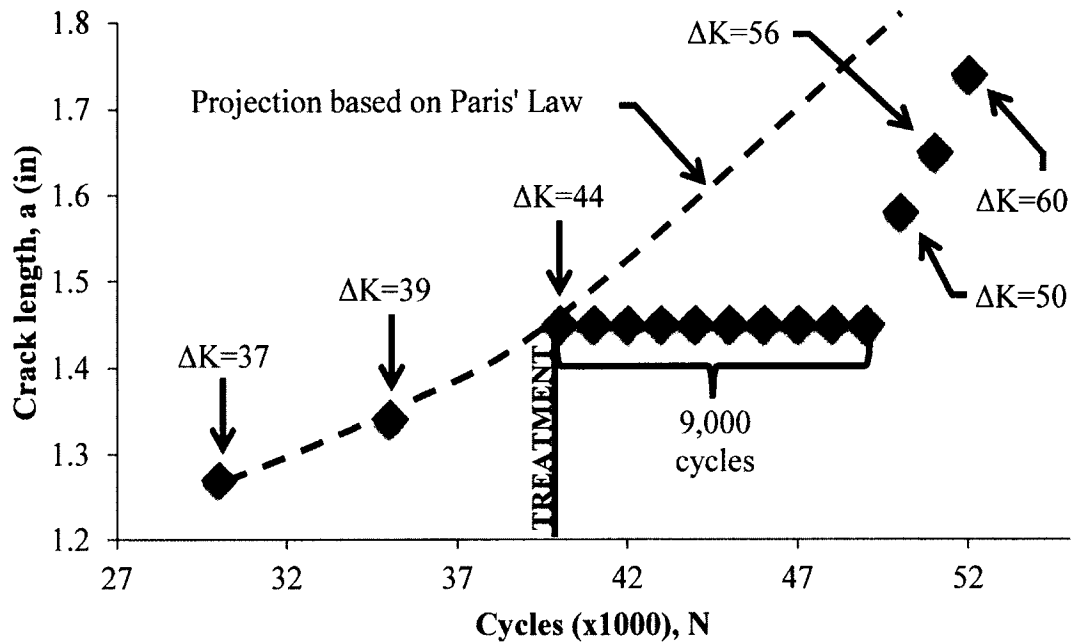


Figure 50. Fatigue crack propagation in ASTM A36 steel CT specimen D before and after electrochemical treatment. The units of ΔK were $\text{ksi}\sqrt{\text{in}}$. The dashed line represents the projected behavior of a fatigue crack without electrochemical treatment based on the Paris Law.

The fatigue crack in specimen D was treated after 40,000 cycles when its length was 1.45 inches and $\Delta K = 44 \text{ ksi}\sqrt{\text{in}}$. The cyclic loading of the specimen continued after treatment at $\Delta K = 44 \text{ ksi}\sqrt{\text{in}}$. From Figure 50 it was observed that the fatigue crack was continuously growing before treatment at an average rate of 1.5×10^{-5} inches/cycle. The projection of crack propagation based on the Paris Law was very close to the actual values before treatment. After treatment the crack stopped propagating. During the next 9,000 cycles no crack propagation was observed and the average rate of crack growth (da/dN) was equal to zero. After 9,000 cycles the crack appeared to re-initiate with a local average propagation rate of 8×10^{-5} inches/cycle, which was comparable to Paris Law approximation (6.1×10^{-5} inches/cycle). (It was not clear whether the crack re-

initiated from the point where the tip existed prior to treatment or if it had re-initiated from a “new” crack tip location that may have been created by the plating treatment). The cyclic loading of specimen D was stopped after 52,000 cycles at $\Delta K = 60 \text{ ksi}\sqrt{\text{in}}$. The specimen did not fail. The behavior of the crack in specimen D after treatment differed from its behavior before treatment. Until the point of treatment the fatigue crack growth was well characterized by the Paris Law. It deviated from this behavior after treatment was applied.

Based on these observations and the Paris Law projection the fatigue crack in specimen D, if not treated, would have grown up to 1.76 inches long within 9,000 cycles from the treatment point. The treatment effectively arrested the fatigue crack at a length of 1.45 inches for a period of 9,000 cycles. In order to compare the fatigue behaviors of treated and non-treated cracks two cycling histories were plotted together in Figure 51. Both specimens were cycled under the same loading conditions. In both of these cases the maximum load (P_{max}) was equal to 8.3 kip; the minimum load (P_{min}) was equal to 2.15 kip. The frequency was equal to 5 Hz.

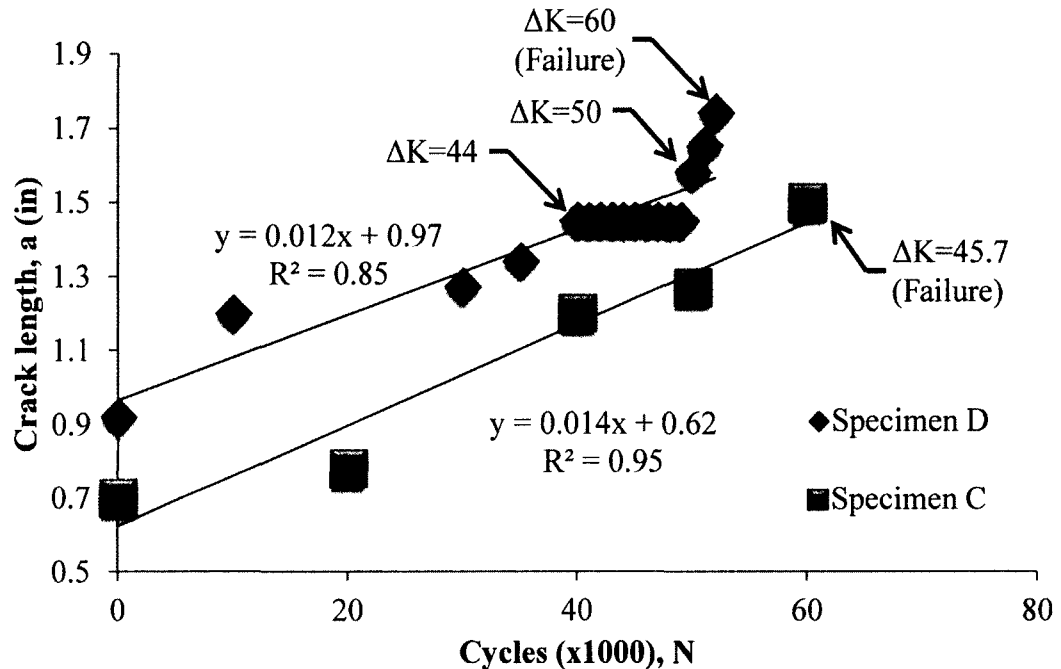


Figure 51. Fatigue crack propagation in specimen C (not treated) and in specimen D (treated). ΔK units - $\text{ksi}\sqrt{\text{in}}$.

From Figure 51 it was observed that both cracks were propagating with an average rate of $\sim 1.5 \times 10^{-5}$ inches/cycle. For example, the fatigue crack in specimen C grew from 1.27 inches to 1.5 inches in 10,000 cycles. During the same number of cycles the fatigue crack in specimen D grew from 1.27 inches to 1.45 inches. The difference was only 0.05 inches thus it appears that the growth rates of these fatigue cracks before treatment were similar. The fatigue crack in specimen C was continuously growing and failed after 60,000 cycles at $\Delta K = 45.7 \text{ ksi}\sqrt{\text{in}}$ and a crack length of 1.5 inches.

Electrochemical treatment was applied to specimen D at the 40,000th cycle at $\Delta K = 44 \text{ ksi}\sqrt{\text{in}}$ and arrested the fatigue crack for 9,000 cycles. This specimen did not fail after 52,000 cycles. The last measurement indicated the crack length and the ΔK values of 1.74 inches and $60 \text{ ksi}\sqrt{\text{in}}$ respectively. The slope of the trend line of specimen D is lower

than that of specimen C. The difference in slopes may have been caused by the crack arrest period in treated specimen D. The fatigue crack in treated specimen D grew 0.24 inches longer than that of the non-treated specimen C before failure. Taking into account the similarity of the crack growth rates of specimens C and D before treatment and assuming the similarity of material fracture toughness of those specimens it appears that specimen D would be expected to fail within 1,800 cycles after the point of treatment. Instead the failure of specimen D did not occur after 10,200 cycles. Thus it appears that the fatigue life of the specimen D could be increased by 10,200 cycles or approximately 20%. However this fatigue life difference could also be observed due to the normal scatter of fatigue data.

For some specimens electrochemical treatment was applied on more than one occasion. Figure 52 shows fatigue crack propagation in specimen E before and after electrochemical treatment. The treatment was applied on two occasions.

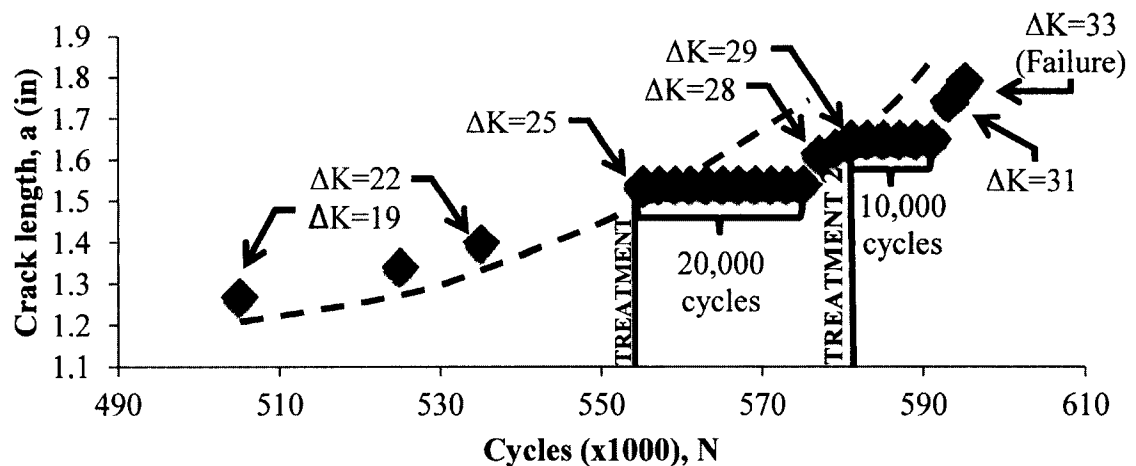


Figure 52. Fatigue crack propagation in specimen E before and after electrochemical treatment. Dashed lines represent projected behavior of a fatigue crack without electrochemical treatment based on the Paris Law.

Similarly to the fatigue crack in specimen D the crack in specimen E was continuously growing before treatment with the propagation rates reasonably characterized by the Paris Law. The crack was treated on the first occasion after 555,000 cycles when ΔK was equal to $25 \text{ ksi}\sqrt{\text{in}}$. The crack mouth opening (which was later converted to crack length using compliance methodology provided by the ASTM E399 Standard) was measured after every 2,000 cycles (after each treatment) in order to estimate the duration of treatment effect with some accuracy. After the first treatment no crack propagation was observed for 20,000 cycles. The crack resumed its propagation after that period with a rate of $\sim 1.75 \times 10^{-5}$ inches/cycle which was comparable to the Paris Law approximation ($\sim 9 \times 10^{-6}$ inches/cycle). The second treatment was applied after 581,000 cycles when ΔK was equal to $29 \text{ ksi}\sqrt{\text{in}}$. No crack propagation was observed for 10,000 cycles after the second treatment. Crack propagation was again noted at the 593,000th cycle. The crack propagation rate after the second treatment was 2.5×10^{-5} inches/cycle and was similar to the Paris Law approximation. Based on the Paris Law projection if the first treatment had not been applied the crack would have grown to 1.68 inches in 20,000 cycles instead of being held to 1.55 inches in length. It is interesting to note that the treatment yielded a longer crack re-initiation life when applied at a lower ΔK level. Based on these observations it appears that this type of treatment may be applied more than once in the life of a propagating crack and yield significant life extension following each application. Subsequent electrochemical treatments can be applied as a regular maintenance practice that can be designed to extend fatigue crack propagation life indefinitely.

Figure 53 demonstrates the history of the fatigue crack growth in specimen H.

The cycling of that specimen started at $\Delta K = 11 \text{ ksi}\sqrt{\text{in}}$ which was lower than that of the previously described specimens. That resulted in a longer fatigue life (1,165,000 cycles).

Crack propagation was measured using the CMOD method described in Section 3.1.

From Figure 53 it can be noted that the fatigue crack was continuously growing before treatment.

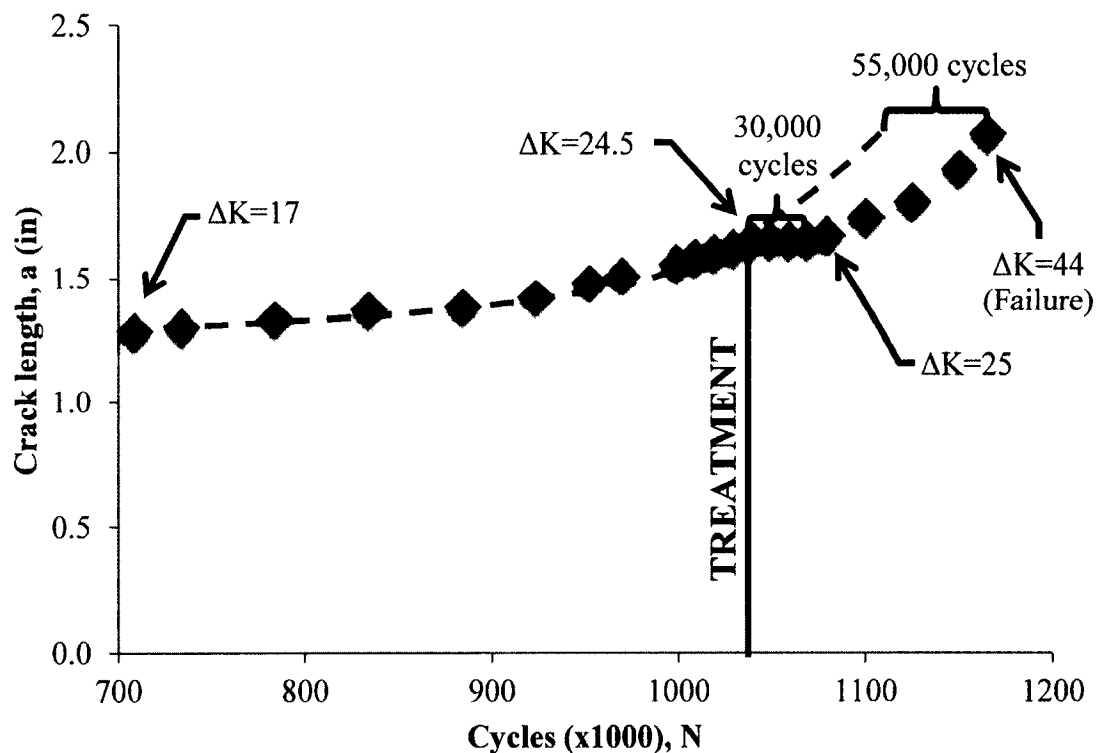


Figure 53. Fatigue crack propagation in specimen H before and after electrochemical treatment. ΔK units - $\text{ksi}\sqrt{\text{in}}$. Dashed lines represent projected behavior of the fatigue crack without electrochemical treatment.

As observed in other cases the projection of the crack propagation based on the Paris Law was very close to the actual data points before treatment. The crack propagation rate before treatment was well characterized by the Paris Law.

Electrochemical treatment was applied after the 1,040,000th cycle when ΔK was equal to 24.5 ksi $\sqrt{\text{in}}$. According to the Paris Law (if not arrested) the crack would have been projected to achieve 1.75 inches in length within 30,000 cycles. Instead the treatment only permitted a crack of 1.65 inches to be achieved by that point. According to the Paris Law projection shown in Figure 53 the failure of the specimen would be projected to occur 55,000 cycles earlier than the actual failure. The lower crack growth rate (da/dN) shortly after treatment resulted in an additional 25,000 cycles of fatigue life extension which followed 30,000 cycles of crack arrest. It was clearly observed that electrochemical treatment arrested fatigue crack propagation for 30,000 cycles and extended the fatigue life of specimen H for additional 25,000 cycles for a total apparent benefit of 55,000 added cycles. After the arrest period the crack resumed its propagation at an average rate of 2.2×10^{-6} inches/cycle. It was notable that shortly after re-initiation the crack growth rate (da/dN) was lower than the value predicted by the Paris Law (6×10^{-6} inches/cycle). Slower crack propagation after treatment may have been caused by the changed geometry of the crack and could possibly be characterized more accurately by a crack initiation model rather than the crack propagation model (the Paris Law). Slower crack propagation appeared to provide the 25,000 additional cycles noted here after crack arrest period of 30,000 cycles. Slower crack propagation (following treatment) was also noted in one other specimen (D). It was not noticed in other specimens. This type of observation was not possible in the other specimens because the observation frequency in these earlier cases was too low to capture this type of detail. The possibility of slowed crack propagation due to treatment requires additional exploration and analysis.

Based on the crack propagation data discussed in the preceding paragraphs it appears that the propagation of cracks before treatment was well characterized by the Paris Law. The behavior of the cracks after treatment was characterized by a period of apparent arrest and resumption of the propagation. In the two cases where it could be observed, the rate of crack propagation after treatment appeared to be converging back to the Paris Law approximation.

During this study the fatigue crack arrest period varied from 2,000 to 30,000 cycles and two data points of fatigue life extension were 10,200 cycles and 55,000 cycles. All the specimens were fatigue cycled with a sinusoidal wavelength at a frequency of 5Hz. The stress ratio was different for each specimen within a range of 0.26 - 0.66. The crack length to specimen width ratio (a/W) varied from 0.35 to 0.8. According to the literature the actual number of service load cycles in a typical gas pressure vessel is around 700-1,000 cycles per year, while the number of load cycles in a typical oil pipeline varies between 10^3 and 10^6 cycles [13,23]. Thus the periods of crack arrest and fatigue life extension observed in the current study may be translated into approximately 0.6-15 years of a typical oil pipeline operation or 2.4-66 years of a typical gas pressure vessel operation [13,23].

In the literature, other studies conducted on fatigue crack treatment techniques based on infiltration of cracks with epoxy resin researchers observed propagation life extension in the range of 2,900-12,600 cycles [125,183]. Song *et al.* achieved fatigue crack life extensions of up to 300,000 cycles by employing pressurized nitrogen for introducing alumina and silicon carbide reinforced epoxy resin into fatigue cracks in 5083-O aluminum alloy and AISI 4130 stainless steel specimens [125]. The study found

that the hardness of infiltrated materials was proportional to the fatigue retardation effect. Results obtained by Shin and Hsu on fatigue crack life extension using alumina reinforced epoxy resin contradicted with the results obtained by Song *et al.* [183]. In their study alumina reinforced epoxy brought smaller fatigue crack life extension compared to that of a regular epoxy resin. The current approach provided a life extension benefit of up to 55,000 cycles as compared to the best case in the literature of 300,000 cycles. The current approach appears to provide benefits that are within an order of magnitude of the best reported achievement but produces these results using an approach that can be field applied more easily since no gas pressure would be required and the cracks do not need to be free of moisture.

4.2 Re-initiation of Treated Fatigue Cracks

Figure 54 contains a bar-chart showing the average number of cycles that were required to initiate a fatigue crack from a V-shaped starter notch as compared to re-initiating fatigue crack propagation after an electrochemical treatment.

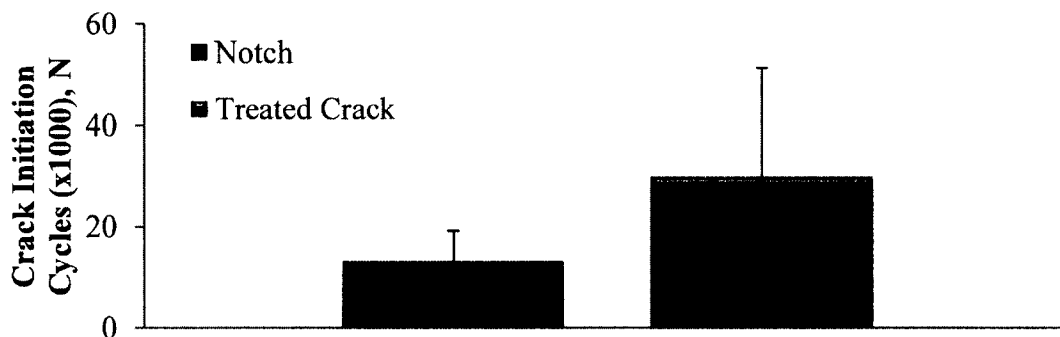


Figure 54. The average number of cycles required to initiate a fatigue crack from a V-notch as compared to re-initiating a fatigue crack after electrochemical treatment (Average of 3 data points for the notch case and 4 data points for the treated crack case. All data points were recorded at an average $\Delta K = 26 \text{ ksi}\sqrt{\text{in}} \pm 4 \text{ ksi}\sqrt{\text{in}}$).

From Figure 54 it was observed that on average 13 thousand cycles were required to initiate a fatigue crack (≥ 2 mm long) from a starter notch and 30 thousand cycles were required to re-initiate a fatigue crack after electrochemical treatment at an average of $\Delta K = 26 \text{ ksi}\sqrt{\text{in}} \pm 4 \text{ ksi}\sqrt{\text{in}}$. These observations tend to indicate that treated fatigue cracks may seem to behave as if they were untreated notches. In general, crack initiation in notches is well characterized using a strain life analysis as described in Section 2.1.3. The following section explores the viability of using a strain life approach in characterizing the fatigue behavior observed in Figure 54.

Based on an elastic-plastic strain-life analysis using a combination of Eqs. (1), (6) and (7) the calculation of crack initiation life from the ASTM E399 compact tension V-shaped notch used in this study was performed. Fatigue properties of ASTM A36 steel were found in the literature [41]. These values are shown in Table 2 (see Section 2.1.3). The values of the remote elastic strain amplitude were obtained from a finite element analysis described later in this chapter. The steps of the strain life analysis for crack initiation within the notch of the specimen are listed below:

1. Determination of the remote stress range ($\Delta S = S_{max} - S_{min}$) from the FEA (Section 4.5).
2. Estimation of the local stress at the notch root using Eq. (8). The stress concentration factor (K_t) was also obtained from the FEA (Section 4.5). The fatigue strength coefficient (K') and the fatigue strain hardening exponent (n') were obtained from the literature (see Table 2 in Section 2.1.3) [41].
3. Solving Eq. (7) for the local strain amplitude ($\Delta \epsilon/2$).
4. Calculating the number of reversals to failure ($2N_f$) using the Morrow's model (Eq. (1)),

$$\text{where } \sigma_m = \frac{\Delta \sigma}{2}.$$

An example calculation of $2N_f$ for specimen E is shown below.

Example of $2N_f$ calculation for specimen E with a V-shaped starter notch.

1. The maximum and the minimum load (P_{max} , P_{min}) applied during cycling were 6.72 kips and 3.45 kips respectively. The remote stress range ($\Delta S = S_{max} - S_{min}$) was obtained from the FEA:

$$\Delta S = 13.59 \text{ ksi} - 6.98 \text{ ksi} = 6.61 \text{ ksi}$$

2. The local stress at the notch root was calculated using Eq. (8) by iteration. The value of $K_t = \sigma_{max}/\sigma_{nom}$ was found to be equal to 15.8 (from the FEA). The fatigue properties of ASTM A36 steel were found in the literature and are shown in Table 2 in Section 2.1.3 [41]. All known values were inserted in Eq. (8) and it was solved for $\Delta\sigma$:

$$\Delta\sigma = \left\{ E \left[\frac{(K_t \Delta S)^2}{E} - 2 \left(\frac{(\Delta\sigma)^{\frac{n'+1}{n'}}}{(2K')^{1/n'}} \right) \right] \right\}^{1/2}$$

Inserting known and obtained values yields the following:

$$\Delta\sigma = \left\{ 27500 \text{ ksi} \left[\frac{(15.8 \times 6.6121 \text{ ksi})^2}{27500 \text{ ksi}} - 2 \left(\frac{(\Delta\sigma)^{\frac{0.249+1}{0.249}}}{(2 \times 159 \text{ ksi})^{1/0.249}} \right) \right] \right\}^{1/2}$$

$$\Delta\sigma = 66 \text{ ksi}$$

The mean stress is equal to a half of the true stress range:

$$\sigma_m = \frac{\Delta\sigma}{2} = 33 \text{ ksi}$$

3. The local strain amplitude ($\Delta\varepsilon/2$) was calculated by inserting all known values into the cyclic stress-strain curve Eq. (7):

$$\frac{\Delta\varepsilon}{2} = \frac{\Delta\sigma}{2E} + \left(\frac{\Delta\sigma}{2K'}\right)^{1/n'}$$

Inserting known values of E , K' and n' and the value of $\Delta\sigma$ obtained in step 2 yields the following:

$$\frac{\Delta\varepsilon}{2} = \frac{66 \text{ ksi}}{2 \times 27500 \text{ ksi}} + \left(\frac{66 \text{ ksi}}{2 \times 159 \text{ ksi}}\right)^{1/0.249} = 0.003$$

4. The number of reversals to failure ($2N_f$) was calculated by iteration using Eq. (1):

$$\frac{\Delta\varepsilon}{2} = \frac{\sigma_f' - \sigma_m}{E} (2N_f)^b + \varepsilon_f' (2N_f)^c$$

Inserting known and obtained values to the Morrow's strain life expression (Eq. (1)) yields the following:

$$0.003 = \frac{147 \text{ ksi} - 33 \text{ ksi}}{27500 \text{ ksi}} (2N_f)^{-0.132} + 0.271 (2N_f)^{-0.451}$$

$$2N_f = 3,801 \text{ reversals}$$

The results of the crack initiation analysis are shown in Figure 55.

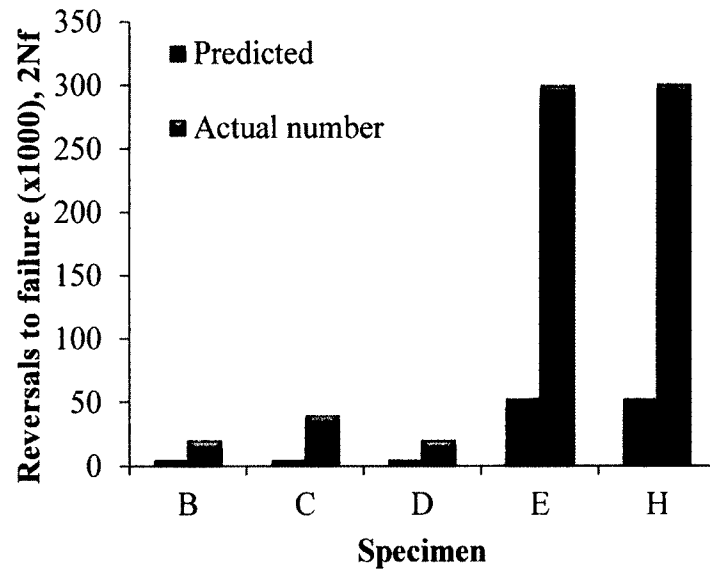


Figure 55. Comparison between the predicted and the actual numbers of reversals to failure (crack initiation) of ASTM E399 CT V-shaped starter notches. The prediction was achieved using a strain life analysis involving Eqs. (1, 7, 8). An example calculation is shown in current section.

From Figure 55 it was observed that the fatigue life prediction based on the true elastic-plastic strain analysis provided a reasonable approximation when taking into account the typically large scatter (up to a factor of ± 20 on life) that is generally associated with fatigue data [178,179]. Most of the predicted fatigue life values were a factor of approximately 5-6 times less than the actual test results; the maximum difference was of a factor of 10.5. The correlation between the predicted and the actual fatigue life data in a log-log plot is shown in Figure 56.

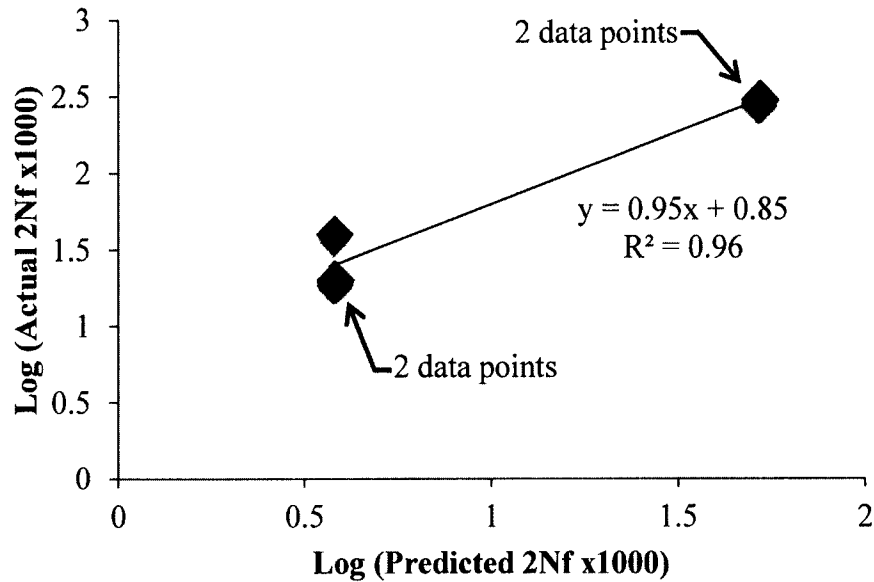


Figure 56. The relationship between the predicted and the actual values of reversals to failure (crack initiation) of starter V-shaped notches. Note that two of the five data points in this figure are obscured from view due to their close proximity to other data.

The coefficient of determination (R^2) of 0.96 for the 5 data points indicates a 95% confidence in the reproducibility of these results [184]. As noted earlier, the prediction correlates well while it under-predicts the true crack initiation life of the notch by approximately a factor of five – six on life.

As discussed in the beginning of this section it was observed that the treated fatigue cracks were similar to the ASTM E399 CT V-shaped notches in terms of the number of cycles required for fatigue (re-) initiation (see Figure 54). The fatigue live prediction based on the true elastic-plastic strain analysis was also performed for the treated fatigue cracks. In this analysis the limiting assumption was that the fatigue cracks appeared to behave like V-shaped notches after treatment. All treated cracks were assumed to be packed with nickel over 10% of their lengths. The steps of this analysis were similar to that of the notch case. An example calculation is presented below.

Example of $2N_f$ calculation for specimen E with electrochemically treated fatigue crack.

1. The maximum and the minimum load (P_{max} , P_{min}) applied during cycling were 6.72 kips and 3.45 kips respectively. The remote stress range ($\Delta S = S_{max} - S_{min}$) was obtained from the FEA of a treated crack (Section 4.5). The crack packing percentage was assumed to be 10%,

$$\Delta S = 38.07 \text{ ksi} - 19.55 \text{ ksi} = 18.52 \text{ ksi}$$

2. The local stress at the virtual notch root (this was actually a treated crack tip that was presumably behaving as if it were a notch) was calculated using Eq. (8) by iteration. The value of $K_t = \sigma_{max}/\sigma_{nom}$ used for calculation was 15.8 as for the notch case since the fatigue crack was assumed to appear like a notch after treatment. The fatigue properties of ASTM A36 (shown in Table 2) were used here again (even though Nickel properties may have provided some influence). All known values were inserted in Eq. (8) and it was solved for $\Delta\sigma$ by iteration:

$$\Delta\sigma = \left\{ E \left[\frac{(K_t \Delta S)^2}{E} - 2 \left(\frac{(\Delta\sigma)^{\frac{n'+1}{n'}}}{(2K')^{1/n'}} \right) \right] \right\}^{1/2}$$

Inserting known and obtained values yields the following:

$$\Delta\sigma = \left\{ 27500 \text{ ksi} \left[\frac{(15.8 \times 18.52 \text{ ksi})^2}{27500 \text{ ksi}} - 2 \left(\frac{(\Delta\sigma)^{\frac{0.249+1}{0.249}}}{(2 \times 159 \text{ ksi})^{1/0.249}} \right) \right] \right\}^{1/2}$$

$$\Delta\sigma = 107.03 \text{ ksi}$$

Mean stress is equal to a half of the true stress range:

$$\sigma_m = \frac{\Delta\sigma}{2} = 53.58 \text{ ksi}$$

3. The local strain amplitude ($\Delta\varepsilon/2$) was calculated by inserting all known values into Eq. (7):

$$\frac{\Delta\varepsilon}{2} = \frac{\Delta\sigma}{2E} + \left(\frac{\Delta\sigma}{2K'}\right)^{1/n'}$$

Inserting known values of E , K' and n' and the value of $\Delta\sigma$ obtained in step 2 yields the following:

$$\frac{\Delta\varepsilon}{2} = \frac{107.03 \text{ ksi}}{2 \times 27500 \text{ ksi}} + \left(\frac{107.03 \text{ ksi}}{2 \times 159 \text{ ksi}}\right)^{1/0.249} = 0.0146$$

4. The number of reversals to failure ($2N_f$) was calculated by iteration using Eq. (1):

$$\frac{\Delta\varepsilon}{2} = \frac{\sigma_f' - \sigma_m}{E} (2N_f)^b + \varepsilon_f' (2N_f)^c$$

Inserting known and obtained values into Morrow's strain life equation (Eq. (1)):

$$0.0146 = \frac{147 \text{ ksi} - 53.58 \text{ ksi}}{27500 \text{ ksi}} (2N_f)^{-0.132} + 0.271 (2N_f)^{-0.451}$$

$$2N_f = 819 \text{ reversals}$$

The relationship between the predicted and the actual data is shown in Figure 57.

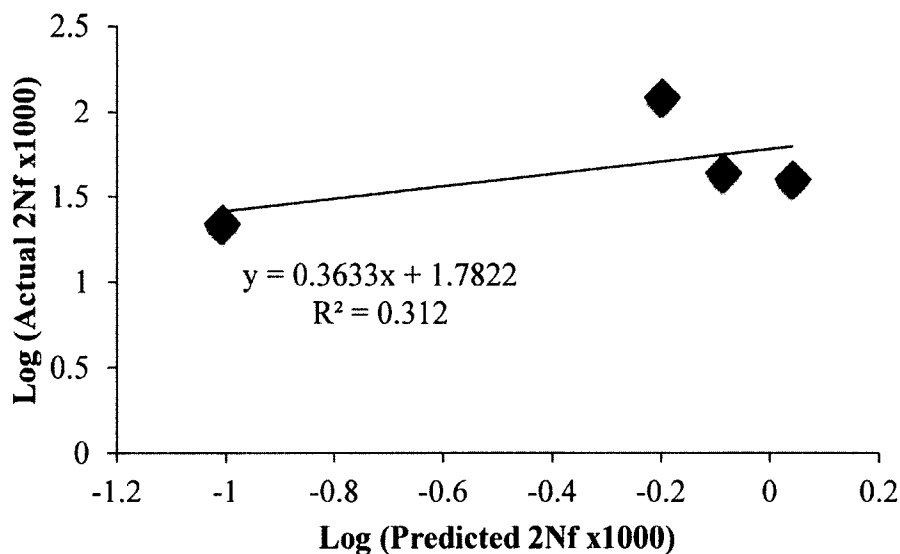


Figure 57. The relationship between the predicted and the actual values of reversals to failure (crack initiation) of electrochemically treated fatigue cracks. The prediction is based on a strain life analysis.

From Figure 57 it can be observed that the true elastic-plastic strain-life analysis did not provide a good approximation for the case of the treated fatigue crack. The actual number was under-predicted by factors ranging from 36 to 224. On average the under prediction was by a factor of 130. The large difference between the values of the predicted and the actual fatigue lives may be influenced by the changed material properties of the electrochemically treated cracks (fatigue cracks were packed with nickel), variation of the nickel deposit quality and thickness, and its distribution inside the cracks. A more accurate strain-life fatigue modeling approach requires a number of empirical constants for nickel that were not available for this study or found in the literature. Closer agreement between the observed and the predicted fatigue crack initiation life in electrochemically treated specimens may be possible using the strain-life fatigue properties of nickel. In future work it is also conceivable that a model of the

nickel distribution inside treated fatigue cracks may be developed in order to obtain more accurate strain values from a finite element analysis. Based on the observations described above it appears that the conventional elastic-plastic strain life analysis may not be suitable for achieving a reasonable re-initiation life of electrochemically treated fatigue cracks without better understanding of the deposited nickel distribution and its strain life fatigue properties. In the next Section another approach for predicting post-treatment fatigue based on a crack propagation approach is explored.

A relationship between the period of crack arrest and the stress intensity factor range (ΔK) applied during post-treatment cycling was observed (see Figures 58 and 59).

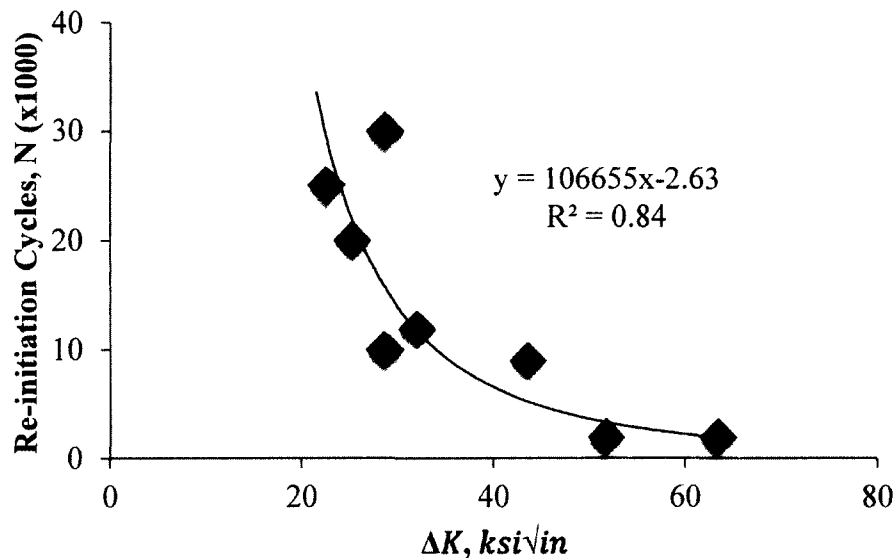


Figure 58. Relationship between fatigue crack arrest life (number of cycles to re-initiate a fatigue crack after treatment) and stress intensity factor range (ΔK) applied during post-treatment cycling.

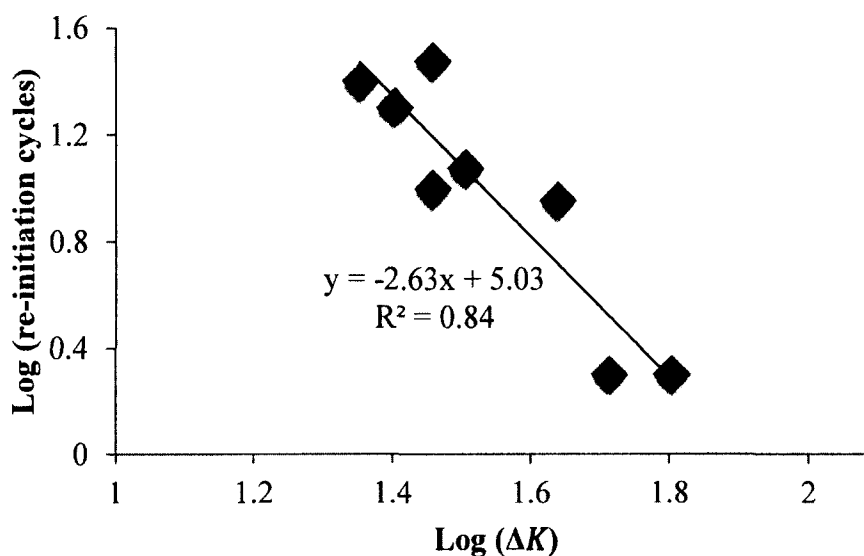


Figure 59. Log-log plot of the relationship between fatigue crack arrest life (number of cycles to re-initiate a fatigue crack after treatment) and theoretical stress intensity factor range (ΔK) applied during post-treatment cycling.

From Figure 58 it can be observed that the fatigue crack arrest time varied from 2,000 to 30,000 cycles. Electrochemical treatment conditions and procedures were the same for all treated specimens and thus it can be noted that there is a correlation between the fatigue crack arrest period and the stress intensity factor range (ΔK) applied for post-treatment cycling. Figure 58 can be used to predict the effect of electrochemical treatment in terms of number of cycles for fatigue crack to re-initiate. The coefficient of determination (R^2) was equal to 84% leading to the correlation coefficient equal to 91.6%. This corresponds to a 99% confidence level for the reproducibility of the findings. This can be interpreted as good data correlation taking into account the typically large scatter of fatigue data [178,179]. The power law relationship presented above exhibits good correlation but it assumes the presence of an “infinitely sharp crack” that is unaltered. An adjusted version of ΔK that takes into account crack length and local stress

reductions due to electrochemical treatment is described in Section 4.5. This modified model also incorporates observations from the treated crack microscopy that is presented in the Section 4.3.

4.3 Microscopic Analysis

Optical microscopy allowed determination of the dimensions of starter notches and fatigue cracks. Figure 60 shows an optical microscope image of a starter notch in an ASTM E399 specimen machined for this study.

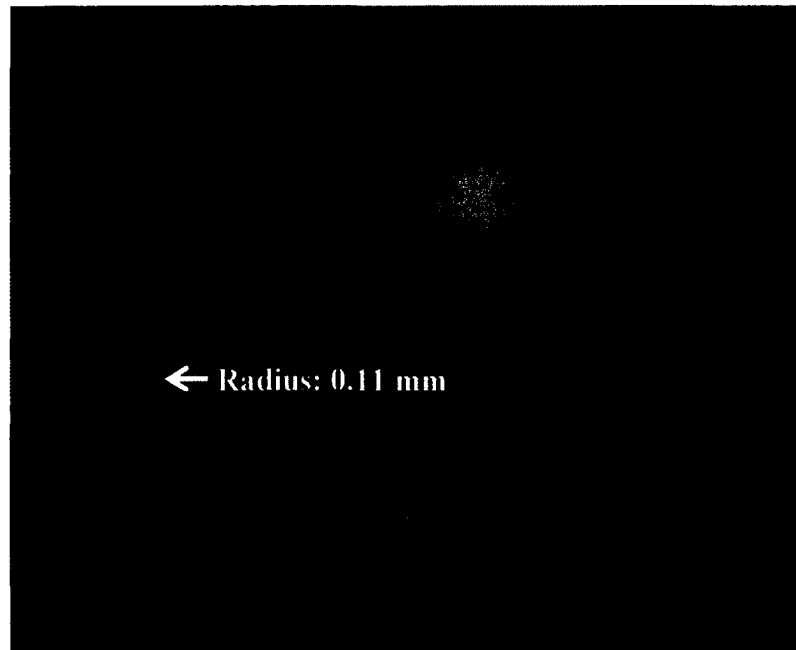


Figure 60. Starter notch radius of an ASTM E399 compact-tension specimen.

From Figure 60 the radius of a starter notch established within an ASTM E399 CT specimen used in this study was determined. It was 0.11 mm or 0.0043 inches. In general, the smaller the notch radius the shorter the crack initiation life is. The notch

radius has been found to be a primary influence on such factors as stress concentration, stress intensity, and the fracture toughness of a component [185,186]. According to Eq. (3) (see Section 2.1.3) the stress concentration factor of a typical starter notch used in this study was equal to approximately 16.

Scanning electron microscopy (SEM) was employed to capture an image of the tip of an electrochemically treated fatigue crack as shown in Figure 61. This specimen was cut from a treated ASTM E399 Compact Tension specimen (as shown in Figure 36), mounted in epoxy and polished prior to imaging. The specimen preparation procedure is described in detail in Section 3.4.

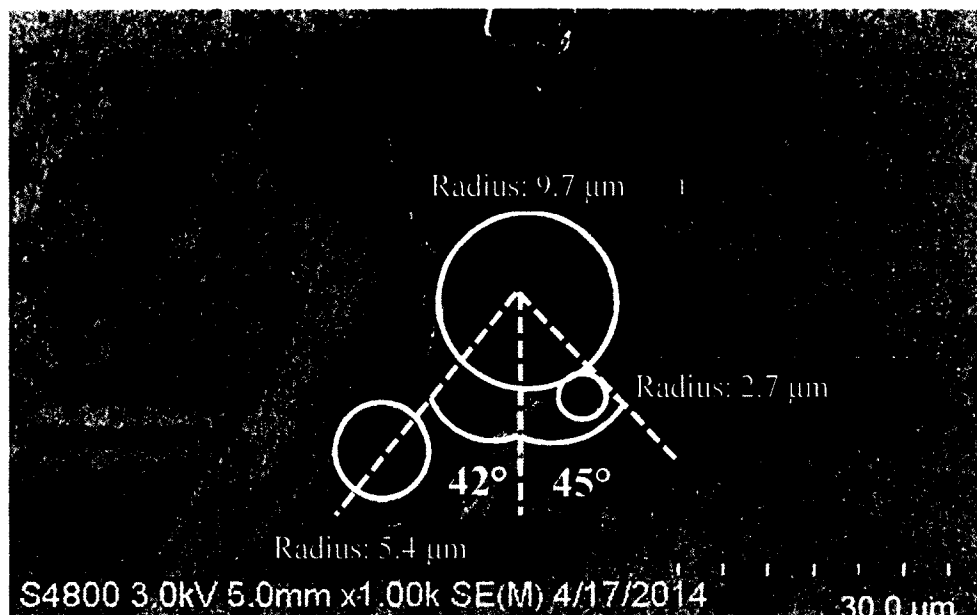


Figure 61. SEM image of the fatigue crack tip (Specimen G) following nickel plating treatment.

From Figure 61 it was observed that a fatigue crack tip consisted of two small notches with 2.7 μm and 5.4 μm radii located at 42° and 45° angles from the fatigue

crack. Similar images of fatigue crack tips can be observed in the literature [187-190]. According to Laird these notches may account for the orientation concentration of slip zones and the formation of striations associated with crack propagation [66]. The plastic-blunting mechanism of crack extension proposed by Laird is shown in Figure 11 in Section 2.1.6. The radius of the fatigue crack tip determined from Figure 61 can be used to calculate the stress concentration factor (K_{tg}). Using Eq. (3) K_{tg} was found to be equal to 135.

Another treated fatigue crack was examined with an optical microscope in order to determine nickel deposit distribution as described in Section 3.5. Figure 62 contains an optical microscope image of an electrochemically treated fatigue crack. The specimen was imaged under a static load of 6 kip immediately after electrochemical treatment without polishing or any other preparation procedures. A relatively bright layer was observed along the left face of the crack. It was not evenly distributed and its thickness varied along the crack length. Bright particles were also observed inside the crack. In addition, a few bright areas were also present on the right side of the crack. The following Section examines how these bright areas compare to theoretical expectations for nickel deposition.

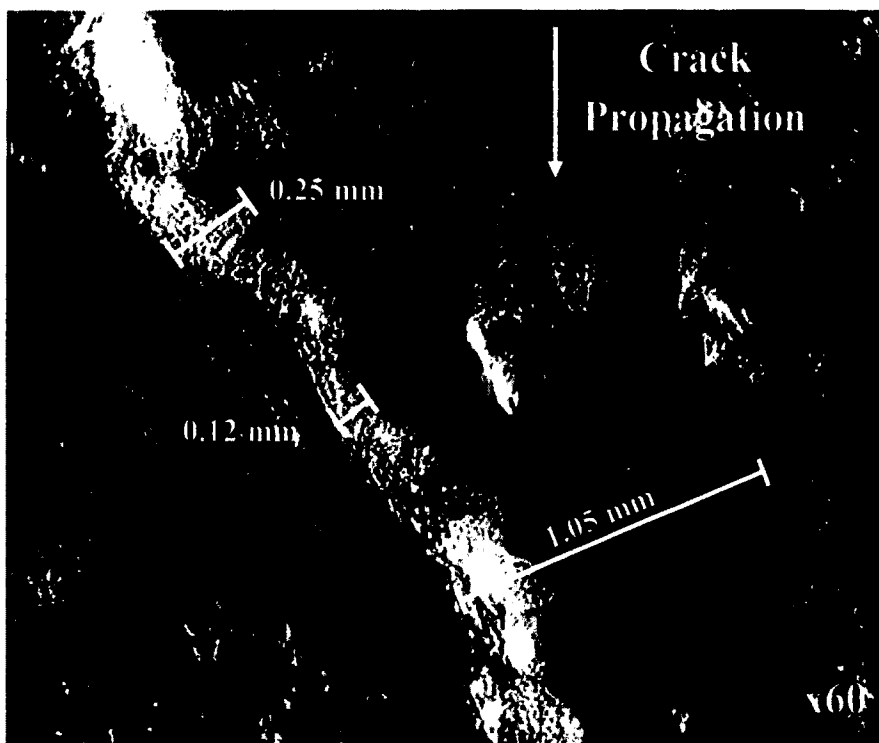


Figure 62. Optical microscope image of electrochemically treated fatigue crack.

As noted, the bright layer along the left side of the crack appeared to be nickel that was deposited into the crack during electrochemical treatment. According to Faraday's Law (Eq. (22)) the thickness of the nickel deposit formed during electrochemical treatment was expected to be 0.18 mm. By comparison, the apparent deposit shown along the left side of the fatigue crack ranged from 0.12 to 0.25 mm. From these observations it appeared that the bright layer along the left side of the crack was nickel since it tended to approximately correlate with the theoretical thickness of nickel that can be electroplated under conditions applied in this study.

Figure 63 shows an optical image of a portion of a fatigue crack that was subjected to treatment. As noted in an earlier example the treatment did not appear to exhibit a uniform morphology along the length of the crack. Constituents inside the crack

formed a clump with an arc-shaped edge (See Figure 64). The thickness of this formation (0.23 mm) was similar to that of the bright layer observed in Figure 58 (0.12 - 0.25 mm). Beyond this location, the crack did not appear to be completely packed with nickel. These observations indicated that electrochemical treatment could possibly cause wedging ahead of a fatigue crack tip as opposed to, or in addition to, completely packing it with new material.

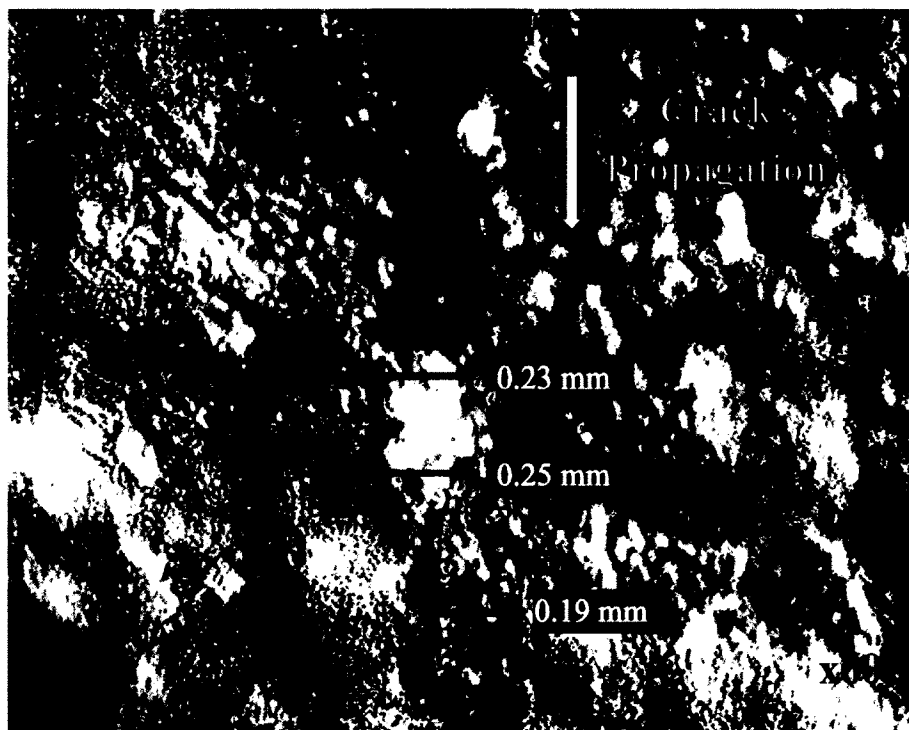


Figure 63. Optical microscope image of a portion of a fatigue crack packed with plating bath constituents (presumably with nickel).

The crack packing formation presented in Figure 63 has an arc-shaped top side that creates two small notches one at each crack surface boundary as shown in Figure 64.

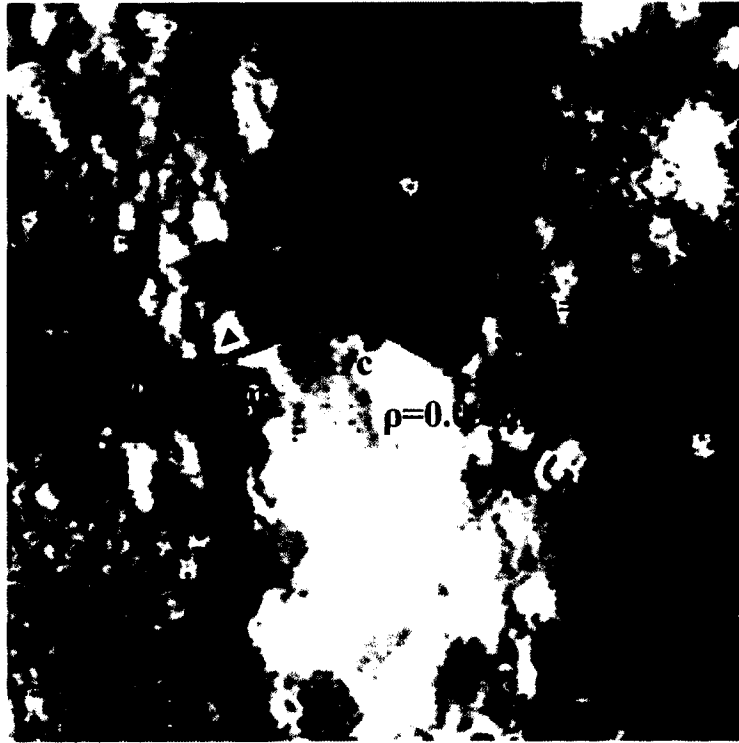


Figure 64. Magnified optical microscope image extracted from Figure 63. This image shows deposit formation within the crack, the arc of the deposit and the radii at each crack surface.

The stress concentration factors of these notches can be estimated with Eq. (3) by taking into account that the length of the crack before treatment was 1.76 inches and it was reduced to 1.55 inches by 12% crack packing with nickel. The stress concentration factors (K_{tg}) of these notches are 47 (right notch) and 53 (left notch). The finite element solution which is presented further in this chapter resulted in $K_{tg} = 8$ for a 1.4 inch long crack with a nickel wedge located 5 mm away from the crack tip. This observation suggests that packing a fatigue crack with nickel may result in a significant reduction of the stress concentration factor, particularly from 135 to around 50 in one of the specimens used in this study. Reduction of the stress concentration factor provides a more even distribution of stresses and a potentially longer fatigue life. This may be one of the

factors leading to the phenomenon of longer crack re-initiation in electrochemically treated fatigue cracks as compared to crack initiation in starter notches as shown in Figure 64.

In addition to optical microscopy, scanning electron microscopy (SEM) was also employed for imaging electrochemically treated fatigue cracks. Figure 65 shows an SEM image of a fatigue crack plated with nickel. This image was taken using the specimen shown in Figure 61, 5 mm away from the crack tip. The crack seems to be loaded with some particles. In a later section energy-dispersive x-ray spectroscopy (EDS) was used to examine the composition of the crack packing material. During the spectroscopic analysis nickel was detected. Discussion of other EDS results is presented further in this chapter.



Figure 65. Scanning electron microscope image of an electrochemically treated fatigue crack within 5 mm of the crack tip.

SEM images were used to estimate the efficiency of the electroplating setup used in this study and to determine the deposit surface profile. The surface roughness and the distribution of electroplated nickel on a sand-blasted, rectangular, ASTM A36 steel specimen were analyzed. Figure 66 contains an SEM image of the electrolytic nickel layer removed from a specimen, mounted in epoxy, and polished prior to imaging.

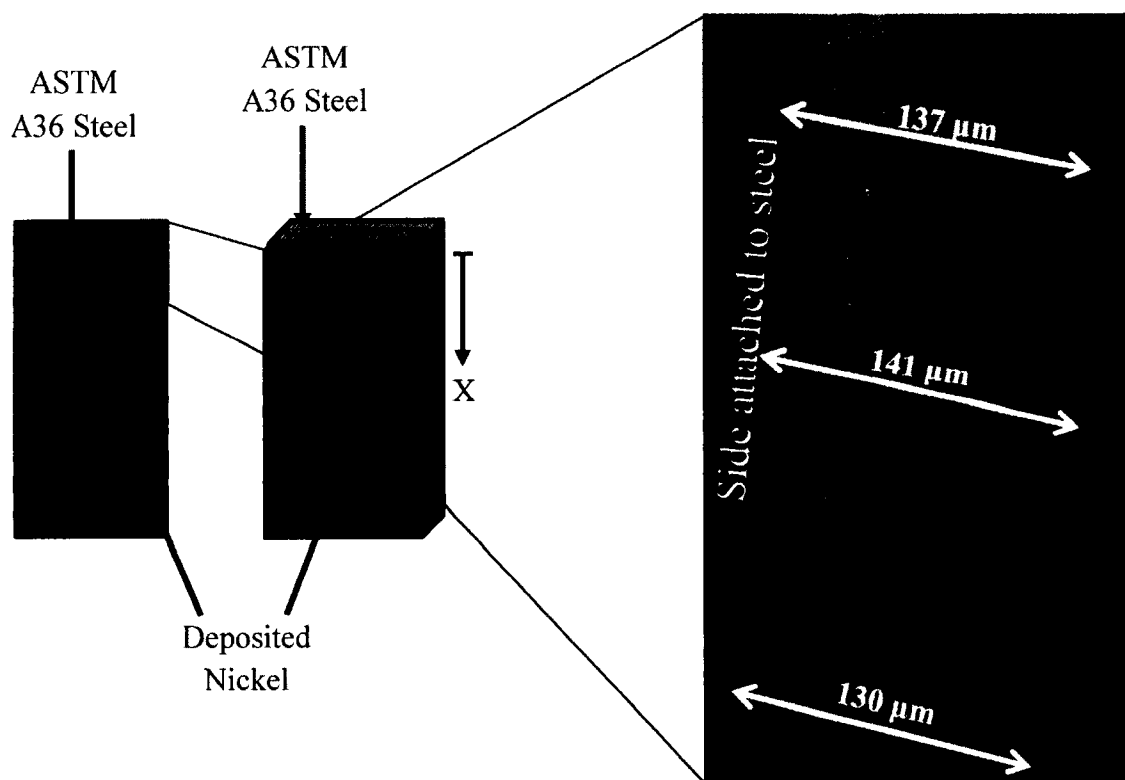


Figure 66. SEM image of the electrolytic nickel layer deposited onto an ASTM A36 steel specimen. Nickel was deposited using Watts' nickel plating bath for deposition time of 1 hr. The layer was manually removed from the specimen, mounted in epoxy and polished prior to imaging.

Figure 66 presents a layer of nickel formed by electroplating. Similar images were found in the literature [191,192]. The side that was previously attached to steel specimen appears to be more uniform due to sandblasting of the steel specimen prior to

electroplating. Black spots as well as asymmetric voids inside the nickel layer may be examples of micro-porosity. Porosity of the electroplated layer of nickel in this study could have been caused by impurities introduced into the plating bath solution. These may include chlorides, oxides, sulfur and organic impurities [147,193]. Porosity of electroplated material has been demonstrated to influence the corrosion resistance and fatigue life of the deposited layer [194,195]. Pores and voids inside the deposited material present stress concentrations and may encourage crack initiation. The defects observed on the right side along the deposit surface, due to their shape, could also lead to crack initiation, crevice corrosion and corrosion fatigue. It would be anticipated that a relatively low porosity in the nickel deposit could result in a better outcome for electrochemical treatment of fatigue cracks in terms of greater fatigue life extension and longer crack arrest time. Lower porosity should also improve corrosion resistance by lessening the potential for occluded cells as well as less opportunity for an aggressive environment to percolate through the network or pores.

In order to obtain the surface profile of the deposited nickel the thickness of the layer was measured in 52 different locations using SEM images. The results of the measurements are presented in Figure 67.

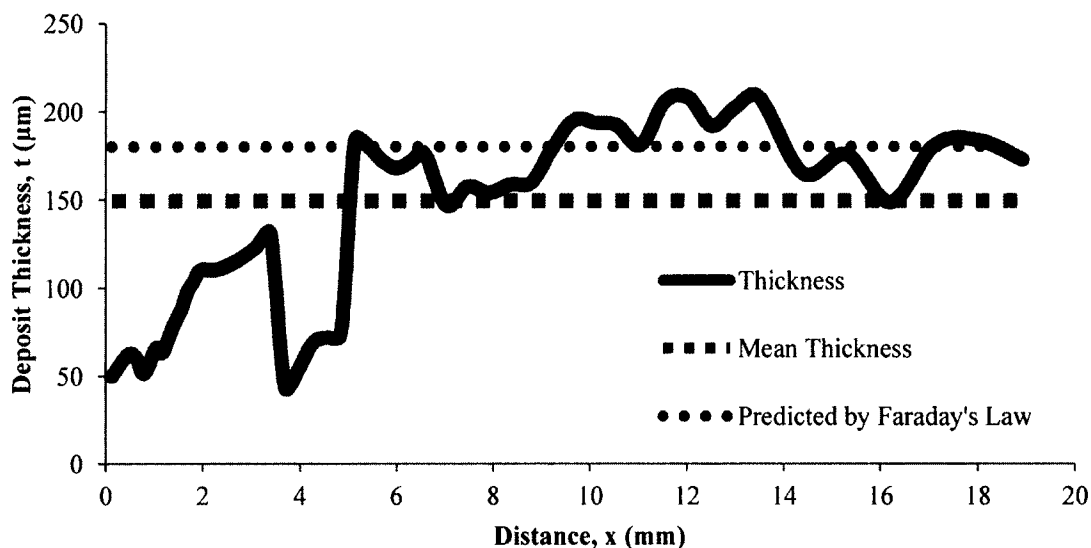


Figure 67. Thickness variation of a nickel layer electrodeposited onto ASTM A36 steel plate. The distance was measured from the specimen's edge closest to the top of the plating bath reservoir.

From Figure 67 it was observed that the thickness of the nickel layer varied from 44 μm to 208 μm . The mean thickness of the nickel layer was 153 μm . The standard deviation was 54 μm . The roughness of the profile (R_a) was calculated using Eq. (23) (see Section 2.2.3) and was equal to ~ 49 μm .

Faraday's Law of Electrolysis presented by Eq. (22) (see Section 2.2.3) was used for calculation of the theoretical thickness of a nickel layer that could be electrodeposited under the conditions used in this study (see Section 3.2). The dimensions of the substrate (ASTM A36 steel rectangular specimen) were 0.7 inches (1.78 cm) wide and 0.75 inches (1.91 cm) long. The weight of the deposited nickel layer in this study was found to be equal to 1.09 gram. It was divided over the substrate's surface area (A) subjected to electrodeposition ($A = 2 \times 1.78 \text{ cm} \times 1.91 \text{ cm} = 6.77 \text{ cm}^2$), and over the nickel density (8.9 gram/cm^3). These calculations resulted in an estimated nickel layer thickness equal

to ~180 μm . This profile is plotted in Figure 67 as a dashed line with circular markers. The efficiency of the plating setup ($\%F$) was estimated as a ratio between the mean thickness of the deposit obtained from the experimental results and the theoretical value estimated by Faraday's Law. $\%F$ in this case was equal to 85%. The layer of the deposited nickel whose profile is shown in Figure 67 was extracted from a corner region that was bordered by two edges. The literature generally contends that such edges are expected to have relatively thicker deposits than interior regions [147,158,196]. The present profile appears to contradict this tendency but this difference could possibly stem from the irregular electrode configuration used in this particular experiment.

Because of the nature of electroplating in general, obtaining a highly uniform distribution for a deposit may be difficult in practice. The uniformity of a deposit depends on the uniformity of the current distribution over the surface [158]. Current distribution usually depends on the shape and roughness of the surface of the substrate and its relative position with respect to the anode [196]. Edges and recesses on a surface often attract more current and this consequently results in thicker deposits at these locations [197].

For some applications of steel structures surface roughness is of high importance, for example for considering the friction of sliding components or for management of hydrodynamic drag. In this particular study, the surface roughness is of interest due to its effect on fatigue life [153-157,198-200]. One of the factors affecting the degree of fatigue life extension is the quality and uniformity of plated metal deposits. During the experimental procedures it was observed that the electroplating process often resulted in a build-up of nickel "clumps" around the edges of the specimens which could conceivably hinder the flow of metal ions into the crack.

Improved nickel deposit quality can be achieved by the application of sulfamate nickel plating bath solutions which were recently shown to be effective for engineering applications providing great wear and corrosion protection [201,202]. The surface roughness, the micro-porosity and the distribution of the nickel deposit may also be improved by employment of electroless nickel plating as was previously demonstrated in several studies [194,195,203,204]. This process achieves deposits through a dipping methodology. This may be difficult to apply deep within cracks and in areas where organic liquids need to be cleansed from the surface prior to plating.

4.4 Spectroscopic Analysis

Energy-dispersive X-ray spectroscopy (EDS) was employed for elemental analysis and chemical characterization of treated specimens. An SEM image of the surface of an electrochemically treated fatigue crack is shown in Figure 68. Table 8 contains elemental content data acquired from this specimen surface.

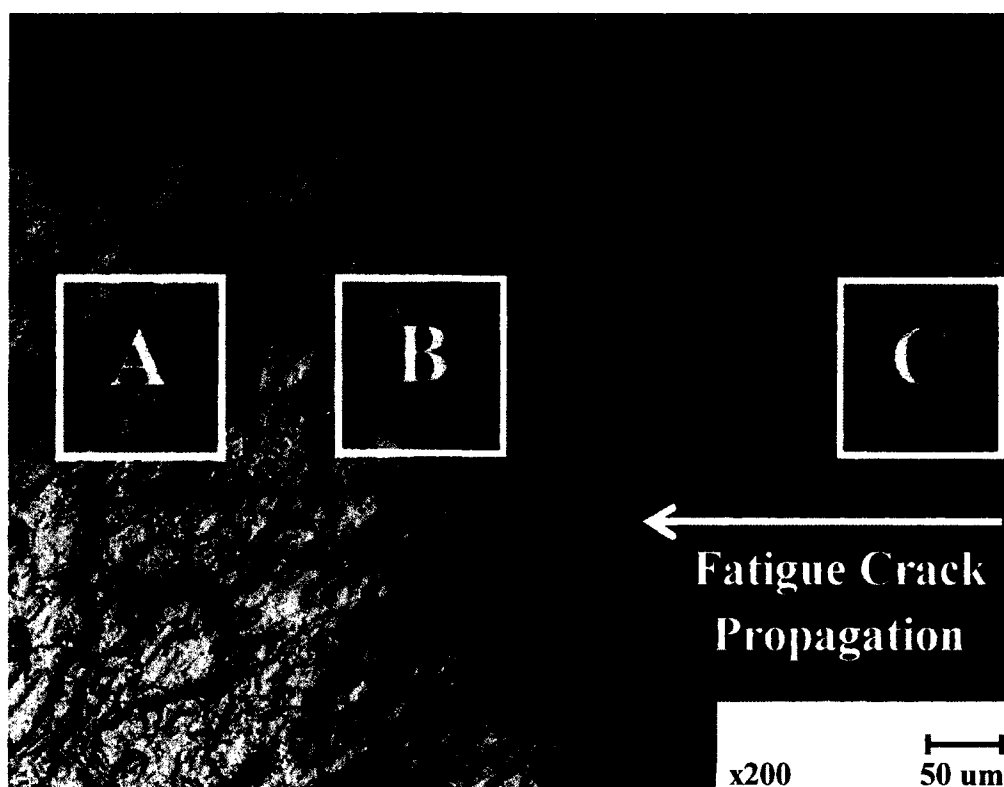


Figure 68. SEM image of electrochemically treated specimen fracture surface. The border between light and dark areas marks the tip of the fatigue crack.

Table 8. Elemental content (weight %) of electrochemically treated specimen

Chemical element	Area A	Area B	Area C
Iron (Fe)	92.7	91.2	81.1
Nickel (Ni)	5.5	7.6	15.4
Sulfur (S)	-	1.1	3.5

The surface of the specimen was not polished prior to imaging in order to preserve the original element content. Dark areas appear to represent the extent of the Watts' plating bath solution penetration into the treated the crack. The element content was measured at three locations in the vicinity of this boundary as marked on Figure 68. Location C was the most remote from the apparent crack tip within the plating bath zone.

Location B was on the apparent borderline of the plating bath treatment, and location A was ~250 μm away from the borderline in the apparently untreated region, B.

It was observed that the nickel and sulfur weight percentages declined from high values in the treated zone (within the crack) to lower values in the untreated zone in the direction of crack propagation. Sulfur was present in the Watt's plating bath solution and its limited presence on this surface appeared to indicate that the plating bath reached areas B and C. It was somewhat unexpected to find the presence of nickel in area A where the plating bath residue was not observed. It is conceivable that diffusion of nickel from area B could have permitted this transport into the area that was outside of the apparent plating bath zone.

Diffusion of nickel into the adjacent steel and diffusion of iron into the nickel deposit would be expected over time since nickel and iron are well known and established in various metal alloys. It is conceivable that mutual diffusion of these species could be beneficial. Galvanic corrosion induced by these metals is a concern for long term durability. The mutual diffusion indicated by these EDS results could eventually reduce the galvanic potential difference exhibited by these two metals which would tend to reduce the rate of corrosion over time. Based on these observations it appears that the treatment process would yield a galvanic corrosion potential that is lower than what may be anticipated by comparison of the two metals in a galvanic series table or in a simple galvanic corrosion measurement.

These observations raise some interesting durability considerations. The diffusion process mentioned earlier would not tend to reduce the compressive stress induced by the

initial nickel deposit. This bodes well for the long term performance of a treatment. This means that after treatment the crack closure would tend to continue providing a compressive stress that would be expected to limit the amount of water that could access the interface between the two metals in the vicinity of the crack tip. This also would tend to support effective long term performance of a given treatment.

In Figure 68 It was somewhat difficult to determine the location of the crack tip. For this reason an EDS analysis of a specimen containing an electrochemically treated fatigue crack with a clear location of the tip was also performed. An optical image of the specimen is shown in Figure 69. In the case the specimen was not broken to reveal the crack surface. The elemental content was measured at three locations (outside of the crack, inside the crack and inside the crack tip). Those locations are identified by black round markers placed in Figure 69.

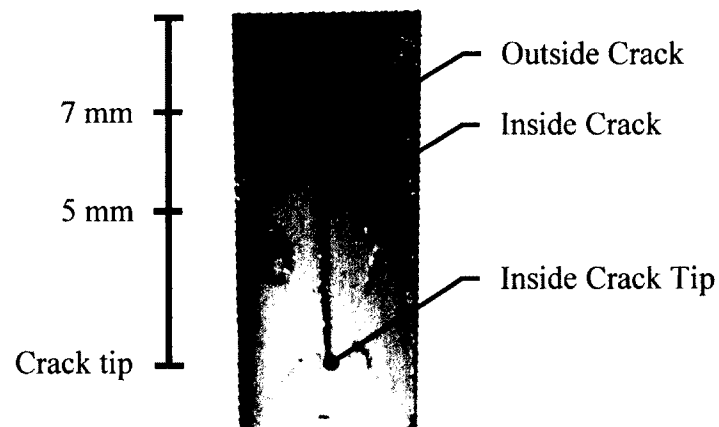


Figure 69. ASTM A36 steel specimen with an electrochemically treated fatigue crack viewed from the side. In this view the crack appears to be propagating down the page.

The presence of nickel was detected inside the crack, 5 mm away from the crack tip. Nickel was not detected outside the crack and just inside the crack tip. It is conceivable that the absence of nickel inside the crack tip may have been caused by some level of crack closure that could have occurred during electroplating since the crack was not fully opened during the treatment. This possibility is unlikely since the ΔK_{eff} in this case would have to be very small for crack closure to play a role in effecting transport to the crack tip. It is also possible that small air bubbles in the crack could have inhibited penetration of the plating bath solution prior to treatment. Another consideration is that the roughness of the crack could have provided a nonuniform electric field which could also cause the nickel distribution to be nonuniform.

Although the EDS was effective in confirming the deposition of nickel on crack surfaces it should be noted that the element content analysis had limitations in terms of the depth of the measurement. It provided measurement of the surface content (1-2 μm deep). Even though the specimens were relatively flat, the weight percentages obtained for the elements detected did not present highly accurate values that would be anticipated from polished surfaces. Thus the EDS can be considered somewhat qualitative in nature.

4.5 Finite Element Analysis

Finite element analysis was performed to serve as a comparison to the experimental and analytical results. In particular the analysis also examined the relative impact of filling the tip of the crack fully as opposed to creating a wedge just ahead of the crack since the microscopy showed both possibilities exist along a given crack. The FEA results were used earlier in this study for the analysis and modeling of crack re-initiation.

Initially the ASTM E399 CT- specimen with a fatigue notch subjected to a static load of 6 kips was modeled and analyzed. Figure 70 shows the normal stress distribution along X axis (σ_x) of the CT specimen.

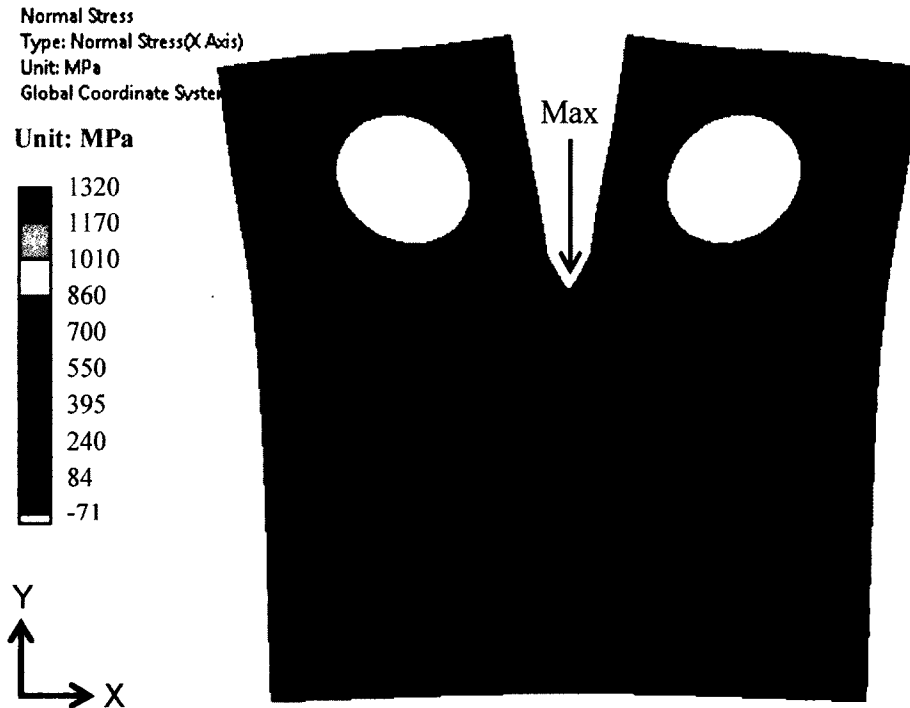


Figure 70. Normal stress distribution along X-axis (σ_x) in the ASTM E399 CT specimen with a V-shaped starter notch subjected to a static load of 6 kips. The maximum stress zone (red color) is very small and appears at the root of the notch.

From Figure 70 it was observed that the maximum stress (σ_{max}) was 1320 MPa (192 ksi) and it was located at the tip of the fatigue starter notch. The nominal stress (σ_{nom}) located away from the notch tip was equal to 84 MPa (12 ksi).

The stress concentration factor ($K_{Ig} = \sigma_{max}/\sigma_{nom}$) was determined to be equal to 15.8. The theoretical value of K_{Ig} calculated using Eq. (3) was 16. This suggests that a good correlation between the FEA model and analytical calculations was achieved.

A model of the CT specimen with a fatigue crack of 1.4 inches in length was studied using a dynamic transient analysis technique as described in Section 3.8. The analysis involved 3 time steps. At time step 1 the specimen was subjected to a static load of 6 kips. At step 2 nickel deposition was simulated by insertion of a nickel layer with length of 10%, 50% and 100% of the fatigue crack length as shown in Figure 71. At step 3 the static load was released. Figure 72 shows the normal stress distribution along the X-axis (σ_x) at each of the 3 steps of the analysis.

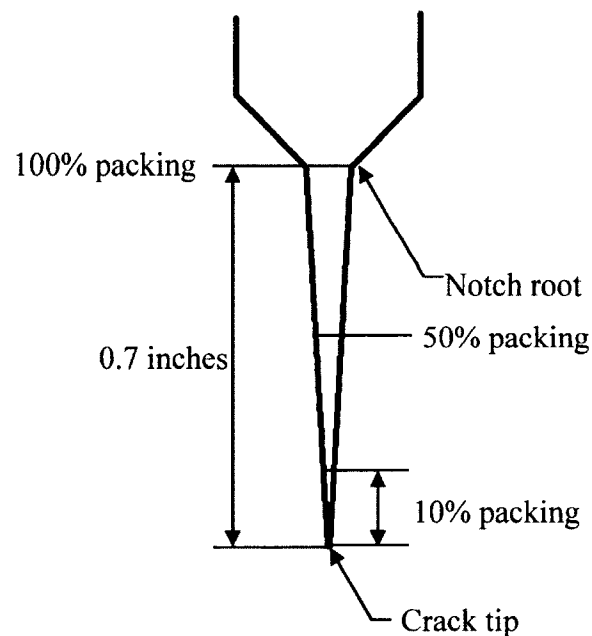
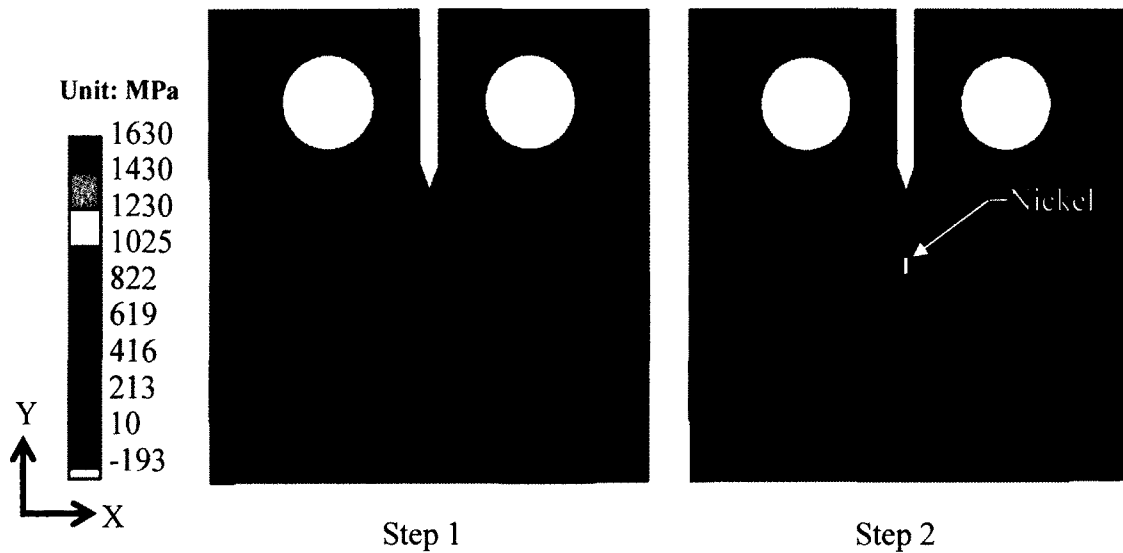


Figure 71. Crack packing schematic. The FEA analysis was conducted for 3 levels of crack packing, 10, 50, and 100% of the crack length.



CT-specimen with a fatigue crack subjected to a static loading of 6 kip.

A layer of nickel is inserted. 10% of the crack is filled with nickel. Specimen is still loaded to 6 kip.

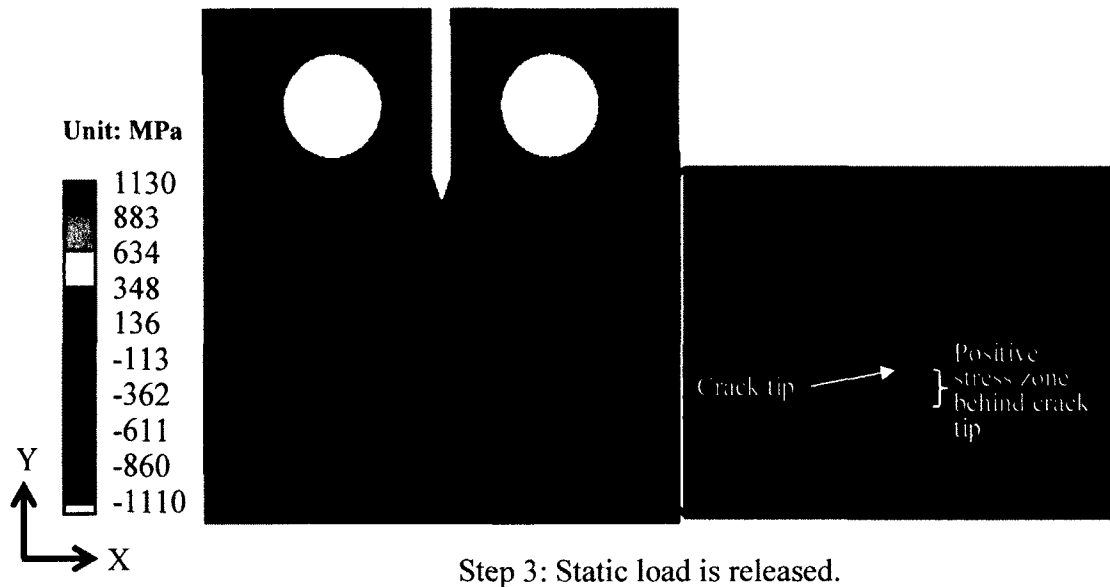


Figure 72. Normal stress distribution along X-axis (σ_x) in ASTM E399 compact tension (CT) specimen with a fatigue crack packed with a nickel layer extending 10% of the crack length, starting at the tip. Each image represents one step of the finite element analysis.

At step 1 the maximum normal stress along the X-axis was observed at the crack tip and was equal to 1630 MPa (237 ksi). The nominal stress was 10.3 MPa (1.5 ksi).

The ratio of the local stress maximum to the remote (nominal) stress in this case was found to be $K_{Ig} = 158$. By comparison, the K_{Ig} value of a typical fatigue crack (shown in the SEM image of Figure 61) was equal to 135 according to Eq. (3). The fatigue crack modeled in the FEA was 0.66 inches shorter than the fatigue crack shown in Figure 61, thus a lower K_{Ig} value was expected to result from the finite element analysis. A higher K_{Ig} value obtained from the FEA may be caused by the fact that the finite element analysis assumed a sharp crack and provided a purely elastic solution that ignored the stress reduction associated with crack tip radius affected by plasticity. Modeling a radius similar to that shown in Figure 61 could possibly bring these two K_{Ig} values closer in value. As expected, no change of stress values or distribution was observed after insertion of the nickel layer at step 2. At step 3 the static load was released and the stress distribution changed. The maximum stress was now observed just beyond the crack tip and was equal to 1130 MPa (164 ksi). The minimum stress was located at the packed crack tip and extending along the nickel layer. This stress was equal to -1110 MPa (-161 ksi). It makes sense from an equilibrium standpoint that compressive stresses forming within the packed crack would be balanced by tensile stresses just beyond the tip of the crack. The stress at the top of the nickel layer (new fatigue crack tip) was equal to -860 MPa (-124 ksi) and was under compression. The fatigue crack became packed with nickel and was under compression. Fatigue cracks are assumed not to grow under compression and thus crack packing and formation of compressive stresses at the crack tip would tend to result in fatigue crack arrest as observed during the experiments (Figures 50-53).

Another effect of the introduction of foreign objects onto fatigue crack surfaces is the potential for crack closure which was described in Section 2.1.10. Crack closure was

found to be responsible for crack growth retardation in numerous studies [93-95, 102, 110,112-114,122,124]. The majority of those studies were performed under plane stress conditions which would permit significant amounts of plasticity. Under these conditions, the crack closure phenomenon could play a significant role in fatigue crack growth retardation observed in those studies. This study was performed under plane strain conditions as dictated by the ASTM E399 Standard. Plasticity induced crack closure under plane strain conditions has generally been found to be insignificant so it is unlikely that it was responsible for the fatigue crack arrest behavior observed in this study [121,205].

The effect of the crack packing percentage was studied via the FEA with three different nickel layer models. Each model varied only by length along the crack. The lengths were as follows: 0.7 inch (100% packing of the crack length), 0.35 inch (50% packing of the crack length), and 0.07 inch (10% packing of the crack length). Each of these lengths was measured from the crack tip as shown in Figure 71. The results of this analysis are shown in Table 9.

Table 9. FEA model results for the maximum and minimum normal stresses developed along the X-axis of the crack in the ASTM E399 compact-tension specimen with a 0.7 inch long fatigue crack (measured from the notch root as shown in Figure 71). This model simulates uniform packing of a fatigue crack during electrochemical treatment by insertion of a layer of nickel.

Crack Packing	Max σ_x (MPa) Step 1	Max σ_x (MPa) Step 2	Max σ_x (MPa) Step 3	Min σ_x (MPa) Step 3
100%	1633	1633	1578	-516
50%	1633	1633	1330	-840
10%	1633	1633	1132	-1110

From the FEA it was observed that the highest tensile stress at step 1 and 2 remained the same and was located at the tip of the fatigue crack. At step 3 the static tensile load was released and the distribution of stresses changed. The maximum tensile stress was now located just beyond the old crack tip and a compressive stress developed in the vicinity of the “new” crack tip (top edge of the deposit) as shown in Figure 72. In comparing the three cases of crack packing (10%, 50% and 100%) it was observed that packing 10% of the fatigue crack resulted in the highest compressive stress in the vicinity of the new crack tip and the lowest tensile stress was developed just behind the initial crack tip.

The relatively high compressive stress in the 10% packing case can be explained by the load being distributed over a small area of nickel. The compressive stress at the crack tip in the case of 100% crack packing was the lowest result. This makes sense because the closure load was distributed over the largest area of nickel under consideration. In the 5th column of Table 9 the compressive stress drops from 516 MPa down to 1100 MPa while the percent of crack being packed decreases from 100% to 10%. This trend suggests that a higher percentage of crack packing would be expected to result in a lower compressive stress along the crack face. A higher percentage of crack packing would tend to reduce the stress intensity and the stress concentration factor at the crack tip and thus increasing the fatigue crack re-initiation life, assuming it re-initiates at the new crack tip. A similar conclusion was stated by Shin and Cai who developed a model for evaluation of fatigue crack repair by an epoxy infiltration method [127].

In order for the packed crack to resume its propagation an external tensile stress, at above the magnitude of the compressive stress developed due to crack packing, had to

be applied. In the case of 100% crack packing the fatigue crack would essentially disappear, leaving only a notch with a stress concentration factor significantly lower than that of the original fatigue crack. Under these circumstances a relatively large number of cycles would be needed to re-initiate the fatigue crack from this notch.

On the other hand, a lower percentage of crack packing would be expected to result in higher compressive stress in the vicinity of the new crack tip due to the load being distributed over smaller area of the packing material. One limitation in this case is the compressive strength of the packing material. At a certain compressive stress the packing material may exhibit yielding, at least in locations that are not directly adjacent to either the old or the new crack tip. This yielded material will tend to be plastically flattened since dislocation motion would not be constrained in these areas. In such cases the crack arrest or the growth retardation may be limited by this plasticity and would tend to reduce compressive stresses. The relationship between the percentage of crack packing and the compressive stress at the crack tip obtained with FEA is shown in Figure 73.

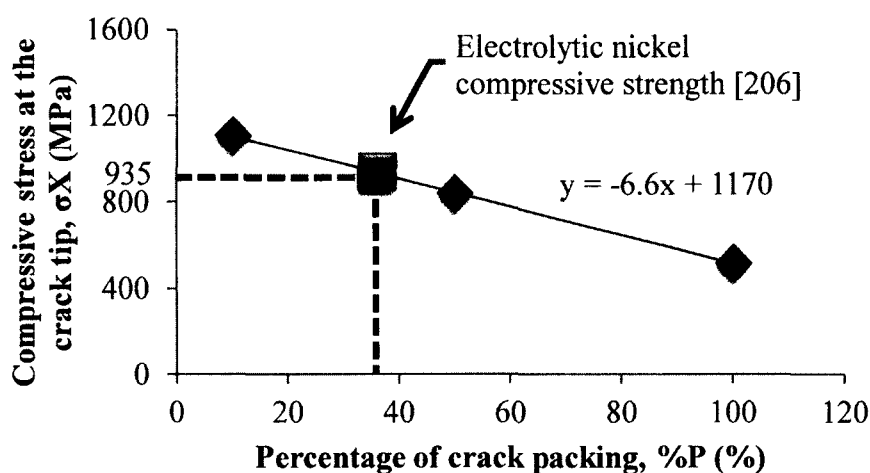


Figure 73. The relationship between the percentage of crack packing and the compressive stress developed at the new crack tip. This data was obtained from Table 9.

As observed previously a higher percentage of crack packing resulted in lower compressive stress developed at the new crack tip. It was also discussed in the preceding paragraph that the maximum compressive stress along the crack surfaces is limited by the value of the compressive strength of the deposit. In the literature the compressive strength of electrolytic nickel was found to be equal to 935 MPa [206]. It was plotted in Figure 73 as a red square point. From Figure 73 it was observed that increasingly positive results from crack packing with nickel can be expected if 36% or more of the crack volume is filled since this is the point where the yield stress of the nickel layer is no longer being exceeded.

The feasibility of applying this method to fatigue management will depend on treatment processing speed. The speed of nickel deposition using the Watts' nickel plating bath (with a current density of 0.15 A/cm³) using the Faraday's Law (Eq. (22)) was found to be equal to approximately 123 mm³/hr. The typical volume of an average fatigue crack grown during this study was calculated using Eq. (28):

$$V = A \times B = \frac{ab}{2} B \quad \text{Eq. (28)}$$

where A is the side area of the crack, B is the thickness of the specimen, a is the length of the fatigue crack, b is the "base" of the crack as shown in Figure 74.

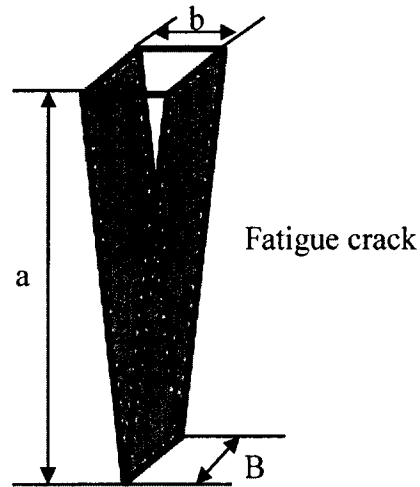


Figure 74. Fatigue crack volume.

The typical volume of an average fatigue crack grown during this study was found to be 610 mm^3 . This suggests that about five hours ($610 \text{ mm}^3 / 123 \text{ mm}^3/\text{hr} \approx 5 \text{ hrs}$) would be required to completely pack that fatigue crack with nickel. In this study fatigue crack packing varied between 11% and 22.5% and was achieved in one hour.

In order to characterize the relationship between the percentage of crack packing and the period of crack re-initiation after treatment the stress intensity factor formula (Eq. (11)) was modified to account for the crack length reduction due to crack packing. The modified formula is represented by Eqs. (29-31):

$$K_{max} - K_{min} = \Delta K_{tr} = \frac{Y(P_{max} - P_{min})}{(W - \Delta a)B} \sqrt{\pi \Delta a} \quad (29)$$

$$Y = 16.7 \left(\frac{\Delta a}{W}\right)^{0.5} - 104 \left(\frac{\Delta a}{W}\right)^{1.5} + 369.9 \left(\frac{\Delta a}{W}\right)^{2.5} - 573.8 \left(\frac{\Delta a}{W}\right)^{3.5} + 360.5 \left(\frac{\Delta a}{W}\right)^{4.5} \quad (30)$$

$$\Delta a = a(100\% - \%P) \quad (\Delta a - \text{Crack length reduction}) \quad (31)$$

where ΔK_{tr} is the stress intensity factor range after crack packing, ΔK is the stress intensity factor before packing, $\%P$ denotes the percentage of crack packing (volume of the deposited material/volume of the fatigue crack), W is the width of the ASTM E399 CT specimen, B is the thickness of the specimen, P_{max} , P_{min} are the maximum and the minimum applied loads, Y is the geometry factor, Δa is the crack length after crack packing which is calculated here for a rectangular crack profile as opposed to an elliptical crack profile. It is important to note that this model assumes that the compressive stress associated with the presence of the nickel layer did not influence the stress experienced by the crack tip.

Equations (29-31) suggest that 100% crack packing would tend to result in the stress intensity factor range equal to zero, meaning that a complete crack arrest will occur. However this condition is unlikely due to the relative non-homogeneity of the nickel deposit (see Figure 67), the possible plastic deformation of the deposited material, the presence of stress concentrations at material imperfections, and the notch. All these sources of stress raisers can cause an arrested crack to re-initiate. Based on these observations it appears that the context of this approach is confined to a finite extension of fatigue life as opposed to producing an infinite life.

Equations (29-31) were used to obtain ΔK_{tr} values for all treated specimens. The Paris Law (Eq. (14)) was then solved for dN using these ΔK_{tr} values, the C and m coefficients for ASTM A36 steel found in the literature and the actual da values obtained during this study [177,180]. The results of this analysis are shown in Table 10.

Table 10. Results of the treated fatigue crack re-initiation analysis based on the crack-length-adjusted stress intensity factor range, ΔK_{tr} . A treatment number is listed for specimens that were treated on several occasions. % P denotes the percentage of crack packing, dN is the number of cycles for crack initiation.

Specimen and treatment #	% P	ΔK (ksi $\sqrt{\text{in}}$)	ΔK_{tr} (ksi $\sqrt{\text{in}}$)	Projected dN based on ΔK , cycles (x1000)	Projected dN based on ΔK_{tr} , cycles (x1000)	Actual dN , cycles (x1000)
E-1	15.2%	25.4	22.3	12.60	18.0	22
D	17.0%	43.5	38.5	4.80	6.8	10
H	13.4%	24.5	21.3	3.68	5.4	61
A	14.0%	51.7	45.1	6.71	9.8	3
E-2	13.4%	28.6	24.9	10.70	22.7	12
2-1	11.0%	22.5	19.0	30.40	48.8	43
2-2	15.6%	53.2	31.8	0.63	2.7	20
2-3	22.5%	63.4	28.9	0.39	3.5	4

Table 10 contains data obtained from eight treatments. The theoretical stress concentration factor range (ΔK) varied from 22.5 ksi $\sqrt{\text{in}}$ up to 63 ksi $\sqrt{\text{in}}$. The range of the percent crack packing was 11% - 22.5%. The projected values of the number of cycles for crack re-initiation (dN) based on ΔK varied within 0.39 – 30.4 thousand cycles. The actual dN values were in the range of 3-61 thousand cycles. The values of the adjusted stress concentration factor (ΔK_{tr}) and the number of cycles for crack re-

initiation (dN) based on ΔK_{tr} varied within 19 – 45.1 ksi $\sqrt{\text{in}}$ and 48.8 – 3.5 thousand cycles respectively.

The average percentage error of the prediction based on ΔK_{tr} from the actual values of (dN) was 71%. The prediction based on ΔK_{tr} was more accurate than the prediction based on ΔK for six out of the eight trials considered. This observation suggests that the model based on ΔK_{tr} can provide reasonable approximations of crack re-initiation after treatment if the percentage of crack packing is known. This successful correlation based on FEA and specimen imaging also indicates that the effective crack length and the local stresses at the new crack tip could be reduced during an electrochemical crack packing treatment.

The bar chart shown in Figure 75 presents a comparison between the actual number of cycles for the re-initiation of treated fatigue cracks with the numbers predicted by the Paris Law using the values of the stress intensity factor range (ΔK), and the values of the modified stress intensity factor range (ΔK_{tr}) that was accounting for the crack length change alone. Figure 76 demonstrates the relationship between ΔK_{tr} and the actual periods of crack re-initiation observed during experiments. Figure 77 shows that relationship in a log-log plot.

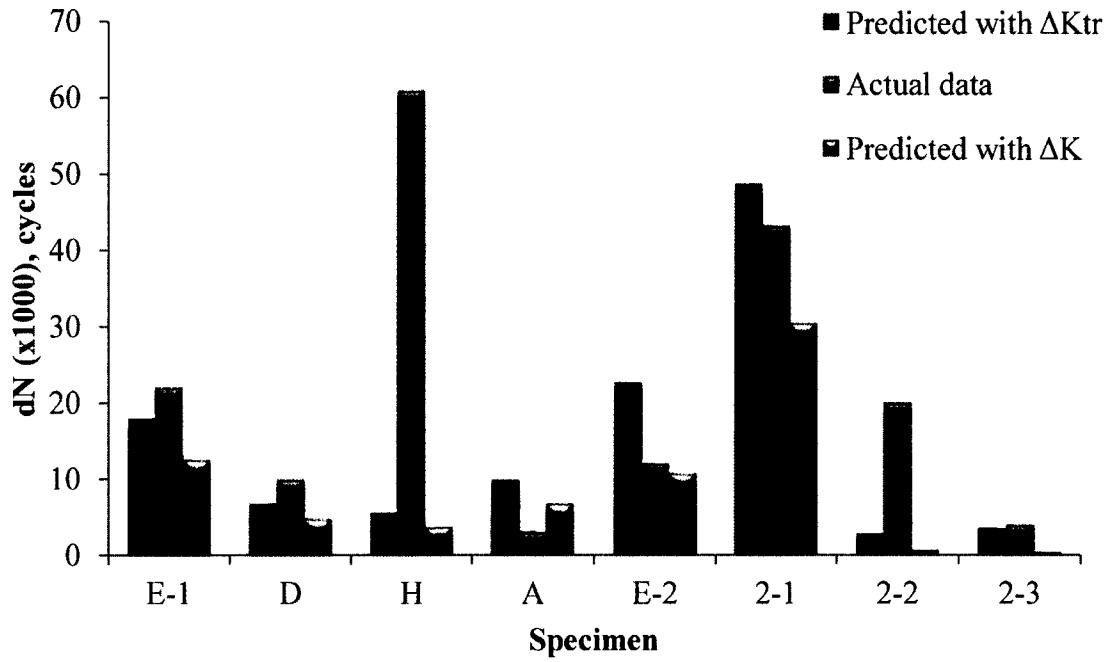


Figure 75. The fatigue cycles required for re-initiation of treated fatigue cracks.

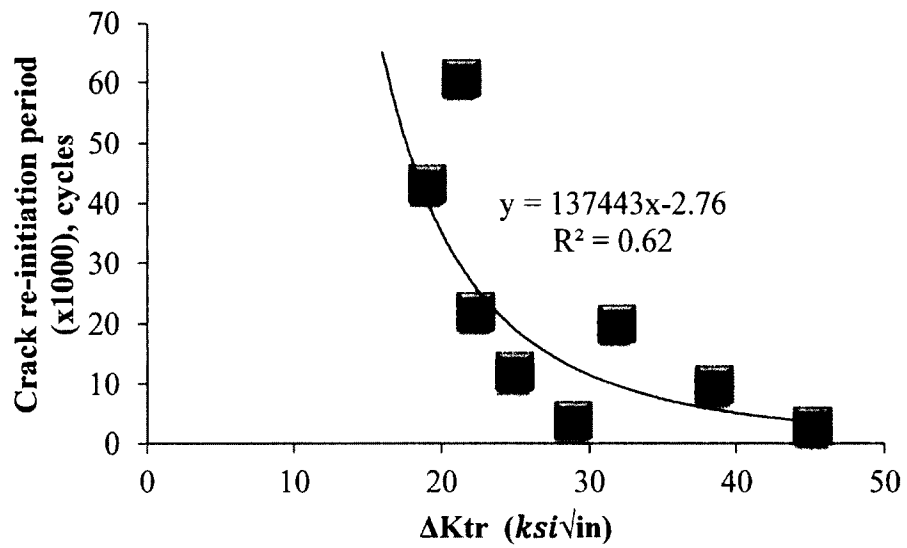


Figure 76. The relationship between ΔK_{tr} and the actual cycles required for crack re-initiation observed during experiments.

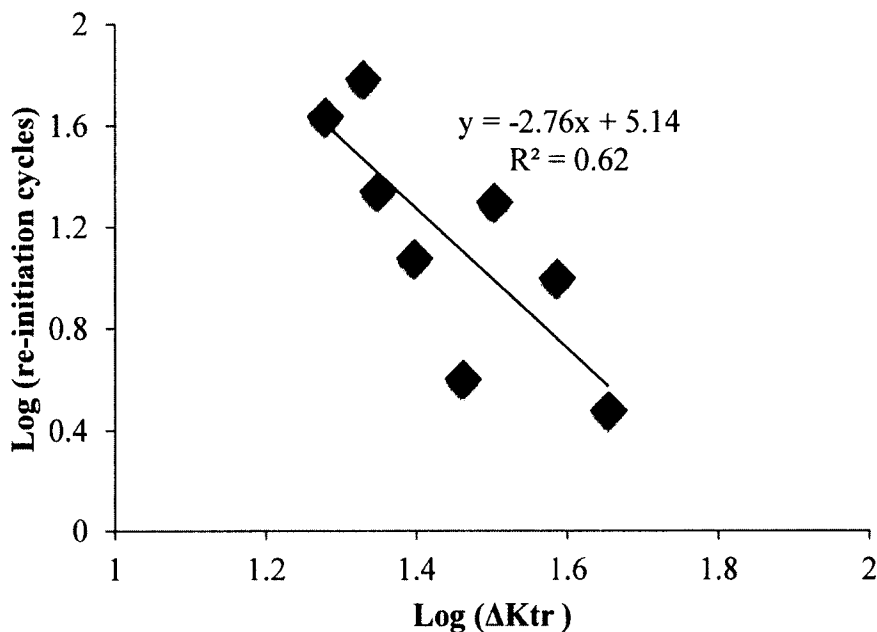


Figure 77. Log-log plot of the relationship between ΔK_{tr} and the actual number of crack re-initiation cycles observed during experiments.

From Figure 76 it was noticed that the period of crack re-initiation after electrochemical treatment was longer when a lower ΔK_{tr} was applied after treatment. ΔK_{tr} is a function of the applied load, the specimen geometry and the percentage of crack packing. The applied load remained the same after treatment, but the length of the fatigue crack was presumably reduced by the crack packing treatment.

The model assumes that a reduction of the crack length resulted from a treatment which provided a reduction of the local stress at the crack tip. As shown in Table 10, the re-initiation life predictions using the Paris law along with the treatment-reduced crack length assumption agreed well with the experimental results. In addition to this general agreement the model also supports the explanation that a higher percentage of crack packing should result in longer fatigue lives. Based on these observations and analyses,

crack packing appeared to prolonged the fatigue lives of the specimens by reducing the lengths of the fatigue cracks which in turn would be expected to reduce the local stresses in the vicinity of the crack tip.

It is notable that the ΔK_{II} model did not account for the compressive stress induced by loading nickel into the crack. Despite this limitation the model tended to predict the re-initiation life of the cracks. It is conceivable that another assumption of the model may have offset this potential shortcoming. The model also assumes that the packing of a crack is thorough and continuous throughout the length of the crack that was intended to receive treatment. From Figures 62, 63, and 67 it is clear that the packing of the crack was not continuous along the intended length. In the case of a discrete crack packing the crack propagation would likely have proceeded faster in areas that did not contain effective nickel and slower in areas at which nickel was deposited. As a crack propagated to an area with no nickel, the local stress would be reconfigured and the radii of the next packing point of nickel (see Figure 78) would essentially force a new series of re-initiation cycles at that point. It is conceivable that crack propagation through the treated crack involved a series of crack re-initiations at various points along the treated crack. Returning now to the model, and the assumption that treatment-induced compressive stress could be neglected, it appears that the under-prediction provided by this assumption could have been compensated by the over-prediction stemming from crack packing that is not truly as continuous as the model also assumes.

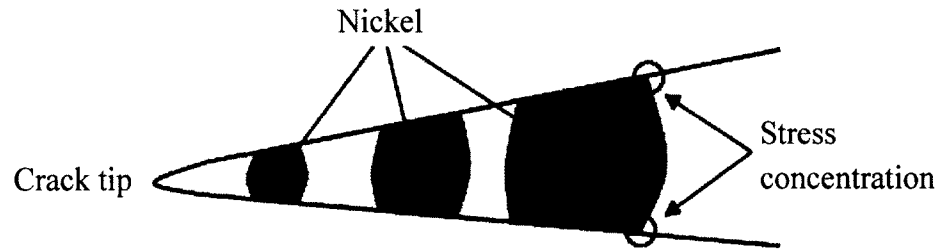


Figure 78. Schematic representation of discrete crack packing. Under these conditions fatigue crack propagation would possibly be arresting and re-initiating several times along a treated crack.

The parameter, ΔK_{tr} correlated well with the crack re-initiation life of the treated cracks in the ASTM A36 steel. This parameter was used along with the electrochemical plating dosage to provide an estimated reduction in crack length. The crack arrest life was calculated based on the assumption that crack propagation was still taking place along the interface between the deposited nickel and the steel crack surface that existed prior to treatment. The re-initiation life was thus estimated by simply calculating the fatigue crack propagation life along the interface between the nickel deposit and the walls of the original crack. The intermittent nature of the nickel deposit did not appear diminish the accuracy of the model because this discontinuity did not effectively reduce the amount of material through which the crack had to travel before it arrived at the original crack tip that existed prior to treatment.

In the first FEM analysis the electrochemical crack treatment was modeled as a uniform layer of nickel packing a fatigue crack. From microscopic images (see Section 4.3) it was observed that electrodeposited nickel developed nonuniform deposits in fatigue cracks that appeared as clumps. Taking into account this observation, in the second FEA, the electrodeposition of nickel was then modeled as an introduction of a

small nickel clump (see Figure 45) that was wedging the fatigue crack. The normal stress distribution in a CT specimen along the X-axis (σ_x) that resulted from the second FEA is shown in Figure 79. Figure 80 shows the normal stress distribution in the vicinity of the crack wedge area. The normal stress distribution in the nickel crack wedge is shown in Figure 81.

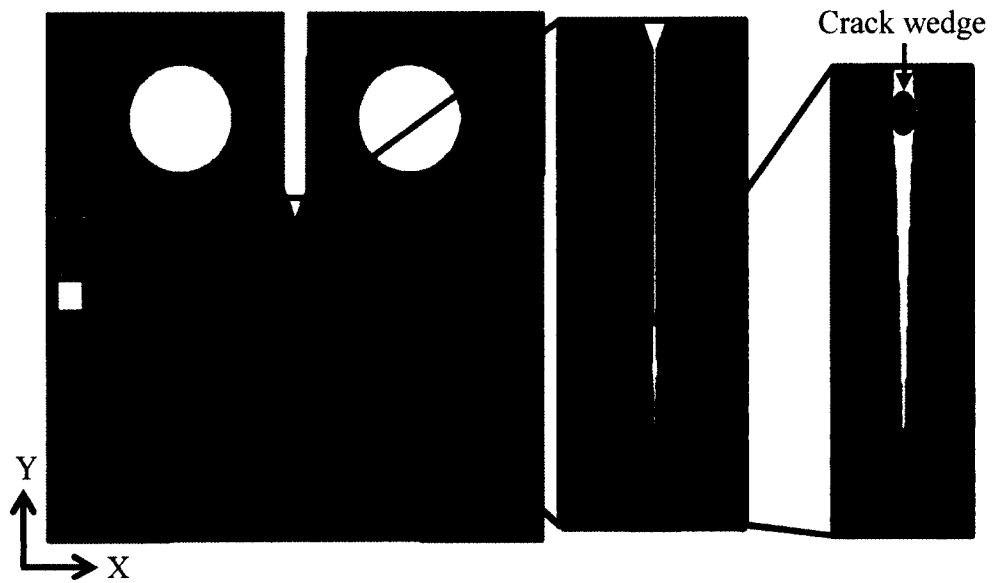


Figure 79. Normal stress distribution along the X-axis (σ_x) in ASTM E399 CT specimen model with a fatigue crack held open by a wedge of nickel at the 3rd step of the transient analysis.

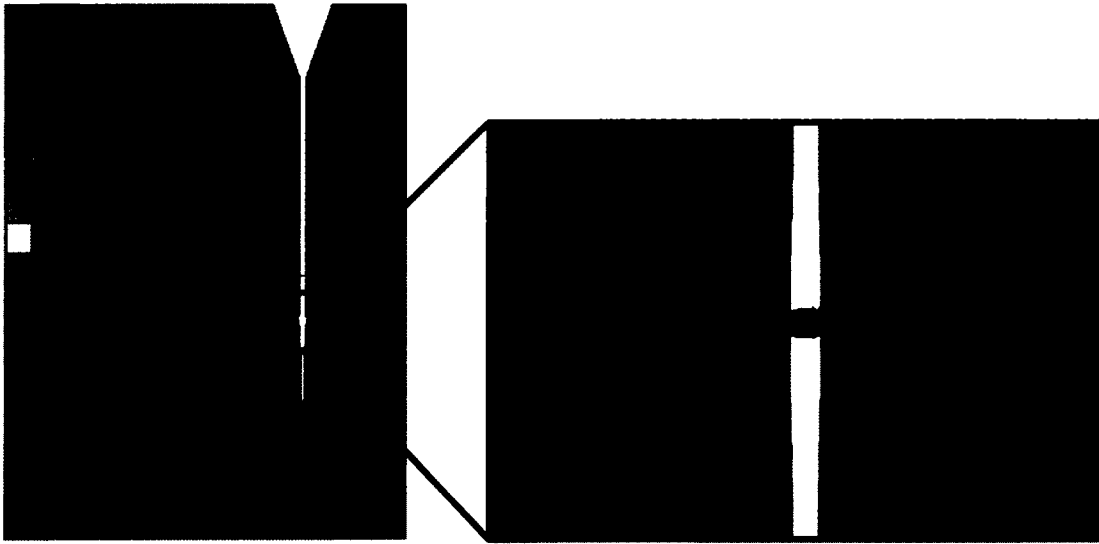


Figure 80. Normal stress distribution along X-axis (σ_x) at the nickel wedge area.

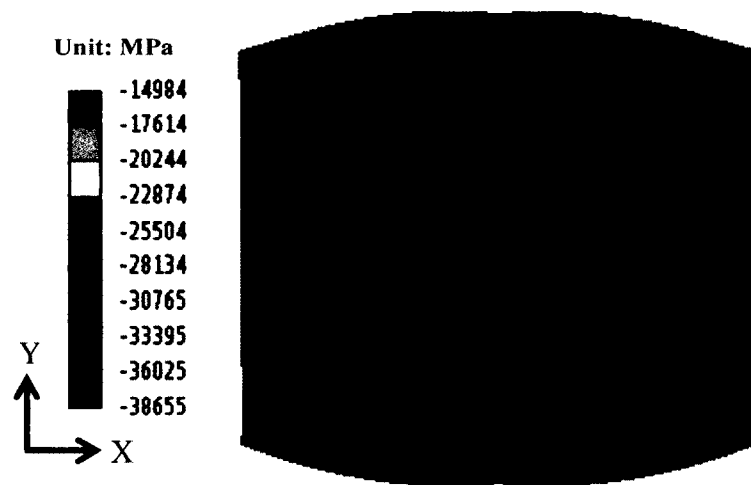


Figure 81. Normal stress distribution along X-axis (σ_x) within the nickel wedge.

In a similar manner as in the previous FEA, the impact of the nickel wedge was modeled using three time steps. The normal stress distribution in this case did not change at steps one and two (similarly as observed in the first FEA, see Figure 72). The maximum tensile stress at the crack tip before introduction of the nickel wedge was 1630

MPa (237 ksi), and the nominal stress was 10.3 MPa (1.5 ksi) resulting in $K_{tg} = 158$. The stress distribution at the third step, after the static load was released, is shown in Figure 68. From Figure 68 it was observed that after the nickel wedge was introduced and the static load was released the maximum normal tensile stress along x-axis was 927 MPa (135 ksi) located just beyond the crack tip. The maximum compressive stress was -3480 MPa (505 ksi) located in the vicinity of the crack wedge. The nominal stress was 437 MPa (63.4 ksi). The nickel wedge was in compression. The maximum compressive stress was developed at the points of contact between the top edge of the nickel wedge and the fatigue crack surfaces (see Figure 80). These points exhibited stress concentration factors, K_{tg} of approximately 8 ($\sigma_{max}/\sigma_{nom} = (505 \text{ ksi})/(63.4 \text{ ksi})$). These stress concentration factors were approximately 6 times lower than those of the notches observed in the optical image of the treated fatigue crack (see Figure 64).

In the current finite element analysis the stress concentration factor (K_{tg}) at the new crack tip (top edge of the nickel wedge) was 8, while the stress concentration at the crack tip before treatment was 158. Assuming that crack re-initiation will take place at the new crack tip it could be noted that introduction of nickel wedge reduced the fatigue inducing stress concentration factor from 158 to 8. A similar reduction of the stress concentration factor was observed in the first FEA, where electrochemical treatment was simulated as crack packing with nickel layers occupying 10%, 50% and 100% of the crack. In that case the K_{tg} was also reduced from 158 to around 8.

The tensile stress predicted by the FEA was almost four times larger than the yield strength of ASTM A36 steel reported by the supplier [171]. Under such high tensile stress plastic deformation of the steel will be possible and crack tip blunting (described in

Section 2.1.6) could occur. Crack tip blunting was previously shown to be one of the mechanisms of crack growth retardation [66,207,208]

The FEA illustrated in Figure 81 revealed that a crack closure load distributed over a small wedge area of plated nickel results in compressive stresses that are 3-4 times the compressive yield strength of the electrolytic nickel [206]. Under such high stresses the fatigue crack wedge could be significantly plastically deformed resulting in relatively low stress increases at the old crack and thus limited crack tip blunting. This in turn would reduce the tendency for crack arrest or crack growth retardation. By comparison, Vecchio *et al.* and Hertzberg *et al.* explored wedging-induced crack closure phenomenon by insertion of needle tips at various locations in the wake of fatigue cracks in 2024 aluminum alloy. They observed that significant crack closure produced only a slight reduction of crack growth rate when a closure object (crack wedge) did not possess a large area [209,210]. Thus it appears that the effect of crack wedging on fatigue crack behavior is expected to be more significant as the size of the crack wedge increases.

The finite element models developed in this study may be used to determine stresses (and their distribution) that will develop after introduction of foreign objects into the fatigue crack in ASTM E399 CT specimen. Knowing these stresses one can calculate the minimum percentage of the crack packing or the minimum dimensions of the crack wedge that will be required to withstand the crack closure load without plastic deformation of the crack wedge. This will tend to enable the specification of a crack wedge that will not be plastically deformed in the process and thus provide a more significant effect on crack behavior after treatment.

4.6 Corrosion Susceptibility Analysis

Corrosion susceptibility tests were performed to evaluate the effect of electrochemical crack treatment on the corrosion resistance of the ASTM A36 base metal. Corrosion potential and corrosion currents were measured as described in Section 3.7. The average corrosion potential with respect to the Cu/Cu sulfate reference electrode was measured over a period of twelve weeks. These readings were taken for electrolytic nickel, as well as nickel-plated and non-plated ASTM A36 steel while immersed in simulated seawater solution (3.5 wt% NaCl) at a temperature of 22 °C – 25.2 °C. These results are shown in Figure 82.

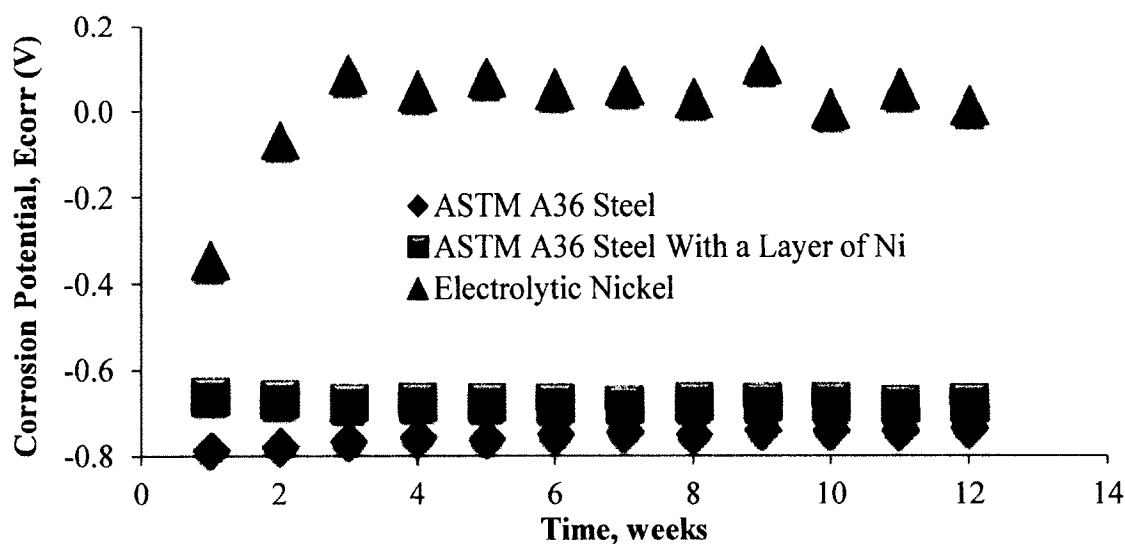


Figure 82. Corrosion potential of electrolytic nickel, nickel-plated ASTM A36 steel, and non-plated ASTM A36 steel in 3.5 wt% NaCl solution. These were measured with respect to a copper-copper sulfate reference electrode.

Figure 82 reveals that the corrosion potential of the ASTM A36 steel stabilized after 5 weeks and was equal to -0.75 volts. The observed corrosion potential was 30%-

43% more negative than values found in the literature [211-213]. One value of ASTM A36 steel corrosion potential that was found in literature was obtained in 10 wt% NaCl water solution at 30 ± 2 °C and was equal to -0.506 V [211]. Another value was obtained in an aqueous solution with a pH value of 5 at 25 °C and was equal to -0.502 V [212]. The third value found in literature was -0.574 V and was obtained in 3 wt% NaCl solution at “ambient” temperature [213]. All referenced values of A36 steel corrosion potential found in the literature were measured with a saturated calomel reference electrode. The corrosion potential of the electrolytic nickel stabilized after 3 weeks with a mean value of +0.05 volts and a standard deviation of 0.03 volts. These values were similar to data found in the literature [214,215]. One value found in the literature was -0.16 V measured in “city” water with the addition of 3 wt% NaCl after 7 months of exposure [214]. Another value from the literature was +0.08 V measured in 1.2 wt% NaCl solution at pH = 6.1 [215]. The temperature at which these values were measured was not reported.

The corrosion current values measured during periodic linear polarization resistance tests were converted into corrosion rates in terms of mils per year (mpy) as shown in Figure 83. The average corrosion rates of all specimens were compared in a bar chart shown in Figure 84. This chart also includes the galvanic corrosion rate between the plated nickel and the ASTM A36 steel that were conducted using a galvanostatic zero resistance ammeter setup as described in Section 3.7. The surface area ratio between steel and nickel specimens was 1:1.

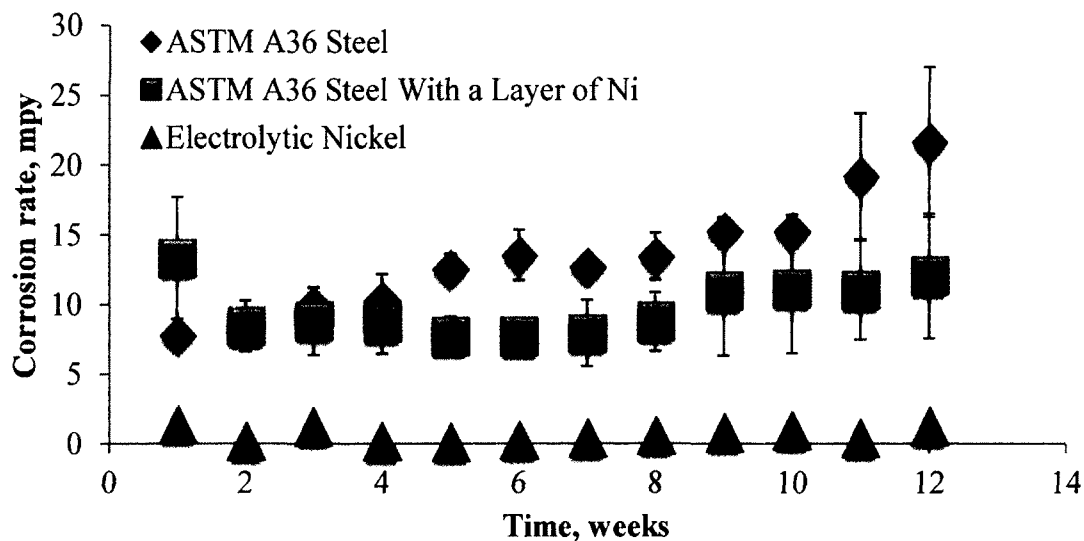


Figure 83. Corrosion rates of electrolytic nickel, nickel-plated ASTM A36 steel and non-plated ASTM A36 steel. These corrosion rates were measured in 3.5 wt% NaCl solution at 22-25 °C. Each data point is an average of 5 trials.

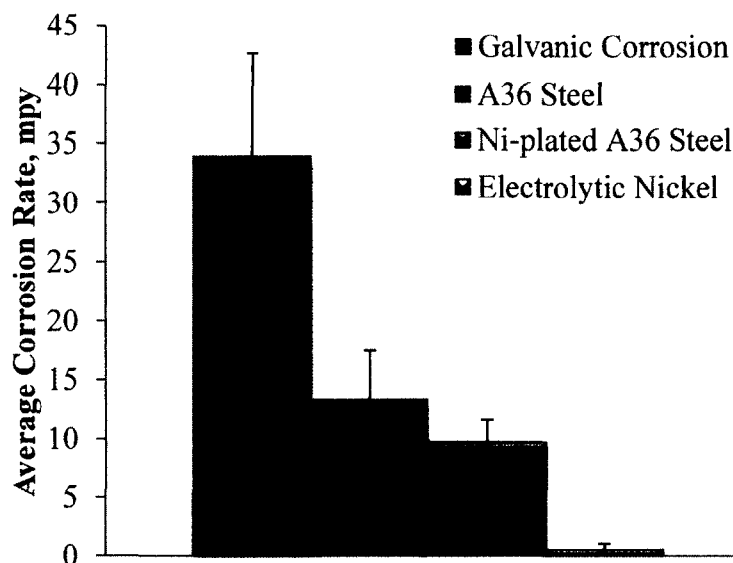


Figure 84. Average corrosion rates in simulated seawater solution (3.5 wt% NaCl). The galvanic corrosion rate between ASTM A36 steel and electrolytic nickel deposit was measured using the galvanostatic zero resistance ammeter (GZRA) method. The other corrosion rates were obtained using the linear polarization resistance method.

From Figure 83 it was observed that after 12 weeks the average corrosion rate of the ASTM A36 steel was 21.7 mpy. The comparable A36 steel corrosion rates found in the literature varied from 5.8 mpy to 77.3 mpy [211,212,216,217]. The average corrosion rate of the nickel-plated A36 steel after 12 weeks was in the vicinity of 12 mpy which was approximately 80% lower than the corrosion rate of the bare A36 steel. The corrosion rate of electrolytic nickel after 12 weeks was 1.2 mpy. In comparison the corrosion rate of electrolytic nickel in seawater found in the literature varied from 0.02 mpy to 6.9 mpy [214,218,219]. The average galvanic corrosion rate between the ASTM A36 steel and electrolytic nickel deposit was 34 mpy. The steel was corroding in this case. This corrosion value was found to be 2.7 times higher than a galvanic corrosion rate found in the literature between carbon steel (0.24% C) and nickel in seawater after 8 years of exposure [220]. For general corrosion or galvanic corrosion, it would make sense that any given corrosion rate would tend to drop over time as oxides would tend to accumulate on the corroding surface, increasing the corrosion circuit resistance and so progressively inhibiting the corrosion rate.

Figure 83 shows that the corrosion rate of all the specimens was increasing with the time. The room temperature varied only within a range 3.2 °C (22 °C – 25.2 °C) and thus cannot be responsible for the growth of the corrosion rates. The corrosion potential was relatively stable during the 12-week experiment period (see Figure 82). During this period the evaporation of water from the electrolyte (simulated seawater) probably caused the corrosion rate growth observed over the 12-week time period since this would have caused the NaCl concentration to increase over time. In addition, CO₂ absorption could also have reduced the solution pH and contributed to an increase in corrosion rate.

The corrosion rate was calculated using current density values (I/A , A/cm²). The decreasing level of the electrolyte was reducing the specimen's surface area that was immersed into it and thus the current density was increasing, consequently increasing the corrosion rate over the time. The salt concentration was presumably increasing over this period as well. The corrosion rate growth over time of the nickel-plated steel was slower than that of the bare A36 steel.

It should be noted that the value of the general corrosion rate of nickel-plated steel was expected to be lower, closer to the value of the corrosion rate of electrolytic nickel. It was also observed that the corrosion rate of the nickel-plated steel experienced relatively larger scatter during the last 4 weeks of the test as compared to the first eight weeks. Starting from the ninth week two of the specimens (specimen 2 and 3) experienced larger corrosion rates than the other three nickel-plated specimens. By the end of the 12th week the corrosion rates of these two specimens were almost twice as high as the other three.

After the 12 week test period the nickel layers were removed from plated specimens 2 and 3 for visual examination. Crevice corrosion was observed on the steel surface on specimen 2 that had been plated. A large corrosion crevice was also observed under the plated surface of specimen 3 (see Figure 85). These areas of localized corrosion were possibly be caused by poor adherence of nickel plating to the surface of the substrate or by an edge effect of epoxy molding. It appears that epoxy did not provide perfect sealing and permitted penetration of the electrolyte onto metal surfaces. In addition, cutting tool marks left grooves on the surface of the substrate steel allowing the salt water to penetrate under the nickel layer causing crevice and pitting corrosion. It appears that the localized corrosion could be responsible for the increased corrosion rate

of specimens 2 and 3. The average corrosion rate of the other 3 nickel-plated specimens was 9 mpy, which was more than 1/2 the observed corrosion rate of the bare ASTM A36 steel. Visual inspection of the surface of the nickel-plated specimens revealed that these specimens (except specimens 2, 3) experienced significantly lower corrosion rates as compared to the non-plated steel specimens. This observation suggests that nickel-plating of ASTM A36 steel brings benefits in terms of lower corrosion susceptibility and lower corrosion rate as was previously demonstrated by many authors [144,147,159,203,219-222]. This benefit applies to general corrosion protection. Where there is potential for imperfect plating such as for non-uniform surfaces the possibility of crevicing needs to be considered.

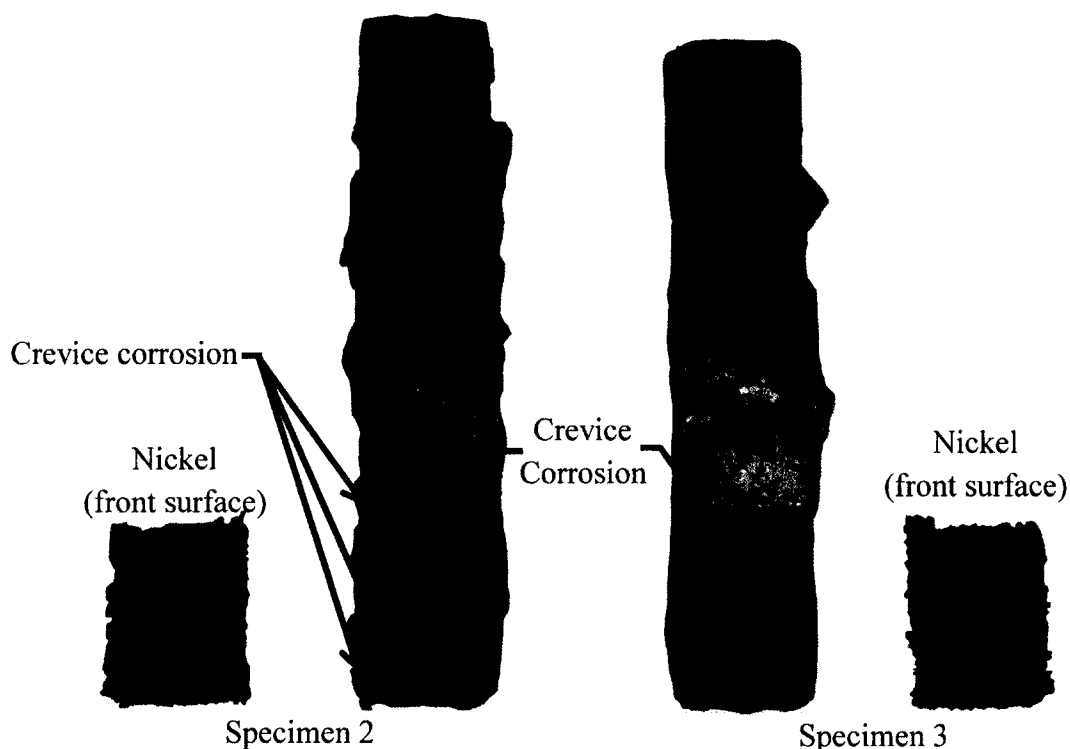


Figure 85. Nickel-plated ASTM A36 steel specimens with localized corrosion after 12 weeks in 3.5% NaCl solution. The deposited nickel layers were removed prior to imaging.

Corrosion protection of steel by electroplated nickel depends on the quality of the plating. One of the main parameters of plating quality is the porosity of the as-plated material which depends on plating thickness, substrate surface roughness, plating solution contaminants and the type of plating bath used. It was previously shown that the galvanic corrosion between a substrate metal and a plated metal initiates as the formation of galvanic cells. If pores in the plating material reach the substrate, these galvanic cells can possibly form within the pores of the plated material and propagate under the deposit as galvanically assisted crevices. The resistance of the galvanic corrosion cell is a function of the plating thickness, the resistivity of the electrolyte and the cross-sectional area of the pore [223].

Electroless nickel has been reported to exhibit superiority over electrolytic nickel in terms of corrosion protection [224,225]. In one example it has been shown that 12 μm thick electroless nickel (EN) coating has provided better corrosion protection than a twice thicker electrolytic nickel coating. Electroless nickel has also been found to be resistant to under-deposit and interface attack [226]. Recently it was found that the density, the hardness and the corrosion resistance of electroless nickel plating can be further improved by post-heat-treatment [221,227].

Taking into account the reported advantages of electroless nickel plating over electrolytic nickel in terms of wear and corrosion resistance it is recommended that electroless nickel plating be examined as a substitution to electroplating for the electrochemical treatment purposes. It would be interesting to compare the electrolytic nickel plating to the electroless nickel plating in terms of the effect on fatigue crack behavior under similar loading and environmental conditions.

Figure 82 shows that the nickel exhibits a significantly more positive corrosion potential than the steel. Galvanic corrosion was observed in this study as shown in Figure 84. In this case the steel was suffering crevicing attack that was galvanically assisted by the nickel. In Figures 62 - 64 incomplete plating of nickel within a steel crack was evident. Under these circumstances it would be expected that corrosion of the steel would occur as assisted by the nickel. This corrosion would be localized within the crack and likely undermine the fatigue benefits of the treatment by inducing a corrosion fatigue process. In light of these corrosion findings it is recommended that an alternative plating metal be considered that could possibly exhibit a lower galvanic potential difference that exists between electrolytic nickel and the ASTM A36 steel. This new candidate would probably work well if the yield strength were comparable to that of the A36 steel.

CHAPTER 5

CONCLUSIONS

The electrochemical method of fatigue crack treatment was developed, described and analyzed. The method was based on placing fatigue cracks under compression by depositing nickel onto the surfaces of the cracks.

During this study the following useful and interesting observations were made:

1. The growth rates of all fatigue cracks observed in ASTM E399 Compact-Tension specimens made of ASTM A36 steel before treatment were in good correlation with data found in the literature.
2. The propagation of the fatigue cracks before treatment was well characterized by the Paris Law.
3. The electrochemical fatigue crack treatment method succeeded in arresting fatigue crack propagation.
4. The fatigue crack arrest period varied from two thousand to thirty thousand cycles in this study.
5. The fatigue life of the specimens was extended primarily by crack arrest. In some cases some relatively slow propagation also contributed to propagation life extension that reached as high as 55,000 cycles.

6. This current method of fatigue crack treatment may be applied more than once in the life of a propagating crack and yield significant life extension following each application. Subsequent electrochemical treatments can be applied as a regular maintenance practice that can be designed to extend fatigue crack propagation life indefinitely.
7. The behavior of the cracks after treatment was characterized by a period of arrest and resumption of the propagation.
8. The periods of crack arrest and fatigue life extension observed in the current study may be translated into approximately 0.6-15 years of a typical oil pipeline operation or 2.4-66 years of a typical gas pressure vessel operation.
9. The current approach appears to provide benefits that are within an order of magnitude of the best achievement reported in the literature but produces these results using an approach that can be field applied more easily.
10. The treated fatigue cracks were similar to the ASTM E399 CT V-shaped notches in terms of the number of cycles required for fatigue (re-) initiation.
11. The conventional elastic-plastic strain life analysis provided reasonable approximations of fatigue lives of V-shaped starter notches, but may not be suitable for achieving a reasonable re-initiation life of electrochemically treated fatigue cracks without better understanding of the deposited nickel distribution and its strain life fatigue properties.
12. A power law relationship between the period of crack arrest and the stress intensity factor range (ΔK) applied during post-treatment cycling was observed

13. Optical and scanning electron microscopy revealed that electrochemical treatment was intermittently loading the fatigue cracks with nickel deposits that exhibited arc-shaped edges. This lack of deposit uniformity stemmed from an apparent lack of electric field uniformity along the length of the crack.
14. The packing of a fatigue crack tip with nickel may result in a significant reduction of the stress concentration factor.
15. The efficiency of the plating setup ($\%F$) was equal to 85%.
16. Energy dispersive spectroscopic analysis demonstrated the presence of nickel within electrochemically treated fatigue cracks.
17. Due to the potential for mutual diffusion of nickel and iron, the treatment process may yield a galvanic corrosion potential between ASTM A36 steel and nickel that could be lower than what may be anticipated by comparison of the two metals in a galvanic series table or in a simple galvanic corrosion measurement.
18. The finite element analysis predicted development of compressive stress at the new fatigue crack tip due to electrochemical treatment that uniformly packs the crack. The stress was in reverse proportion to the percentage of the crack that was packed with nickel, starting at the old crack tip and extending toward the crack mouth opening.
19. FEA of the fatigue crack with an introduced nickel wedge showed that the new crack tip (top edge of the wedge) was under compression.
20. Based on the finite element analysis coupled with the crack propagation results, a higher percentage of crack packing would tend to reduce the stress intensity and

the stress concentration factor at the new crack tip and thus increase the fatigue crack re-initiation life.

21. In order for the packed crack to resume its propagation an external tensile stress above the magnitude of the compressive stress developed due to crack packing, had to be applied.
22. A lower percentage of crack packing would be expected to result in higher compressive stress in the vicinity of the new crack tip due to the load being distributed over smaller area of the packing material.
23. The maximum compressive stress developed at the new crack tip (due to treatment) is limited by the minimum compressive strength of the substrate metal and the deposit.
24. In the current study it was observed that increasingly positive results from crack packing with nickel can be expected if 36% or more of the crack volume is filled (calculated using the dimensions of the specimens tested during this study).
25. The parameter, ΔK_{cr} correlated well with the crack re-initiation life of the treated cracks in the ASTM A36 steel. This parameter was used along with the electrochemical plating dosage to provide an estimated reduction in crack length. The crack arrest life was calculated based on the assumption that crack propagation was still taking place along the interface between the deposited nickel and the steel crack surface that existed prior to treatment. The re-initiation life was thus estimated by simply calculating the fatigue crack propagation life along the interface between the nickel deposit and the walls of the original crack. The intermittent nature of the nickel deposit did not appear diminish the accuracy of

the model because this discontinuity did not effectively reduce the amount of material through which the crack had to travel before it arrived at the original crack tip that existed prior to treatment.

26. The average percent error of the prediction based on ΔK_{tr} from the actual values of (dN) was 71%. The prediction based on ΔK_{tr} was more accurate than the prediction based on ΔK , 6 times out of 8.
27. The re-initiation life predictions obtained using the Paris law along with the treatment-reduced crack length assumption agreed well with the experimental results.
28. The crack treatments appeared to prolong the fatigue lives of the specimens by reducing the lengths of the fatigue cracks which in turn would be expected to reduce the local stresses in the vicinity of the crack tip.
29. The finite element analysis predicted significant reduction of the stress concentration factor at the new crack tip due to theoretically uniform packing of the crack.
30. The finite element model of the ASTM E399 Standard Compact-Tension specimen informed by treated crack microscopy demonstrated that the stress concentration factor at the crack tip was reduced significantly due to electrochemical treatment.
31. Based on an elastic FEA that was modeled from images of treated cracks, it appears that the electrochemical treatments tended to reduce crack tip stresses significantly. Re-initiation life estimates based on the ΔK_{tr} model did not incorporate any such stress reductions.

32. The effect of the crack wedging on the fatigue crack behavior is expected to be more significant if the crack closure load is distributed over a relatively large crack wedge area.
33. Electrochemical treatment was found beneficial in terms of improved corrosion resistance of treated specimens as long as the deposited nickel was free of defects that could cause localized, galvanically-assisted, corrosion of the ASTM A36 base metal.
34. After 12 weeks of simulated seawater exposure the average corrosion rate of the nickel-plated ASTM A36 steel was 80% lower than that of the non-plated ASTM A36 steel.
35. In some cases the adherence of nickel plating was poor and resulted in formation of localized corrosion. When the plating operation did not yield a perfect film, localized corrosion of the steel base metal was observed.

During this study several opportunities for further exploration and improvement of the electrochemical fatigue crack treatment method were identified. They are described in the following recommendations:

1. Application of sulfamate nickel plating bath solutions may be attempted. Sulfamate nickel plating solutions are expected to result in improved mechanical and corrosion resistance properties of nickel deposits thus prolonging the fatigue life, extending the fatigue crack arrest period and improving the corrosion resistance.
2. Taking into account the advantages of the electroless nickel over the electrolytic nickel in terms of wear and corrosion resistance it is recommended to examine

electroless nickel plating as a substitution to electroplating for the electrochemical treatment purposes. It would be interesting to compare the electrolytic nickel plating to electroless nickel plating in terms of the effect on fatigue crack behavior under similar loading and environmental conditions.

3. Experimental proof of the relationship between the percentage of crack packing and the period of fatigue crack re-initiation (observed in finite element analysis) is needed. For this purpose a range of crack packing percentages could be tested.
4. It would be beneficial to measure the actual crack length and the distribution of crack packing material after each treatment. This data will allow more accurate characterization of the crack treatment effect.
5. The possibility of slowed crack propagation after treatment may be explored and analyzed.
6. Using the crack re-initiation data presented in this study one can attempt the application of electrochemical treatment on several occasions preceding crack re-initiation. This will allow testing of the “infinite crack arrest” hypothesis due to a periodic treatment.
7. An alternative plating metal be considered that could possibly exhibit a lower galvanic potential difference than what exists between electrolytic nickel and the ASTM A36 steel. This new candidate would probably work well if the yield strength were comparable to that of the A36 steel.
8. In order to commercialize this technology and propose it as an engineering method of fatigue crack treatment an economic feasibility assessment is required.

APPENDIX

FATIGUE CYCLIC LOADING DATA

Table A1. Fatigue crack propagation in specimen 2

Number of Cycles, N	Crack Mouth Opening, V_m (in)	Crack Length, a (in)	ΔK (ksi $\sqrt{\text{in}}$)
0	0.191	1.34	19.0
14,159	0.191	1.34	19.0
19,755	0.191	1.34	19.0
25,000	0.192	1.40	20.2
42,550	0.193	1.45	21.2
50,000	0.194	1.50	22.3
75,000	0.195	1.54	23.2
100,000	0.196	1.58	24.3
125,000	0.198	1.65	26.2
150,000	0.199	1.68	18.0
175,000	0.200	1.71	18.8
200,000	0.202	1.76	14.7
225,000	0.206	1.85	16.5
TREATMENT 1			
225,000	0.206	1.85	22.5
250,000	0.206	1.85	22.5
293,236	0.260	2.29	48.5
293,237	0.264	2.33	53.2
295,237	0.264	2.33	53.2
297,237	0.264	2.33	53.2
299,237	0.264	2.33	53.2
301,237	0.264	2.33	53.2
303,237	0.264	2.33	53.2
308,237	0.264	2.33	53.2
313,237	0.274	2.36	57.0
TREATMENT 2			
313,238	0.287	2.40	63.4
315,238	0.287	2.40	63.4
317,238	0.301	2.43	68.8

Table A2. Fatigue crack propagation in specimen A

Number of Cycles, N	Crack Mouth Opening, V_m (in)	Crack Length, a (in)	ΔK (ksi $\sqrt{\text{in}}$)
0	0.183	1.02	22.5
10,000	0.183	1.02	22.5
20,000	0.183	1.02	22.5
40,000	0.183	1.02	22.5

Table A2 continued

Number of Cycles, N	Crack Mouth Opening, V_m (in)	Crack Length, a (in)	ΔK (ksi $\sqrt{\text{in}}$)
40,001	0.183	1.02	24.9
50,000	0.183	1.02	24.9
60,000	0.183	1.02	24.9
60,001	0.183	1.02	26.9
65,000	0.184	1.12	29.3
70,000	0.184	1.12	29.3
75,000	0.184	1.12	29.2
80,000	0.184	1.12	29.3
80,001	0.184	1.12	32.1
85,000	0.186	1.27	36.7
90,000	0.188	1.40	41.4
95,000	0.193	1.61	49.8
TREATMENT			
95,000	0.193	1.61	51.7
96,000	0.193	1.61	51.7
97,000	0.193	1.61	51.7
98,000	0.205	1.91	75.2

Table A3. Fatigue crack propagation in specimen C

Number of Cycles, N	Crack Mouth Opening, V_m (in)	Crack Length, a (in)	ΔK (ksi $\sqrt{\text{in}}$)
0	0.178	0.70	22.3
20,000	0.179	0.78	24.0
40,000	0.183	1.20	34.5
50,000	0.184	1.27	36.7
60,000	0.188	1.50	45.7
65,000		FAILURE	

Table A4. Fatigue crack propagation in specimen D

Number of Cycles, N	Crack Mouth Opening, V_m (in)	Crack Length, a (in)	ΔK (ksi $\sqrt{\text{in}}$)
0	0.184	0.92	27.0
10,000	0.187	1.20	34.5
30,000	0.188	1.27	36.7

Table A4 continued

Number of Cycles, N	Crack Mouth Opening, V_m (in)	Crack Length, a (in)	ΔK (ksi $\sqrt{\text{in}}$)
40,000	0.191	1.45	43.5
TREATMENT			
40,000	0.191	1.45	43.5
41,000	0.191	1.45	43.5
42,000	0.191	1.45	43.5
43,000	0.191	1.45	43.5
44,000	0.191	1.45	43.5
45,000	0.191	1.45	43.5
46,000	0.191	1.45	43.5
47,000	0.191	1.45	43.5
48,000	0.191	1.45	43.5
49,000	0.191	1.45	43.5
50,000	0.194	1.58	49.8
51,000	0.196	1.65	55.7
52,000	0.199	1.74	59.9

Table A5. Fatigue crack propagation in specimen E

Number of Cycles, N	Crack Mouth Opening, V_m (in)	Crack Length, a (in)	ΔK (ksi $\sqrt{\text{in}}$)
0	0.179	0.70	11.8
2,000	0.179	0.70	11.8
4,000	0.179	0.70	11.8
6,000	0.179	0.70	11.8
8,000	0.179	0.70	11.8
10,000	0.179	0.70	11.8
12,000	0.179	0.70	11.8
15,000	0.179	0.70	11.8
18,000	0.179	0.70	11.8
21,000	0.179	0.70	11.8
24,000	0.179	0.70	11.8
27,000	0.179	0.70	11.8
30,000	0.179	0.70	11.8
33,000	0.179	0.70	11.8
36,000	0.179	0.70	11.8

Table A5 continued

Number of Cycles, N	Crack Mouth Opening, V_m (in)	Crack Length, a (in)	ΔK (ksi $\sqrt{\text{in}}$)
40,000	0.179	0.70	11.8
43,000	0.179	0.70	11.8
46,000	0.179	0.70	11.8
50,000	0.179	0.70	11.8
55,000	0.179	0.70	11.8
60,000	0.179	0.70	11.8
65,000	0.179	0.70	11.8
67,000	0.179	0.70	11.8
69,000	0.179	0.70	11.8
71,000	0.179	0.70	11.8
73,000	0.179	0.70	11.8
75,000	0.179	0.70	11.8
77,000	0.179	0.70	11.8
79,000	0.179	0.70	11.8
81,000	0.179	0.70	11.8
83,000	0.179	0.70	11.8
85,000	0.179	0.70	11.8
87,000	0.179	0.70	11.8
90,000	0.179	0.70	11.8
95,000	0.179	0.70	11.8
100,000	0.179	0.70	11.8
105,000	0.179	0.70	11.8
120,000	0.179	0.70	11.8
123,000	0.179	0.70	11.8
130,000	0.179	0.70	11.8
135,000	0.179	0.70	11.8
140,000	0.179	0.70	11.8
145,000	0.179	0.70	11.8
150,000	0.180	0.79	12.9
153,000	0.180	0.79	12.9
156,000	0.180	0.79	12.9
158,000	0.180	0.79	12.9
160,000	0.180	0.79	12.9
163,000	0.180	0.79	12.9
166,000	0.180	0.79	12.9
169,000	0.180	0.79	12.9
172,000	0.180	0.79	12.9
175,000	0.180	0.79	12.9

Table A5 continued

Number of Cycles, N	Crack Mouth Opening, V_m (in)	Crack Length, a (in)	ΔK (ksi $\sqrt{\text{in}}$)
180,000	0.180	0.79	12.9
185,000	0.180	0.79	12.9
190,000	0.180	0.79	12.9
195,000	0.180	0.79	12.9
200,000	0.180	0.79	12.9
205,000	0.180	0.79	12.9
210,000	0.180	0.79	12.9
215,000	0.180	0.79	12.9
220,000	0.180	0.79	12.9
240,000	0.180	0.79	12.9
250,000	0.180	0.79	12.9
260,000	0.180	0.79	12.9
270,000	0.181	0.92	14.4
280,000	0.181	0.92	14.4
290,000	0.181	0.92	14.4
310,000	0.181	0.92	14.4
328,000	0.182	1.03	15.8
335,000	0.182	1.03	15.8
345,000	0.182	1.03	15.8
355,000	0.182	1.03	15.8
365,000	0.183	1.12	17.1
375,000	0.183	1.12	17.1
385,000	0.183	1.12	17.1
395,000	0.183	1.12	17.1
405,000	0.183	1.12	17.1
425,000	0.183	1.12	17.1
445,000	0.184	1.20	18.3
465,000	0.184	1.20	18.3
485,000	0.185	1.27	19.5
505,000	0.185	1.27	19.5
525,000	0.186	1.34	20.8
535,000	0.187	1.40	22.0
555,000	0.190	1.54	25.3
TREATMENT 1			
555,000	0.190	1.54	25.3
557,000	0.190	1.54	25.3
559,000	0.190	1.54	25.3
561,000	0.190	1.54	25.3
563,000	0.190	1.54	25.3
565,000	0.190	1.54	25.3
567,000	0.190	1.54	25.3
569,000	0.190	1.54	25.3

Table A5 continued

Number of Cycles, N	Crack Mouth Opening, V_m (in)	Crack Length, a (in)	ΔK (ksi $\sqrt{\text{in}}$)
571,000	0.190	1.54	25.3
573,000	0.190	1.54	25.3
575,000	0.190	1.54	25.3
577,000	0.192	1.62	27.5
581,000	0.193	1.65	28.6
TREATMENT 2			
581,000	0.193	1.65	28.6
583,000	0.193	1.65	28.6
585,000	0.193	1.65	28.6
587,000	0.193	1.65	28.6
589,000	0.193	1.65	28.6
591,000	0.193	1.65	28.6
593,000	0.196	1.74	31.8
595,000	0.198	1.79	33.9

Table A6. Fatigue crack propagation in specimen H

Number of Cycles, N	Crack Mouth Opening, V_m (in)	Crack Length, a (in)	ΔK (ksi $\sqrt{\text{in}}$)
0	0.166	0.84	11.6
52,258	0.166	0.85	11.7
113,335	0.166	0.88	12.0
150,366	0.167	0.93	12.5
173,818	0.167	0.94	12.6
195,422	0.167	0.95	12.7
213,738	0.167	0.96	12.8
262,081	0.168	1.01	13.4
318,870	0.168	1.03	13.6
338,488	0.168	1.05	13.9
345,254	0.168	1.05	13.9
373,197	0.168	1.06	14.0
397,304	0.168	1.06	14.1
420,198	0.168	1.07	14.1
433,115	0.169	1.09	14.4
183,115	0.169	1.12	14.7
533,115	0.169	1.16	15.3
583,115	0.170	1.18	15.6
633,115	0.171	1.25	16.5

Table A6 continued

Number of Cycles, N	Crack Mouth Opening, V_m (in)	Crack Length, a (in)	ΔK (ksi $\sqrt{\text{in}}$)
658,593	0.171	1.26	16.7
708,593	0.171	1.28	17.0
733,905	0.171	1.30	17.3
783,905	0.172	1.33	17.8
833,905	0.173	1.37	18.4
883,905	0.173	1.38	18.6
923,061	0.173	1.42	19.4
952,245	0.175	1.48	20.5
969,749	0.175	1.50	21.1
999,149	0.176	1.55	22.2
1,009,149	0.177	1.58	22.8
1,019,149	0.178	1.60	23.3
1,039,149	0.179	1.65	24.5
TREATMENT			
1,049,149	0.179	1.65	24.5
1,059,149	0.179	1.65	24.5
1,069,149	0.179	1.65	24.5
1,079,149	0.180	1.67	25.0
1,100,000	0.183	1.74	27.5
1,125,000	0.185	1.80	29.6
1,150,000	0.191	1.93	35.5
1,165,000	0.203	2.07	44.4

REFERENCES

- [1] A A Kheraif and M Ramamoorthi, "Fatigue behaviour of recasted removamble partial denture alloys," *International Journal of Dental Clinics*, vol. 3, no. 4, pp. 20-22, 2011.
- [2] R O Ritchie, S Suresh, and C M Moss, "Near-threshold crack growth in 2 ¼ Cr-1 Mo pressure vessel steel in air and hydrogen," *Journal of Engineering Materials*, vol. 102, no. 3, p. 293, 1980.
- [3] S R Biswal, "Fatigue behaviour analysis of differently heat treated medium carbon steel," National Institute of Technology, Rourkela. India, Rourkela, Unpublished Master's Degree Thesis, 2013.
- [4] J Gedeon, "On some spacecraft fatigue-crack propagation problems," *Acta Astronautica*, vol. 12, no. 4, 1985.
- [5] J J Wijker, *Spacecraft Structures*. Berlin, Germany: Springer-Verlag Berlin Heidelberg, 2008.
- [6] L Tamara, "Crash of an Icon," *Miami New Times*, March 22 2007.
- [7] Associated Press, "Boeing admits bad work on ill-fated Japanese Boeing 747," *Star-News*, September 8 1985.
- [8] www.airdisasters.co.uk. (2011, July) Airline Disasters. [Online]. <http://www.airdisasters.co.uk/>
- [9] A Urbach, M Banov, V Turko, and Y Feshchuk, "Diagnostics of fatigue damage of gas turbine engine blades by acoustic emission method," *World Academy of Science*, vol. 59, no. 2011, pp. 906-911, 2011.

- [10] N E Frost, J M Kenneth, and P P Leslie, *Metal Fatigue*. Mineola, NY: Courier Dover Publications, 1999.
- [11] R I Stephens, A Fatemi, R R Stephens, and H O Fuchs, *Metal Fatigue in Engineering*. New York, NY: Wiley-IEEE, 2001.
- [12] D William, *Materials Science and Engineering*, 9th ed. New York, NY: Wiley, 2014.
- [13] N A Fleck and R A Smith, "Fatigue life prediction of a structural steel under service loading," *International Journal of Fatigue*, vol. 6, no. 4, pp. 203-210, 1984.
- [14] M Kay, *Practical Hydraulics*, 2nd ed. New York, NY: Taylor & Francis, 2008.
- [15] National Transportation Safety Board, "Enbridge incorporated hazardous liquid pipeline rupture and release. Pipeline Accident Report, NTSB/PAR-12/01," Washington, D.C., 2012.
- [16] National Transportation Safety Board, "Pipeline Accident Brief, DCA-00-MP-004," Washington, D.C., 2001.
- [17] National Transportation Safety Board, "Pipeline Accident Brief, DCA-00-MP-005," Washington, D.C., 2001.
- [18] National Transportation Safety Board, "Pipeline Accident Brief, DCA05-MP001," Washington, D.C., 2007.
- [19] National Transportation Safety Board, "Pipeline Accident Brief, DCA09FP007," Washington, D.C., 2013.
- [20] National Transportation Safety Board, "Pipeline Accident Brief, DCA99-MP005," Washington, D.C., 2001.
- [21] National Transportation Safety Board, "Rupture of enbridge pipeline and release of crude oil near Cohasset, Minnesota. Pipeline Accident Report, NTSB/PAR-04/01," Washington, D.C., 2002.
- [22] S N Perov and Y N Skvortcov, "Safety estimation of pipelines with fatigue cracks," *Vestnik SamGU*, vol. 8, no. 2, p. 67, 2008.

- [23] L I Domozhirev , "Fatigue life analysis of natural gas pipelines containing fatigue cracks," *Gas Industry*, vol. 7, pp. 70-74, 2005.
- [24] K J Miller, "Initiation and Growth Rates of Short Fatigue Cracks," in *Fundamentals of Deformation and Fracture*. Cambridge, U.K.: Cambridge University Press, 1985, pp. 477-500.
- [25] O K Chopra, "Mechanism and estimation of fatigue crack initiation in austenitic stainless steels in LWR environments," Argonne National Laboratory, NUREG/CR-6787, 2002.
- [26] S G Raman, D Argence, and A Pineau, "High temperature short fatigue crack behaviour in a stainless steel," *Fatigue Fracture and Engineering Materials Structures*, vol. 20, pp. 1015-1031, 1997.
- [27] K J Miller, "Damage in fatigue: a new outlook," in *International Pressure Vessels and Piping Codes and Standards*, 3131st ed. New York, NY: American Society of Mechanical Engineers, 1995, vol. vol. 1: Current Applications, pp. 191-192.
- [28] K Tokaji, T Ogawa, and S Osaka, "The growth of microstructurally small fatigue cracks in a ferrite-pearlite steel," *Fatigue Fracture and Engineering Materials Structures*, vol. 11, no. 5, pp. 311-342, 1988.
- [29] D J Gavenda, P R Luebbbers, and O K Chopra , "Crack initiation and crack growth behavior of carbon and low-alloy steels," *Fatigue and Fracture*, vol. 350, no. 1, pp. 243-255, 1997.
- [30] J Morrow, "Cyclic plastic strain energy and fatigue of metals," in *Damping and Cyclic Plasticity*, *ASTM STP 378*, Conshohocken, PA, 1965, pp. 45-87.
- [31] G Irwin, "Analysis of stresses and strains near the end of a crack traversing a plate," *Journal of Applied Mechanics*, vol. 24, pp. 361-364, 1957.
- [32] J R Rice, "A path independent integral and the approximate analysis of strain concentration by notches and cracks," *Journal of Applied Mechanics*, vol. 35, no. 2, pp. 379-386, 1968.
- [33] A A Griffith, "The phenomena of rupture and flow in solids," *Philosophical Transactions of the Royal Society of London. Series A, containing papers of a mathematical or physical character*, vol. 221, pp. 163-198, 1921.

- [34] C E Inglis, "Stresses in a plate due to the presence of cracks and sharp corners," in *SPIE Milestone Series MS*, vol. 137, London, 1997, pp. 3-17.
- [35] A C Fischer-Cripps, *Introduction to Contact Mechanics*, 2nd ed. New York, NY: Springer, 2007.
- [36] M Seika, "Stresses in a semi-infinite plate containing a U-type notch under uniform tension," *Engineering Architecture*, vol. 27, no. 5, pp. 285-294, 1960.
- [37] O L Bowie, "Analysis of edge notches in a semi-infinite region, AMRA TR 66-07," Army Materials Research Agency, Watertown, MA, Technical Report 1966.
- [38] F I Barrata and D M Neal, "Stress concentration factors in U-shaped and semi-elliptical shaped edge notches," *Journal of Strain Analysis*, vol. 5, no. 2, p. 121, 1970.
- [39] H Neuber, "Theory of stress concentration for shear-strained prismatical bodies with arbitrary nonlinear stress-strain law," *Journal of Applied Mechanics*, vol. 28, no. 4, pp. 544-550, 1961.
- [40] W Ramberg and W R Osgood, "Description of stress-strain curves by three parameters," National Advisory Committee for Aeronautics, Washington, D.C., Technical Note 902, 1943.
- [41] Y Higashida and F V Lawrence, "Strain controlled fatigue behavior of weld metal and heat-affected base metal in A36 and A514 steel welds," College of Engineering, University of Illinois, Urbana, IL, Report of the Fracture Control Program FCP 22, 1976.
- [42] (2014, January) Stress intensity factor. [Online].
http://en.wikipedia.org/wiki/Stress_intensity_factor
- [43] G Irwin, "Fracture dynamics," *Fracturing of Metals*, vol. 40A, pp. 147-166, 1948.
- [44] D M Marsh, "Plastic flow and fracture of glass," *Proceedings of Royal Society of London*, vol. 282, pp. 33-43, 1964.
- [45] Ali Fatemi. Fundamentals of LEFM. [Online].
https://www.efatigue.com/training/Chapter_6.pdf

- [46] W Calister, *Material Science and Engineering: An Introduction*, 3rd ed. New York, NY: John Wiley & Sons, 1994.
- [47] ASTM E399, Standard Test Method for Linear-Elastic Plane-Strain Fracture Toughness K_{Ic} of Metallic Materials, 2009.
- [48] A Wohler, "Versuche uber die festiykeit eisenbahnwagenuchsen," *Bauwesen*, vol. 10, 1860.
- [49] W Schutz, "A history of fatigue," *Engineering Fracture Mechanics*, vol. 54, no. 2, pp. 263-300, 1996.
- [50] W Cui, "A state-of-the-art review on fatigue life prediction methods for metal structures," *Journal of Materials Science Technology*, vol. 7, no. 1, pp. 43-56, 2002.
- [51] N A Fleck, K J Kang, and M F Ashby, "Overview no. 112: the cyclic properties of engineering materials," *Acta Metallic Materials*, vol. 42, no. 2, pp. 365-381, 1994.
- [52] S Suresh, *Fatigue of Materials*, 2nd ed. New York, NY: Cambridge University Press, 1998.
- [53] P J Forsyth, "A two stage process of fatigue crack growth," in *Crack Propagation Symposium*, Cranfield, UK, 1961, pp. 76-94.
- [54] P J Forsyth, *The Physical Basis of Metal Fatigue*. New York, NY: American Elsevier Pub. Co., 1969.
- [55] L P Pook, *Metal Fatigue: What It Is, Why It Matters*, XVII ed. New York, NY: Springer, 2007.
- [56] L P Pook, *Crack Paths*. Southampton, UK: WIT Press, 2002.
- [57] K Tanaka, Y Akinawa , and E Matsui, "Statistical characteristics of propagation of small fatigue specimens of aluminum alloy 2024-T3," *Materials Science and Engineering*, vol. 104, pp. 105-115, 1988.
- [58] J Lankford, "Influence of microstructure on growth of small fatigue cracks," *Fatigue of Engineering Materials and Structures*, vol. 8, no. 2, pp. 161-175, 1985.

- [59] K Tanaka, M Hojo, and Y Nakai, "Fatigue of Engineering Materials and Structures," in *ASTM STP 811*, Conshohocken, PA, 1983, pp. 207-232.
- [60] J Schijve, "Observations on the prediction of fatigue crack growth propagation under variable-amplitude loading. Fatigue crack growth under spectrum loads," in *ASTM STP 595*, Conshohocken, PA, 1976, pp. 3-23.
- [61] K Tokaji, T Ogawa, Y Harada, and Z Ando, *Fatigue of Engineering Materials and Structures*. New York, NY: Wiley, 1986.
- [62] P Paris and F A Erdogan, "A critical analysis of crack propagation laws," *Journal of Basic Engineering*, vol. 85, no. 4, pp. 528-534, 1963.
- [63] N Pugno, M Ciavarella, P Cornetti, and A Carpinteri, "A Generalized Paris' Law for fatigue crack growth," *Journal of the Mechanics and Physics of Solids*, vol. 54, no. 7, pp. 1333-1349, 2006.
- [64] P C Paris, M P Gomez, and W Anderson, "A rational analytic theory of fatigue, the trend in engineering," *University of Washington*, vol. 13, no. 1, pp. 9-14, 1961.
- [65] I P Pook and R A Smith, "Theoretical Background to Elastic Fracture Mechanics," in *Fracture Mechanics. Current Status, Future Prospects*. Oxford: Pergamon Press, 1979, pp. 26-67.
- [66] G Totten, "Fatigue crack propagation," *Advanced Materials and Processes*, vol. 166, no. 5, p. 39, May 2008.
- [67] A H Cottrell, *Theory of Crystal Dislocations*. London, New York, NY: Gordon and Breach, 1964.
- [68] J C Newman, "The merging of fatigue and fracture mechanics concepts: a historical perspective," *Progressive Aerospace Science*, vol. 34, no. 5, pp. 347-390, 1998.
- [69] R G Forman, V E Kearney, and R M Engle, "Numerical analysis of crack propagation in cyclic-loaded structures," *Journal of Basic Engineering*, vol. 89, no. 3, pp. 459-463, 1967.
- [70] K Walker, "The effect of stress ratio during crack propagation and fatigue for 2024-T3 and 7075-T6 Aluminum," in *ASTM STP 462*, Conshohocken, PA, 1970, p. 1.

- [71] F Erdogan and M Ratwani, "Fatigue and fracture of cylindrical shells containing a circumferential crack," *International Journal of Fracture Mechanics*, vol. 6, no. 4, pp. 379-392, 1970.
- [72] NASA, "NASGRO Fatigue Crack Growth Computer Program, Version 2.01," NASA, Houston, TX, Technical Report NASA JSC-22267A, 1994.
- [73] S Saxena, "Assessing the accuracy of fatigue life in surface-cracked straight pipes," *Fatigue & Fracture of Engineering Materials & Structures Volume*, vol. 34, no. 12, pp. 1003-1011, December 2011.
- [74] A J McEvily, "On the Quantitative Analysis of Fatigue Crack Propagation," in *Fatigue Mechanisms: Advances in Quantitative Measurement of Physical Damage*, ASTM STP 811, Conshohocken, PA, 1983, pp. 283-312.
- [75] R Roberts and F Erdogan, "The effect of mean stress on fatigue crack propagation in plates under extension and bending," *Journal of Basic Engineering*, vol. 89, no. 4, pp. 885-892, 1967.
- [76] M Klesnil and P Lukas, "Effect of stress cycle asymmetry on fatigue crack growth," *Material Science and Engineering*, vol. 9, pp. 231-240, 1972.
- [77] S Arad, J C Radon, and L E Culver, "Design against fatigue failure in thermoplastics," *Journal of Mechanical Engineering Science*, vol. 4, no. 3, pp. 511-522, 1972.
- [78] S Mostovoy and E J Ripling, "Flaw tolerance of a number of commercial and experimental adhesives," *Polymer Science Technology B*, vol. 9B, pp. 513-562, 1975.
- [79] R Badaliane, "Application of strain energy density factor to fatigue crack growth analysis," *Engineering Fracture Mechanics*, vol. 13, no. 3, pp. 657-666, 1986.
- [80] J A Bannantine, J J Comer, and J L Handrock, *Fundamentals of Metal Fatigue Analysis*. Englewood Cliffs, NJ: Prentice Hall, 1990.
- [81] E I Stephens, E C Sheets, and G O Njiius, "Fatigue crack growth and life predictions in man-ten steel subjected to single and intermittent tensile overloads, cyclic stress-strain and plastic deformation aspects of fatigue crack growth," in *ASTM STP 637*, Conshohocken, PA, 1977, p. 176.

- [82] M Benachour, A Hadjoui, M Benguediab, and N Benachour, "Stress ratio effect on fatigue behavior of aircraft aluminum Alloy 2024T351," in *Material Research Society Conference Proceedings*, vol. 1276, Cambridge, UK: Cambridge University Press, 2010, p. 1276.
- [83] R I Stephens, P H Benner, G Mauritzson, and G W Tindall, "Constant and Variable Amplitude Fatigue Behavior of Eight Steels," *Journal of Testing and Evaluation*, vol. 7, no. 2, p. 68, 1979.
- [84] J M Barsom and S T Rolfe, *Fracture and Fatigue Control in Structures*, 3rd ed. Conshohocken, PA: ASTM, 1999.
- [85] D L Davidson and S Suresh, *Fatigue Crack Growth Threshold Concepts*. New York, NY: TMS-AIME, 1984.
- [86] D L Davidson and J Lankford, "Plastic strain distribution at the tips of propagating fatigue cracks," *Journal of Engineering Materials and Technology*, vol. 98, no. 1, pp. 24-29, 1976.
- [87] C Loye, C Bathias, D Retali, and J C Devaux, "The plastic zone ahead of a fatigue crack in 316 stainless steel," in *Fatigue Mechanisms: Advances in Quantitative Measurement of Physical Damage, ASTM STP 811.*, Conshohocken, PA, 1983, pp. 427-444.
- [88] A Chikh, A Imad, and M Bengauediab, "Influence of the cyclic plastic zone size on the propagation of the fatigue crack in case of 12NC6 steel," *Computational Materials Science*, vol. 43, no. 4, pp. 1010-1017, October 2008.
- [89] W Elber, "Fatigue crack closure under cyclic tension," *Engineering Fracture Mechanics*, vol. 2, no. 1, pp. 37-45, 1970.
- [90] W Elber, "The significance of fatigue crack closure," in *ASTM STP 486*, Conshohocken, PA, 1971, pp. 230-242.
- [91] J C Newman and W Elber, "Mechanics of fatigue crack closure," in *ASTM STP 982*, Conshohocken, PA, 1988, pp. 24-36.
- [92] J C Newman and R C McClung, "Advances in fatigue crack closure measurement and analysis," in *ASTM STP 1343*, Conshohocken, PA, 1999, pp. 44-52.

- [93] A K Vasudevan, K Sadananda, and N Louat, "A review of crack closure, fatigue crack threshold and related phenomena," *Material Science Engineering*, vol. A1, no. 88, pp. 1-22, 1994.
- [94] A K Vasudevan, K Sadananda, and N Louat, "Two critical stress intensities for threshold fatigue crack propagation," *Scripta Metall et Materialia*, vol. 28, no. 1, pp. 65-70, 1993.
- [95] A K Vasudevan, K Sadananda, and G Glinka, "Critical parameters for fatigue damage," *International Journal of Fatigue*, vol. 23, pp. 39-53, 2001.
- [96] C J Beevers, "The effect of air and vacuum environments on fatigue crack growth rates Ti-6Al-4V," *Metal Transactions*, vol. 5, no. 2, pp. 391-398, 1974.
- [97] R J Cooke, P E Irving, G S Booth, and C J Beevers, "The slow fatigue crack growth and threshold behaviour of a medium carbon alloy steel in air and vacuum," *Engineering Fracture Mechanics*, vol. 7, no. 1, pp. 69-77, 1975.
- [98] U Krupp, *Fatigue crack propagation in metals and alloys*. Weinheim, Germany: WILEY-VCH Verlag GmbH & Co, 2007.
- [99] S Suresh, *Fatigue of Materials*, 2nd ed. Cambridge, UK: Cambridge University Press, 1988.
- [100] S Suresh, G F Zaminski, and R O Ritchie, "Oxide-induced crack closure: an explanation for near-threshold corrosion fatigue crack growth behavior," *Metallurgical Transactions A*, vol. 12, no. 8, pp. 1435-1443, 1981.
- [101] A K Vasudevan and K Sadananda, "Classification of fatigue crack growth behavior," *Metallic Materials Transactions A*, vol. 26, no. 5, pp. 1221-1234, 1995.
- [102] A Carpinteri, M Freitas, and A Spagnoli, *Biaxial/multiaxial Fatigue and Fracture*. New York, NY: Elsevier, 2003.
- [103] E J Imhof and J M Barsom, "Fatigue and corrosion-fatigue crack growth of 4340 steel at various yield strengths," in *Progress in Flaw Growth and Fracture Toughness Testing, ASTM STP 536*, Conshohocken, PA, 1973, p. 182.
- [104] S R Novak, "Corrosion-fatigue crack initiation behavior of four structural steels," in *Corrosion Fatigue: Mechanics, Metallurgy, Electrochemistry, and Engineering, ASTM STP 801*, Conshohocken, PA, 1983, pp. 26-63.

- [105] H G Popp, L G Wilber, and V J Erdeman, "Metal fatigue damage mechanism. Detection, avoidance and repair," in *ASTM STP 495*, Conshohocken, PA, 1971, p. 228.
- [106] G E Linnert, *Welding Metallurgy*, 2nd ed. New York, NY: American Welding Society, 1967.
- [107] C Makabe, A Murdani, K Kuniyoshi, Y Irei, and A Saimoto, "Crack-growth arrest by redirecting crack growth by drilling stop holes and inserting pins into them," *Engineering Failure Analysis*, vol. 16, no. 1, pp. 475-483, 2009.
- [108] P S Song and Y L Shieh, "Stop drilling procedure for fatigue life improvement," *International Journal of Fatigue*, vol. 26, no. 12, pp. 1333-1339, 2004.
- [109] D Broek, *Elementary Engineering Fracture Mechanics*. New York, NY: Springer, 1986.
- [110] H P Leeuwen, "The repair of fatigue cracks in low-alloy steel sheet," National Aerospace Institute of Amsterdam, Amsterdam, Report TR 70029, 1970.
- [111] M A Landy, H Armen, and H L Eidinoff, "Enhanced stop-drill repair procedure for cracked structures," in *ASTM STP 927*, Conshohocken, PA, 1986, pp. 190-220.
- [112] A Y Chen et al., "Study of toughening mechanisms through the observations of crack propagation in nanostructured and layered metallic sheet," *Materials Science and Engineering A*, vol. 528, no. 29-30, pp. 8389-8395, 2011.
- [113] J Z Lu, K Y Luo, and F Z Dai, "Effects of multiple laser shock processing (LSP) impacts on mechanical properties and wear behaviors of AISI 8620 steel," *Materials Science and Engineering A*, vol. 536, pp. 57-63, 2012.
- [114] J Z Lu, K Y Luo, and Y K Zhang, "Grain refinement mechanism of multiple laser shock processing impacts on ANSI 304 stainless steel," *Acta Materialia*, vol. 58, no. 16, pp. 5354-5362, 2010.
- [115] X D Ren, Q B Zhan, and H M Yang, "The effects of residual stress on fatigue behavior and crack propagation from laser shock processing-worked hole," *Materials and Design*, vol. 44, pp. 149-154, 2013.

- [116] I B Roman, A S Banea, and M H Ierean, "A review on mechanical properties of metallic materials after laser shock processing," *Bulletin of the Transylvania University of Brasov, Series I: Engineering Sciences*, vol. 4, no. 2, pp. 81-86, 2011.
- [117] P S Song and G L Sheu, "Retardation of fatigue crack propagation by indentation technique," *International Journal of Pressure Vessels and Piping*, vol. 79, no. 11, pp. 725-733, 2002.
- [118] A Baker, "Growth characterization of fatigue cracks repaired with adhesively bonded boron/epoxy patches," in *Proceedings of International Conference on Fracture, ICF-9*, Sydney, Australia, April 1-5, 1997.
- [119] V Sabelkin, S Mall, and J B Avram, "Fatigue crack growth analysis of stiffened cracked panel repaired with bonded composite patch," *Engineering Fracture Mechanics*, vol. 73, no. 11, pp. 1553-1567, 2006.
- [120] D Seo and J Lee, "Fatigue crack growth behavior of cracked aluminum plate repaired with composite patch," *Composite Structures*, vol. 57, no. 1, pp. 323-330, 2002.
- [121] D M Shuter and W Geary, "The Influence of Specimen Thickness on Fatigue Crack Growth Retardation Following an Overload," *International Journal of Fatigue*, vol. 17, no. 2, pp. 111-119, 1995.
- [122] P S Song and Y L Shieh, "Stop crack growth and closure behavior of surface cracks," *International Journal of Fatigue*, vol. 264, pp. 429-436, 2004.
- [123] E J Von Eow and R W Hertzberg, "In stress analysis and growth of cracks," in *Proceedings of National Symposium of Fracture Mechanics, Part 1, ASTM STP 513*, Conshohocken, PA, 1972, pp. 230-259.
- [124] P K Sharp, J Q Clayton, and G Clark, "Retardation and repair of fatigue cracks by adhesive infiltration," *Fatigue and Fracture of Engineering Materials and Structures*, vol. 20, no. 4, pp. 605-614, 1997.
- [125] P S Song, S Hwang, and C S Shin, "Effect of artificial closure materials on crack growth retardation," *Engineering Fracture Mechanics*, vol. 60, no. 1, pp. 47-58, 1998.

- [126] C S Shin and C Q Cai, "Surface fatigue crack growth suppression in cylindrical rods by artificial infiltration," *International Journal of Fatigue*, vol. 30, no. 3, pp. 560-567, 2008.
- [127] C S Shin and C Q Cai, "A model for evaluating the effect of fatigue crack repair by the infiltration method," *Fatigue Fracture Engineering Material Structures*, vol. 23, no. 10, pp. 835-845, 2000.
- [128] B C Sheu, P S Song, and C S Shin, "The effect of infiltration induced crack closure on crack growth retardation," *Scripta Metallurgica et Materialia*, vol. 31, no. 10, pp. 1301-1306, 1994.
- [129] Y Y Wang, M X Zho, and D Q Feng, "A study of retarding fatigue crack growth using an artificial wedge," *Fatigue and Fracture of Engineering Material Structures*, vol. 16, no. 3, pp. 363-376, 1993.
- [130] M N James and G C Smith, "Surface microcrack closure in fatigue: a comparison of compliance and crack sectioning data," *International Journal of Fracture*, vol. 22, no. 2, pp. R69-R75, 1983.
- [131] R Syed and W Jiang, "Fatigue crack behavior of stainless steel 304 by the addition of carbon nanotubes," *Journal of Nanomaterials*, vol. 2014, pp. 1-6, 2014.
- [132] L Boger, J Sumfleth, H Hedemann, and K Schulte, "Improvement of fatigue life by incorporation of nanoparticles in glass fiber reinforced epoxy," *Applied Science and Manufacturing*, vol. 41, no. 10, pp. 1419-1424, 2010.
- [133] C S Grimmer and C K Dharan, "High-cycle fatigue of hybrid carbon nanotube/glass fiber/polymer Composites," *Journal of Materials Science*, vol. 43, no. 13, pp. 4487-4492, 2008.
- [134] Y M Jen and Y H Yang, "A study of two-stage cumulative fatigue behavior for CNT/epoxy composites," *Procedia Engineering*, vol. 2, no. 1, pp. 2111-2120, 2010.
- [135] S Lower, *Electrochemistry*. Vancouver, Canada: Simon Fraser University, 2007.
- [136] A Galvani, "Viribus electricitatis in motu musculari," *De Bononiensi Scientiarum et Artium Instituto atque Academia Commentarii*, vol. 7, pp. 99-156, 1791.

- [137] M Ciobanu, J P Wilburn, M L Krim, and D E Cliffler, "Fundamentals," in *Handbook of Electrochemistry*. Amsterdam, The Netherlands: Elsevier B.V., 2007, pp. 12-18.
- [138] D E Roller and R Blum, *Physics: Electricity Magnetism and Light*, 2nd ed. Oakland, CA: Holden Day, 1982.
- [139] W Gibbs, "On the Equilibrium of Heterogeneous Substances," *Transactions of the Connecticut Academy of Arts and Sciences*, vol. 3, pp. 108-524, 1878.
- [140] J W Hittorf, *Ueber die Wanderungen der Ionen während der Elektrolyse*. Weinheim, Germany: WILEY-VCH Verlag GmbH & Co, 1853.
- [141] W F Kohlrausch and O Grotrian, "On the electrical conducting power of the chlorides of the alkalis, alkaline earths, and nitric acid in aqueous solutions," *Philosophical Magazine*, vol. XLIX, pp. 417-425, 1875.
- [142] S Arrhenius, *Recherches sur la conductivité galvanique des électrolytes*, 1884, Unpublished Doctoral Dissertation.
- [143] P Debye and E Huckel, "The theory of electrolytes. Lowering of freezing point and related phenomena," *Physikalische Zeitschrift*, vol. 24, pp. 185-206, 1923.
- [144] Naval Air System Comman, Engineering Division, Federal specification QQ-N-290A: nickel plating (electrodeposited), November 12, 2001.
- [145] R Bottger, "Investigation of nickel plating on metals," *Erdmann's J. Praktische Chemie*, vol. 30, p. 267, 1843.
- [146] G Dubpernell, "The story of nickel plating," *Plating*, vol. 46, p. 599, 1959.
- [147] J K Dennis and T E Such, *Nickel and Chromium Plating*, 3rd ed. Cambridge, UK: Woodhead Publishing, 1993.
- [148] W H Remington, "Improved process of electroplating with nickel," Grant US82877 A, October 6, 1868.
- [149] E Weston, "Improvement in Nickel-plating," Grant US211071 A, December 17, 1878.

- [150] O P Watts, "Progress of the hot nickel solution," *Transactions of The Electrochemical Society*, vol. 59, no. 1, pp. 379-384, 1931.
- [151] E Weil, "Material science of electrodeposits," *Plating & Surface Finishing*, vol. 69, no. 12, pp. 46-51, 1982.
- [152] E P Degarmo, J Black, and K A Ronald, *Materials and Processes in Manufacturing*, 9th ed. New York, NY: Wiley, 2003.
- [153] P V Jadhav and D S Mankar, "Effect of surface roughness on fatigue life of machined component of Inconel 718," in *Bharati Vidyapeeth Deemed University International Conference*, Maharashtra, India, 2011, pp. 312-320.
- [154] G Deng, K Nagamoto, Y Nakano, and T Nakanishi, "Evaluation of the effect of surface roughness on crack initiation life," in *International Conference on Fracture*, Ottawa, Canada, 2009, pp. 121-135.
- [155] N A Alang, N A Razak, and A K Miskam, "Effect of surface roughness on fatigue life of notched carbon steel," *International Journal of Engineering & Technology IJET-IJENS*, vol. 11, no. 1, pp. 160-163, 2001.
- [156] H Itoga, K Tokaji, M Nakajima, and H Ko, "Effect of surface roughness on step-wise S-N characteristics in high strength steel," *International Journal of Fatigue*, vol. 25, no. 5, pp. 379-385, 2003.
- [157] P G Fluck, "The influence of surface roughness on the fatigue life and scatter of test results of two steels," in *Proceedings of ASTM STP 359*, Conshohocken, 1951, pp. 584-592.
- [158] J A Di Bari, *Electrodeposition of nickel in Modern Electroplating*. New York, NY: John Wiley and Sons Inc., 2000.
- [159] Y D Gamburg and G Zangari, *Theory and practice of metal electrodeposition*. New York, NY: Springer Science+Business Media, 2011.
- [160] G H Koch, M P Brongers, N G Thompson, Y P Virmani, and J H Payer, "Corrosion costs and preventive strategies in the United States," Federal Highway Administration, 2001.
- [161] I V Semenova, G M Dlorianovich, and A V Horoshilov, *Corrosion and corrosion protection*. Moscow, Russia: FIZMATLIT, 2002.

- [162] R Heidersbach, *Metallurgy and corrosion control in oil and gas production*. New York, NY: John Wiley & Sons, 2011.
- [163] R Fessler, "Pipeline corrosion," US Department of Transportation, Pipeline and Hazardous Materials Safety Administration, Office of Pipeline Study, Technical Report DTRS56-02-D-70036, 2008.
- [164] H E Cardenas, "Galvanic corrosion of steel," University of Illinois, Champaign, IL, Research Report 1997.
- [165] P A Schweitzer, *Encyclopedia of Corrosion Technology*, 2nd ed. New York, NY: Marcel Dekker, Inc., 2004.
- [166] E McCafferty, *Introduction to Corrosion Science*. New York, NY: Springer, 2010.
- [167] V S Sastri, *Green Corrosion Inhibitors*. Hoboken, NJ: John Wiley & Sons, Inc., 2011.
- [168] H L Craig and T W Crooker, "Corrosion-fatigue technology," in *Proceedings of ASTM STP 642*, Conshohocken, PA, pp. 189-201, 1978.
- [169] O F Devereux and A J McEvily, *Corrosion fatigue: chemistry, mechanics, and microstructure*. Houston, TX: National Association of Corrosion Engineers, 1972.
- [170] F R Stonesifer and J M Krafft, "Fatigue crack growth in A36/A283 plate in air and sea water environments," Naval Research Laboratory, Washington, D.C., Memorandum Report 4467, 1981.
- [171] (2014, January) www.onlinemetals.com. Chemical and Physical Properties of ASTM A36 Steel [Online]. <http://www.onlinemetals.com/alloycat.cfm?alloy=A36>
- [172] J M Barsom and S T Rolfe, *Fracture and Fatigue Control in Structures: Application of Fracture Mechanics*, 2nd ed. Englewood Cliffs, NJ: Prentice Hall, 1987.
- [173] MTS Systems Corporation, "Clip-On Gages ," MTS International, Eden Prairie, MN, Equipment Manual 100-007-834 B, 2008.
- [174] W F Dean and C E Richard, "A simple and sensitive method of monitoring crack and load in compact fracture mechanics specimens using strain gages," *Journal of Testing and Evaluation*, vol. 7, no. 3, pp. 147-154, 1979.

- [175] J C Newman, Y Yamada, and M A James, "Back-face strain compliance relation for compact specimens for wide range in crack lengths," *Engineering Fracture Mechanics*, vol. 78, no. 15, pp. 2707-2711, 2011.
- [176] Buehler LTD, "BUEHLER® Alpha, Beta & Vector™ grinder-polishers and power heads," Buehler LTD, Lake Bluff, IL, Promotional Brochure 2005.
- [177] J M Barsom, "Fatigue-crack propagation in steels of various yield strengths," *Journal of Manufacturing Science and Engineering*, vol. 93, no. 4, pp. 1190-1196, 1971.
- [178] P C McKeighan and J H Feiger, "Fatigue crack growth rate behavior of tank car steel TC-128B," Southwest Research Institute, San Antonio, TX, Technical Report 2012.
- [179] C Hinnant, "Fatigue design of process equipment," Paulin Research Group, Houston, TX, Technical Report 2009.
- [180] J W Fisher, B T Yen, and D Wang, "Fatigue of bridge structures. A commentary for design, evaluation and investigation of cracking," Lehigh University, Bethlehem, PA, Technical Report ATLSS Report No. 89-02, 1989.
- [181] J M Barsom, "Structural problems in search of fracture mechanics solutions," in *Fracture Mechanics: Twenty-Third Symposium, ASTM STP 1189*, Conshohocken, PA, 1993, pp. 5-34.
- [182] S T Rolfe, "Fracture and fatigue control in steel structures," *Engineering Journal of American Institute of Steel Construction*, vol. Q1, pp. 1-15, 1977.
- [183] C S Shin and S H Hsu, "Fatigue life extension by an artificially induced retardation mechanism," *Engineering Fracture Mechanics*, vol. 43, no. 4, p. 677, 1992.
- [184] A J Wheeler and A R Ganji, *Introduction to Engineering Experimentation*. Upper Saddle River, NJ: Prentice-Hall, 1996.
- [185] N E Dowling and W K Wilson, "Results of elastic analysis of bluntly notched compact specimens," *Engineering Fracture Mechanics*, vol. 20, no. 3, pp. 569-572, 1984.

- [186] A H Mourad, "Fracture toughness prediction of low alloy steel as a function of specimen notch root radius and size constraints," *Engineering Fracture Mechanics*, vol. 103, pp. 79-93, 2013.
- [187] K Yamagiwa and D W Hoepfner, "In-situ fatigue test of A36-steel," in *Proceedings of 12th International Conference on Fracture*, Ottawa, Canada, 2009, pp. 215-223.
- [188] N Hashimoto, H Tanigawa, M Ando, and M A Sokolov, "TEM observation around crack in fatigue-precracked 1TCT fracture toughness specimen of F82H-IEA," Japan Atomic Energy Research Institute and the Office of Fusion Energy Sciences, Tokyo, Japan, Final Report 2003.
- [189] M Andersson, C Persson, and S Melin, "An in situ SEM study of crack propagation," in *15th European Conference on Fracture*, Alexandroupolis, Greece, 2005, pp. 3-12.
- [190] L Jacobsson and D S Mankar, "SEM study of overload effects during fatigue crack growth using an image analyzing technique and potential drop measures," *Fatigue and Fracture of Engineering Materials and Structures*, vol. 33, no. 2, pp. 105-115, 2010.
- [191] J Palmari, G Rasigni, M Rasigni, J P Palmari, and A Hugot-le Goff, "Study of surface roughness of nickel electrodeposits," *Journal of the Optical Society of America A*, vol. 3, no. 4, pp. 410-416, 1986.
- [192] W Riedel, *Electroless Nickel Plating*. Stevenage, UK: Finishing Publications Ltd, 1991.
- [193] G Di Bari, "Nickel plating. Surface engineering," *ASM Handbook*, vol. 5, pp. 201-212, 1994.
- [194] F C Walsh, C Ponce de Leon, C Kerr, S Court, and B D Barker, "Electrochemical characterization of the porosity and corrosion resistance of electrochemically deposited metal coatings," *Surface and Coatings Technology*, vol. 202, no. 32, pp. 5092-5102, 2008.
- [195] J P Celis, J R Roos, and C Fan, "Porosity of electrolytic nickel-phosphorus coatings," *Transactions of the Institute of Metal Finishing*, vol. 69, no. 1, pp. 15-19, 1991.

- [196] O Sadiku-Agboola, E R Sadiku, O I Ojo, O Akanji, and O F Biotidara, "Influence of operation parameters on metal deposition in bright nickel-plating process," *Portugaliae Electrochimica Acta*, vol. 29, no. 2, pp. 91-100, 2011.
- [197] F A Lowenheim, *Modern Electroplating*. New York, NY: Wiley, 1974.
- [198] E Zahavi and V Torbilo, *Fatigue Design: Life Expectancy of Machine Parts*. Boca Raton, FL: CRC Press, 1996.
- [199] S Gungor and L Edwards, "Effect of surface texture on the initiation and propagation of small fatigue cracks in a forged 6082 aluminum alloy," *Material Science Engineering A*, vol. 160, no. 1, pp. 17-24, 1993.
- [200] J D Fordham, R Pilkington, and C C Rang, "The effect of different profiling techniques on the fatigue performance of metallic membranes of AISI 301 and Inconel 718," *International Journal of Fatigue*, vol. 19, no. 6, pp. 487-501, 1997.
- [201] R C Barrett, "Nickel plating from the sulfamate bath," in *Annual Convention of the American Electroplaters' Society*, Shelton, CT, 1954, pp. 14-18.
- [202] R J Davis, "Nickel, cobalt, and their alloys," *ASM Specialty Handbook*, pp. 111-113, December 2000.
- [203] A H Wahab, M Y Noordin, S Izman, and D Kurniawan, "Quantitative analysis of electroplated nickel coating on hard metal," *The Scientific World Journal*, vol. 2013, pp. 6-12, 2013.
- [204] R Parkinson, *Properties and Applications of Electroless nickel*. Toronto, Canada: Nickel Development Institute, 1997.
- [205] N A Flect and R A Smith, "Crack Closure – is it just a surface phenomenon?," *International Journal of Fatigue*, vol. 4, no. 3, pp. 157-160, 1982.
- [206] V Parkville, *IMMA Handbook of Engineering Materials*, 5th ed. Parkville, Australia: Institute of Metals and Materials Australasia, 1997.
- [207] J R Rice and M A Johnson, "The role of large crack tip geometry changes in plane strain fracture," in *Inelastic Behavior of Solids*. New York, NY: McGraw-Hill, 1970, pp. 641-672.

- [208] F A McClintock, "Plasticity aspects of fracture," in *An Advanced Treatise*. New York, NY: Academic Press, 1971, ch. 3, pp. 47-225.
- [209] R S Vecchio, J S Crompton, and R W Hertzberg, "Anomalous aspects of crack closure," *International Journal of Fracture*, vol. 31, no. 2, pp. R29-R33, 1986.
- [210] R W Hertzberg, C H Newton, and R Jaccard, "Crack Closure: correlation and confusion," in *Mechanics of Fatigue Crack Closure, ASTM STP 982*, Conshohocken, PA, 1988, pp. 139-148.
- [211] F Sun et al., "Corrosion mechanism of corrosion-resistant steel developed for bottom plate of cargo oil tanks," *Acta Metall*, vol. 26, no. 3, pp. 257-264, 2013.
- [212] M H Hussin and M J Kassim, "Electrochemical studies of mild steel corrosion inhibition in aqueous solution by uncaria gambir extract," *Journal of Physical Science*, vol. 21, no. 1, pp. 1-13, 2010.
- [213] A Kumar and A Odeh, "Mechanical properties and corrosion behavior of stainless steels for locks, dams, and hydroelectric plant applications," Department of the Army, US Army Corps of Engineers, Champaign, IL, Technical report REMR-EM-6, 1989.
- [214] W J Schwerdtfeger, "Corrosion rates of binary alloys of nickel and iron measured by polarization methods," *Journal of Research of the National Bureau of Standards*, vol. 70C, no. 3, pp. 1-8, 1966.
- [215] H D Ney, "Corrosion behaviour of nickel and monel in aqueous fluoride media," University of British Columbia, Unpublished Master's Thesis 1964.
- [216] X Shi, L Fay, Z Yang, T A Nguen, and Y Liu, "Corrosion of deicers to metals in transportation infrastructure: introduction and recent developments," *Corrosion Reviews*, vol. 27, no. 1-2, pp. 23-52, 2009.
- [217] Y Xi and Z Xie, "Corrosion effects of magnesium chloride and sodium chloride on automobile components," Colorado Department of Transportation, Technical report CDOT-DTD-R-2002-4, 2002.
- [218] F M Reinhart and J F Jenkins, "Corrosion of materials in surface seawater after 12 and 18 months of exposure," Naval Civil Engineering Laboratory, Port Hueneme, CA, Technical Note N-1213, 1972.

- [219] B R Rebak and P Crook, "Nickel alloys for corrosive environments," *Advanced Materials and Processes*, vol. H2116, no. 2, pp. 1-6, 2000.
- [220] X G Zhang, "Galvanic corrosion," in *Uhlig's Corrosion Handbook*, R W Revie, Ed. New York, NY: John Wiley & Sons Inc., 2011, pp. 123-143.
- [221] Y S Huang and X T Zeng, "Corrosion resistance properties of electroless nickel composite coatings," *Electrochimica Acta*, vol. 49, no. 25, pp. 4313-4319, 2004.
- [222] G A Di Bari, *Electrodeposition of Nickel. Modern Electroplating*, 5th ed., Schlesinger M and Paunovic M, Ed. New York, NY: John Wiley & Sons, 2010.
- [223] U R Evans, *The Corrosion and Oxidation of Metals*, 2nd ed. London, UK: Arnold, 1976.
- [224] T Ernest , R Sorensen, and T Guilinger, "Effectiveness of nickel plating in inhibiting atmospheric corrosion of copper alloy contacts," Sandia National Laboratories, Albuquerque, NM, Report SAND-97-3061C, 1997.
- [225] R N Duncan, "Corrosion resistance of high phosphorus electroless nickel coatings," in *Proceedings of AESF Third Electroless Plating Symposium*, Nashville, TN, 1986.
- [226] W H Metzger, "Characteristics of deposits," in *Symposium on Electroless Nickel Plating, ASTM STP 265*, Conshohocken, PA, 1959.
- [227] M Mohammadi and M Ghorbani, "Wear and corrosion properties of electroless nickel composite coatings with PTFE and/or MoS particles," *Journal of Coatings Technology & Research*, vol. 8, no. 4, p. 527, 2011.